

Department of Physics and Astronomy
University of Heidelberg

Master thesis
in Physics
submitted by

Christopher M. Rank

born in Stuttgart, Germany

March 2013

MRI-based treatment plan simulation and adaptation for ion radiotherapy using a classification-based approach

This Master thesis has been carried out by Christopher M. Rank

at the
German Cancer Research Center (DKFZ)

under the supervision of
Prof. Dr. Peter Bachert
and
Prof. Dr. Oliver Jäkel.

Abstract

MRI-based treatment plan simulation and adaptation for ion radiotherapy using a classification-based approach

Accurate treatment planning and simulation are required to benefit from the highly conformal irradiation of tumors in ion radiotherapy. The purpose of this study was to investigate the potential of MRI for treatment plan simulation and adaptation in ion radiotherapy using a classification-based approach.

At first, a tissue classification tool was developed and applied for deriving so-called pseudo CT numbers from MR images. Suitable MR sequences and parameters were evaluated in cross-validation studies of tissue samples and of patients with tumors in the head region. Then, ion radiotherapy treatment plans were optimized by using both MRI-based pseudo CT and reference CT and dose distributions were calculated on the reference CT. Finally, a target volume shift was simulated and employing a hybrid approach, a treatment plan adapted to the shift was optimized on the basis of a so-called corrected CT. The latter consisted of a reference CT, in which a volume around the target was replaced by pseudo CT values.

The derivation of pseudo CT values led to mean absolute errors in the range of 21 - 95 HU for tissue samples and 141 - 165 HU for patients. Most significant deviations appeared at transitions between different tissue types and at air cavities as well as compact bones. The former originated from partial volume effects and registration errors whereas the latter resulted from the low signal to noise ratio of bones in MR imaging. Simulations of ion radiotherapy treatment plans using pseudo CT revealed only small underdosages of a target volume compared to reference CT simulations. Deviations of the mean dose of target ranged from 0.8 - 3.1 % for tissue samples and 0.4 - 2.0 % for patients. Plans adapted to the target volume shift and optimized on the basis of a corrected CT exhibited an improved target dose coverage compared to non-adapted plans optimized on the basis of a reference CT. The obtained results for tissue samples and the head region of patients provided first evidence that MRI-based derivation of pseudo CT and treatment plan simulation for ion radiotherapy are feasible.

Kurzfassung

MRT-basierte Simulation und Adaption von Bestrahlungsplänen für die Ionentherapie unter Verwendung eines klassifikationsbasierten Ansatzes

Um den Vorteil der in hohem Maße konformen Bestrahlung von Tumoren in der Ionentherapie nutzen zu können, sind eine exakte Bestrahlungsplanung und -simulation erforderlich. Die vorliegende Studie diente zur Untersuchung des Potentials der MRT zur Simulation und Adaption von Bestrahlungsplänen unter Verwendung eines klassifikationsbasierten Ansatzes. Zunächst wurde ein Programm zur Gewebeklassifizierung entwickelt und damit sog. Pseudo-CT-Zahlen aus MR-Bildern abgeleitet. In Kreuzvalidierungsverfahren wurden geeignete MR-Sequenzen und -parameter für Gewebeproben und Patienten mit Tumoren im Kopfbereich untersucht. Anschließend wurden Ionentherapiebestrahlungspläne optimiert, wobei sowohl MRT-basierte Pseudo-CTs als auch Referenz-CTs verwendet wurden, und die Dosisverteilungen auf Referenz-CTs berechnet. Schließlich wurde eine Verschiebung des Zielvolumens simuliert und mit einem hybriden Ansatz ein an die Verschiebung angepasster Bestrahlungsplan auf Basis eines sog. korrigierten CTs optimiert. Bei Letzterem wurde ein um das Zielvolumen liegender Bereich des Referenz-CTs durch Pseudo-CT-Werte ersetzt. Die Ableitung von Pseudo-CT-Werten ergab bei den Gewebeproben mittlere absolute Fehler im Bereich von 21 - 95 HU sowie 141 - 165 HU bei Patienten. An Grenzbereichen zwischen verschiedenen Gewebetypen sowie in luftgefüllten Nebenhöhlen und kompakten Knochen waren die größten Abweichungen zu finden. Erstere konnten auf Teilvolumeneffekte und Registrierungsfehler zurückgeführt werden, während Letztere aus dem niedrigen Signal-Rausch-Verhältnis von Knochen in der MR-Bildgebung resultierten. Die Simulation von Ionentherapiebestrahlungsplänen auf der Basis von Pseudo-CTs zeigte nur kleine Unterdosierungen des Zielvolumens im Vergleich zu Referenz-CT Simulationen. Abweichungen der mittleren Dosis des Zielvolumens lagen zwischen 0.8 - 3.1 % bei Gewebeproben und 0.4 - 2.0 % bei Patienten. Die an die Verschiebung des Zielvolumens angepassten und auf der Basis des korrigierten CTs optimierten Pläne wiesen eine bessere Dosisabdeckung des Zielvolumens auf als nicht angepasste, auf Basis eines Referenz-CTs optimierte Pläne. Die hier erzielten Ergebnisse für Gewebeproben und den Kopfbereich bei Patienten lieferten einen ersten Nachweis, dass die MRT-basierte Ableitung von Pseudo-CTs und Simulation von Bestrahlungsplänen für die Ionentherapie möglich sind.

Contents

1	Introduction	1
2	Fundamentals	3
2.1	Computed tomography	3
2.1.1	Photon interactions with matter	3
2.1.2	Tomographic imaging	4
2.1.3	CT numbers and Hounsfield scale	4
2.2	Magnetic resonance imaging	5
2.2.1	Nuclear magnetic resonance	5
2.2.2	Magnetic resonance tomography	7
2.3	Discriminant analysis	9
2.3.1	Gaussian mixture model framework	9
2.3.2	Process of classification	10
2.4	Ion radiotherapy	12
2.4.1	Physical and radiobiological aspects of ions	12
2.4.2	Treatment planning	14
3	Materials and methods	19
3.1	Tissue samples	19
3.2	Patients	19
3.3	CT equipment and protocols	20
3.4	MR equipment and sequences	20
3.5	Image registration	21
3.6	MMclassification package	22
3.6.1	Statistical computing language <i>R</i>	22
3.6.2	Package overview	22
3.6.3	Workflow for derivation of pseudo CT	23
3.6.4	Image processing	24
3.6.5	HDDA algorithm	26
3.7	Software for treatment plan simulation and adaptation	27
3.7.1	VIRTUOS	27

3.7.2	TRiP98	27
4	Experiments and results	29
4.1	CT image acquisition	29
4.1.1	Tissue samples	29
4.1.2	Patients	29
4.2	MR image acquisition	31
4.2.1	Tissue samples	31
4.2.2	Patients	31
4.2.3	Distribution of absolute MR signal intensities	33
4.3	Derivation of pseudo CT	33
4.3.1	Tissue samples	35
4.3.2	Patients	39
4.4	Ion radiotherapy treatment plan simulation	41
4.4.1	Translation of CT to WEPL	41
4.4.2	Estimation of mean deviation of WET	44
4.4.3	Results of ion treatment plan simulation	44
4.5	Photon radiotherapy treatment plan simulation	51
4.6	Ion radiotherapy treatment plan adaptation	51
5	Discussion	57
5.1	MR image acquisition	57
5.2	Derivation of pseudo CT	58
5.2.1	Tissue samples	58
5.2.2	Patients	59
5.3	Ion radiotherapy treatment plan simulation	61
5.4	Photon radiotherapy treatment plan simulation	62
5.5	Ion radiotherapy treatment plan adaptation	62
5.6	Practical aspects	63
5.7	Outlook	64
6	Conclusions	67
A	Appendix	i
A.1	MMclassification package	i
	Bibliography	xi

List of Acronyms

c CT	corrected CT
CSAME	contribution to the sum of absolute mean errors
CT	computed tomography
DICOM	Digital Imaging and COmmunication in Medicine
DKFZ	German Cancer Research Center (Deutsches Krebsforschungszentrum)
DVH	dose-volume histogram
FOV	field of view
GSI	GSI Helmholtzzentrum für Schwerionenforschung
HDDA	high dimensional discriminant analysis
HIT	Heidelberg Ion-Beam Therapy Center
HLUT	Hounsfield look-up table
HU	Hounsfield unit
linac	linear accelerator
MAE	mean absolute error
ME	mean error
<i>MMclassification</i>	multimodal classification
MPRAGE	magnetization prepared rapid acquired gradient echo
MR	magnetic resonance
MRI	magnetic resonance imaging
NMR	nuclear magnetic resonance

pCT	pseudo CT
PD	proton density
PET	positron emission tomography
PTV	planning target volume
QDA	quadratic discriminant analysis
rCT	reference CT
RF	radio frequency
SNR	signal-to-noise ratio
TRiP98	TReatment plannIng for Particles 98
TSE	turbo spin echo
UTE	ultrashort echo time
VIRTUOS	VIRTUal RadiOtherapy Simulator
WEPL	water equivalent path length
WET	water equivalent thickness

1 | Introduction

Radiotherapy is one of the most important techniques for treating localized tumors. Employing ions as radiation modality offers the opportunity of a highly conformal irradiation. This allows for applying high doses to the tumor volume while sparing the surrounding tissue and organs at risk (Schardt et al., 2010) (fig. 1.1).

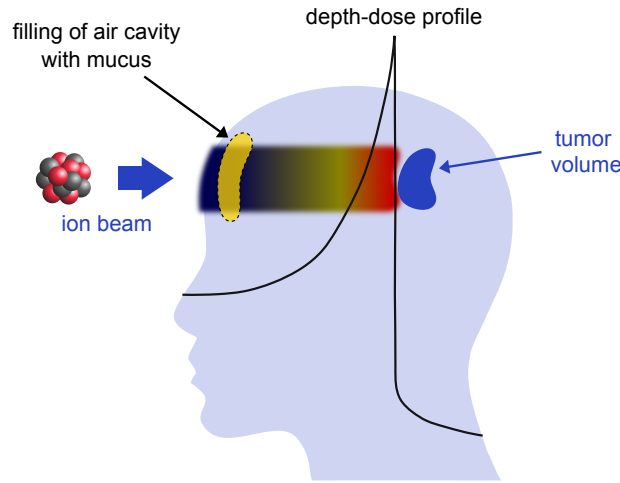


Figure 1.1: Ion radiotherapy offers the opportunity of a highly conformal irradiation of tumors due to the inverse depth-dose profile of charged particles. As a consequence of this high conformality, interfractional changes between the day of CT examination for treatment planning and the days of treatment fractions, e.g. a filling of an air cavity with mucus, may have a large impact on dose distributions within the patient. The result is an impaired dose coverage of the tumor volume and an increased dose to healthy tissue and organs at risk.

Major uncertainties during radiotherapy treatment are caused by anatomical changes, e.g. organ and tumor movement, tumor shrinkage or growth, filling of air cavities as well as gain or loss of weight. Before the treatment of a patient starts, a simulation is carried out in order to evaluate and optimize the dose distribution within the patient. Today, the gold standard for this procedure is based on X-ray computed tomography (CT). However, changes may occur between the day of CT examination for treatment planning and the fractions of treatment. To take these interfractional variations into account, imaging of the patient's anatomy before each fraction and an adaptation of treatment plans to changes are required. For adapting plans even to intrafractional changes, e.g. the movement of chest

during irradiation due to breathing, real-time image guidance would be necessary. However, the application of multiple CT examinations might not be reasonable in many cases due to the additional dose to the patient.

Already today, magnetic resonance imaging (MRI) is increasingly used as an alternative for target delineation in treatment planning due to its superior soft tissue contrast in comparison to CT. However, its application for treatment plan simulation is much more challenging as no physical correlation between magnetic resonance (MR) signal intensities and X-ray attenuation as well as ion ranges in tissue exists. The most advanced project in this context is the current investigation of a hybrid MRI-linac device for photon radiotherapy (Lagendijk et al., 2008; Fallone et al., 2009).

Two different approaches for deriving a so-called pseudo CT (pCT) from MR images are suggested in literature for the simulation of conventional photon treatment plans: *atlas-based methods* employ non-rigid registration to warp a template CT image to the patient's anatomy, whereas *classification-based methods* group tissue voxels into several classes associated with certain bulk CT numbers.

In ion radiotherapy, changes of anatomy have, in comparison to photons, a considerably larger impact on dose distributions within the patient due to the high conformality of ion beams. For that reason, the aim of this work is to investigate the potential of MRI for treatment plan simulation in ion radiotherapy in contrast to investigations in literature for conventional photon radiotherapy (Lee et al., 2003; Prabhakar et al., 2007; Boettger et al., 2008; Karlsson et al., 2008; Kristensen et al., 2008; Stanescu et al., 2008; Wang et al., 2008; Jonsson et al., 2010; Greer et al., 2011; Johansson et al., 2011; Lambert et al., 2011; Dowling et al., 2012; Edmund et al., 2012; Johansson et al., 2012). A two-step approach for the conversion of MR signal intensities to ion ranges is proposed here. A pCT is derived from MR images using a classifier that is based on discriminant analysis, followed by a translation into ion ranges. This *classification-based method* is chosen as it allows a patient-specific voxelwise prediction of pCT numbers.

The following issues for investigating the basic feasibility are covered by this work:

- *Search for suitable MR sequences*: suitable MR sequences are investigated that can be applied for treatment plan simulation and allow a distinction of bones and air.
- *Derivation of pseudo CT*: a classification tool for deriving pCT numbers from MR images is developed and evaluated in studies of tissue samples and of patients with tumors in the head region.
- *Treatment plan simulation*: ion and photon treatment plans are simulated using MRI-based pCTs and results are compared to reference CT (rCT) simulations.
- *Treatment plan adaptation*: the application of MRI for treatment plan adaptation is evaluated by simulating a target volume shift and adapting plans to the shift using a hybrid approach, which combines rCT and pCT information.

2 | Fundamentals

This chapter gives an overview of fundamentals important in this work. In sections 2.1 and 2.2, basics of CT and MRI are presented. Discriminant analysis as a method for classification is explained in section 2.3. Section 2.4 provides an introduction to ion radiotherapy and treatment planning.

2.1 Computed tomography

X-ray CT is a three-dimensional imaging technique that is in common use in radiological diagnostics and allows examining structures inside the body with high resolution in the range of 0.5 mm. It is based on the measurement of X-ray attenuation properties of tissue and features a high geometrical accuracy as well as fast image acquisition times less than 1 s, largely dependent on the application and size of the examined volume. A first technical implementation was accomplished by Hounsfield (1973). Detailed illustrations of CT can be found in Kalender (2011) and Bushberg et al. (2002).

2.1.1 Photon interactions with matter

Interactions of photons traversing matter can be described by contributions of three major interaction processes at X-ray energies used in diagnosis: incoherent Compton scattering, the photoelectric effect and coherent Rayleigh scattering. These interactions result in an attenuation of photons and are mainly influenced by the material composition and the photon energy spectrum. The attenuation is characterized by the linear attenuation coefficient:

$$\mu = \rho_e \sigma, \quad (2.1)$$

with the electron density ρ_e and the total cross-section of interaction processes σ .

The intensity of X-rays after traversing an object can be described by the Beer-Lambert law, that has the following form assuming an inhomogeneous object and a polychromatic X-ray spectrum:

$$I = \int_0^{E_{\max}} I_0(E) e^{-\int_0^d \mu(E) ds} dE, \quad (2.2)$$

with $I_0(E)$ as the initial photon spectrum and d as the thickness of the traversed object.

2.1.2 Tomographic imaging

In CT the imaging volume is divided into a stack of several two-dimensional slices each being composed of small voxels. Measuring X-ray attenuation line integrals I (eq. 2.2) of a large number of projections from different directions through the object, it becomes possible to reconstruct the spatial distribution of linear attenuation coefficients μ for all these voxels (fig. 2.1). For reconstruction, projections covering at least an angular range of 180° are necessary. Modern CT scanners typically measure in fan-beam geometry and cover the full range of 360° . An X-ray tube and a detector facing the tube are mounted on a gantry that rotates continuously around the patient. Meanwhile the patient couch moves in axial direction through the bore of the gantry for acquiring data from several slices, which is called spiral scanning mode.

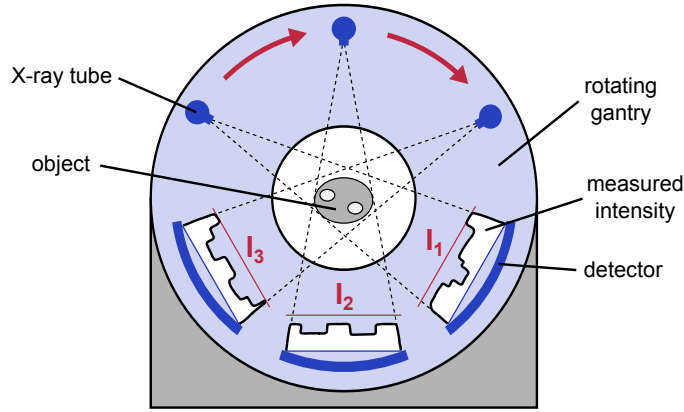


Figure 2.1: Principle of CT imaging: an X-ray tube and a detector facing the tube are mounted on a rotating gantry. X-ray intensities I of a large number of projections from different directions through the object are measured. In addition to the tube rotation, the patient table is moved in axial direction during measurements (into the plane of the drawing). Thus a three-dimensional reconstruction of the spatial distribution of attenuation coefficients of voxels becomes possible.

2.1.3 CT numbers and Hounsfield scale

In order to allow a comparison of CT images acquired on scanners using different energy spectra due to various tube voltages and filtration, the measured linear attenuation coefficient μ is normalized relative to water. It is displayed as CT number, specified in Hounsfield units (HUs):

$$CT\ number = \frac{\mu - \mu_{\text{water}}}{\mu_{\text{water}}} \times 1000\ \text{HU} \quad (2.3)$$

The information measured for each voxel is usually stored with a 12 bit encoding resulting in a CT scale ranging from -1024 to 3071 HU. The value of water is 0 HU by definition and air corresponds to -1000 HU. Considering dense materials, e. g. compact bone, an influence of X-ray spectra on CT numbers can still be observed.

2.2 Magnetic resonance imaging

MRI is a tomographic imaging technique, which has a large spectrum of applications in modern medicine ranging from orthopedics to cancer diagnostics and treatment planning. Using this technique, it is possible to acquire images of inner body structures with a resolution in the range of 1 mm non-invasively and to gain information about physiological processes. Advantages of MRI are an excellent soft tissue contrast and the fact that in contrast to other imaging techniques such as CT or positron emission tomography (PET), no exposure of the patient to ionizing radiation is necessary. Comprehensive descriptions of fundamentals and applications of MRI are presented in [Reiser et al. \(2008\)](#) and [Liang and Lauterbur \(2000\)](#).

2.2.1 Nuclear magnetic resonance

Measuring MR signals is based on the effect of nuclear magnetic resonance (NMR), which was discovered by [Bloch \(1946\)](#) and [Purcell et al. \(1946\)](#). Atomic nuclei with an odd number of protons or neutrons possess a non-zero nuclear spin \mathbf{I} that is related to a nuclear magnetic moment $\boldsymbol{\mu}_I$:

$$\boldsymbol{\mu}_I = \gamma \mathbf{I}, \quad (2.4)$$

with γ as the gyromagnetic ratio of nuclei. In a constant magnetic field \mathbf{B}_0 , these magnetic moments align lifting the degeneracy of energy levels (fig. 2.2 a). This phenomenon is described by the nuclear Zeeman effect and for hydrogen only two discrete states exist (fig. 2.2 b). The energy difference ΔE between both states is proportional to the magnetic field strength:

$$\Delta E = \gamma \hbar B_0, \quad (2.5)$$

with \hbar as the reduced Planck constant. In the case of hydrogen, the probability of occupancy is slightly higher for the parallel lower-energy state in comparison to the antiparallel higher-energy state. The excess of parallel states can be described by Boltzmann statistics and is very small in the order of 10^{-6} , but generates a macroscopic magnetization \mathbf{M} that is defined as the vector sum of expectation values of nuclear magnetic moments per unit volume V :

$$\mathbf{M} = \frac{1}{V} \sum_{i=1}^N \langle \boldsymbol{\mu}_I \rangle. \quad (2.6)$$

Applying a radio frequency (RF) pulse with perpendicular orientation to the direction of the magnetic field \mathbf{B}_0 and frequency $\omega_{\text{rf}} = \frac{\Delta E}{\hbar}$, the magnetization vector can be tipped away from its parallel alignment to the \mathbf{B}_0 -field by exciting spins into the higher-energy state. In this excited state the magnetization precesses about the direction of the magnetic

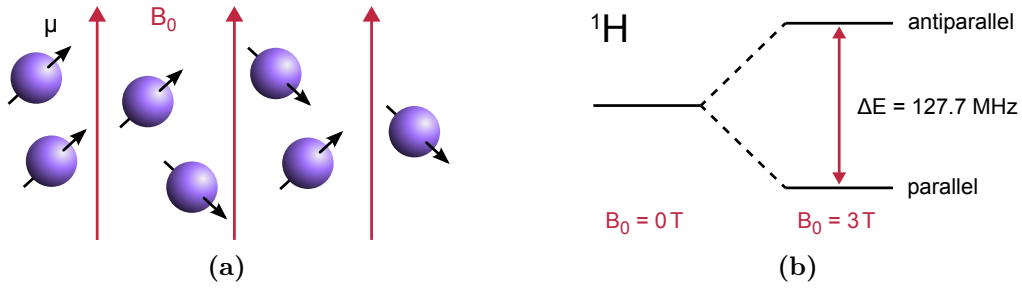


Figure 2.2: (a) Alignment of nuclear magnetic moments in the environment of a constant magnetic field B_0 ; (b) Zeeman splitting for hydrogen that results in two discrete states lifting the degeneracy of energy levels.

field B_0 with the Larmor frequency ω_L :

$$\omega_L = \gamma B_0. \quad (2.7)$$

The precession of the transversal component of magnetization about the axis of the magnetic field B_0 leads to an induction of a current in a receiver coil, which is proportional to the magnitude of the transversal component and can be measured as the MR signal.

Spin-spin interactions as well as interactions of spins with their environment cause a relaxation of magnetization back to equilibrium. These relaxation processes can be described by the Bloch equations (Bloch, 1946):

$$\frac{dM_x}{dt} = \gamma (\mathbf{M} \times \mathbf{B})_x - \frac{M_x}{T_2}, \quad (2.8)$$

$$\frac{dM_y}{dt} = \gamma (\mathbf{M} \times \mathbf{B})_y - \frac{M_y}{T_2}, \quad (2.9)$$

$$\frac{dM_z}{dt} = \gamma (\mathbf{M} \times \mathbf{B})_z - \frac{M_0 - M_z}{T_1}, \quad (2.10)$$

where M_0 represents the magnitude of the magnetization vector in equilibrium. The spin-lattice relaxation time T_1 describes the recovery of the longitudinal component of magnetization, which is caused by an energy transfer from the spin system to the surrounding lattice restoring thermal equilibrium (eq. 2.10 and fig. 2.3 a). In addition to that process, the transversal component of magnetization decays with the spin-spin relaxation time T_2 . Due to dipole-dipole interactions, local magnetic fields are disturbed resulting in different precession frequencies and finally in an irreversible decay of phase coherence of preceding spins (eq. 2.8, 2.9 and fig. 2.3 b). Local inhomogeneities of the magnetic field B_0 and a heterogeneous magnetic susceptibility of the probe cause further dephasing of spins accelerating the decay of the transversal component of magnetization. This faster decay is described by the characteristic time T_2^* . As the disturbing magnetic fields are constant in time, this process can however be reversed by applying a RF pulse that flips the magnetization vector by 180° .

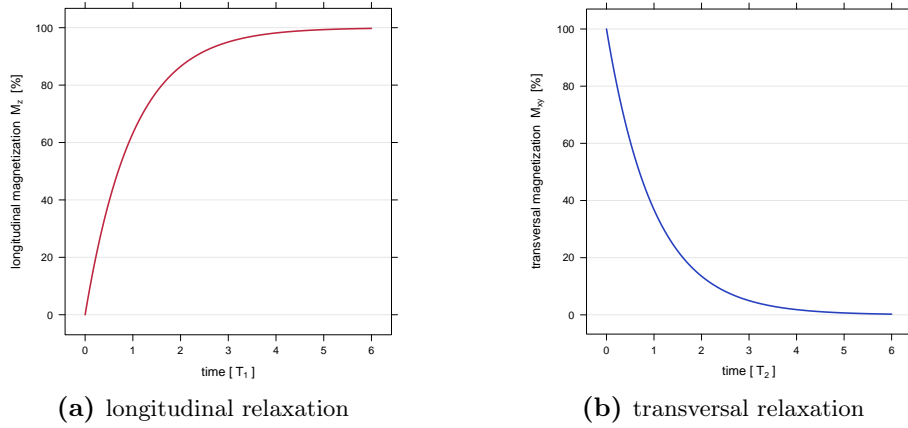


Figure 2.3: Temporal evolution of magnitudes of longitudinal (a) and transversal component (b) of magnetization after excitation with a 90° RF pulse (in units of T_1 and T_2). In biological tissues, T_1 is in the range of 300 - 2000 ms and T_2 is about 30 - 150 ms. The two curves represent solutions of the Bloch equations (eq. 2.10 as well as eq. 2.8, 2.9).

2.2.2 Magnetic resonance tomography

Signal localization and k -space interpretation

In order to obtain a spatial resolution of the MR signal, the constant magnetic field \mathbf{B}_0 is superimposed with a time- and location-dependent gradient field:

$$\mathbf{G}(t) = \frac{\partial B_z(t)}{\partial x} \mathbf{e}_x + \frac{\partial B_z(t)}{\partial y} \mathbf{e}_y + \frac{\partial B_z(t)}{\partial z} \mathbf{e}_z = G_x(t) \mathbf{e}_x + G_y(t) \mathbf{e}_y + G_z(t) \mathbf{e}_z, \quad (2.11)$$

with \mathbf{e}_x , \mathbf{e}_y and \mathbf{e}_z as unit vectors. As a result, the magnetic field as well as the Larmor frequency become dependent on the location \mathbf{r} :

$$\omega(\mathbf{r}, t) = \gamma B_z(\mathbf{r}, t) = \gamma (B_0 + \mathbf{r} \cdot \mathbf{G}(t)). \quad (2.12)$$

Applying the additional gradient field $\mathbf{G}(t)$ allows either only exciting a selected slice by tuning the RF to the Larmor frequency of that particular slice or encoding the MR signal with location-dependent phase or frequency. These phase and frequency encodings can be interpreted as certain points in the so-called k -space. The measured MR signal for each point in k -space is composed of the integrated transversal magnetization of the whole imaging volume. Varying the strength and direction of gradient fields $\mathbf{G}(t)$, arbitrary locations in k -space can be probed. The spatial distribution of the transversal magnetization, i. e. the intensity of individual voxels, then corresponds to the inverse Fourier transform of the measured MR signal. Whereas low frequencies at the k -space center are correlated with image contrast, high frequencies at outer areas yield image details and fine structure. There exist different schemes for probing the k -space, e. g. cartesian or radial sampling (fig. 2.4).

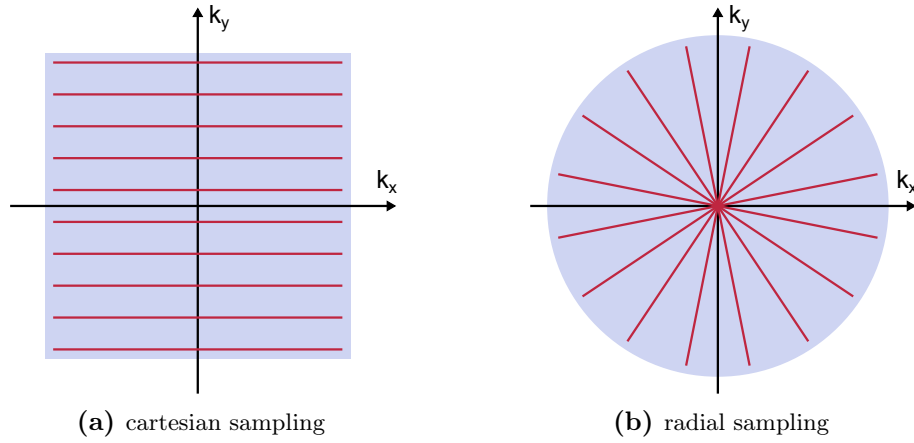


Figure 2.4: Different schemes for probing the k -space: red lines represent trajectories through k -space. The MR signal is then measured at discrete points along these trajectories. For cartesian schemes, magnetic gradient fields are used to move from k -space center to sampling start positions.

MRI contrasts

The process of measuring a MR image is described by the MR sequence that controls the RF excitation pulse, the gradients for spatial encoding as well as signal acquisition. In MRI, the intensity of a voxel depends on several parameters, mainly on its density of water and fat protons as well as its T_1 , T_2 and T_2^* relaxation times. Adjusting the echo time TE and repetition time TR in the sequence protocol determines which of these parameters has the strongest influence on the signal intensity of the voxel and thus the image contrast (fig. 2.5). A very short echo time ($TE \ll T_2^*$) and a long repetition time ($TR \gg T_1$) yields a proton density (PD)-weighted contrast. A T_2 - or T_2^* -weighting is achieved by an appropriate echo time and a long repetition time ($TR \gg T_1$). A very short echo time ($TE \ll T_2^*$) and an appropriate repetition time result in a T_1 -weighted image.

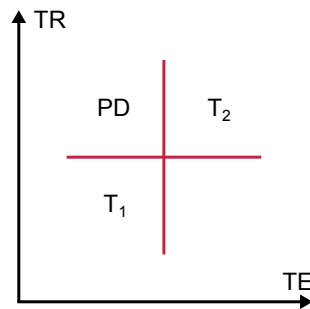


Figure 2.5: Dependence of the MRI contrast on the sequence parameters echo time TE and repetition time TR .

As a second possibility, a T_1 -weighted image contrast can be accomplished using a so-called inversion recovery sequence with magnetic preparation. At first, the longitudinal magnetization is inverted by a 180° RF pulse and starts relaxing back to its initial equilibrium state. After a certain inversion time TI the longitudinal magnetization at that moment is then flipped into the transversal plane by a 90° RF pulse and its magnitude is measured. Applying this technique, it becomes possible to suppress signals from tissue with a certain T_1 relaxation constant as the longitudinal magnetization passes the zero point when relaxing back to equilibrium.

2.3 Discriminant analysis

Discriminant analysis is a widely used multivariate statistical method that allows a common and simultaneous analysis of several observation variables of an object. A first simple form of this method was developed by [Fisher \(1936\)](#). It is a supervised learning approach that analyzes a training dataset that consists of measurements of several observation variables of objects and the corresponding object classes. Thus, a classification function is derived that should predict the correct class for a new object, for which the same observation variables were measured. For a more detailed description of the topics multivariate statistics and discriminant analysis, see [Hastie et al. \(2011\)](#), [Bouveyron et al. \(2007\)](#) and [Berge et al. \(2012\)](#).

2.3.1 Gaussian mixture model framework

Discriminant analysis is based on the Gaussian mixture model framework that assumes that each of the N observations $\mathbf{X}_1, \mathbf{X}_2, \dots, \mathbf{X}_N$ is an independent realization of a random vector $\mathbf{X} = (x_1, x_2, \dots, x_p)^T \in \mathbb{R}^p$. The density of a large number of observations can be written as:

$$f(\mathbf{X}) = \sum_{k=1}^K \pi_k f_k(\mathbf{X}, \boldsymbol{\mu}_k, \boldsymbol{\Sigma}_k), \quad (2.13)$$

where K is the number of classes and π_k is the class mixture proportion, which is equivalent to the a priori probability:

$$\pi_k = \frac{N_k}{N}, \quad (2.14)$$

with N_k as the number of observations in class k .

The term $f_k(\mathbf{X}, \boldsymbol{\mu}_k, \boldsymbol{\Sigma}_k)$ describes the Gaussian probability density of each class:

$$f_k(\mathbf{X}, \boldsymbol{\mu}_k, \boldsymbol{\Sigma}_k) = \frac{1}{(2\pi)^{p/2} |\boldsymbol{\Sigma}_k|^{1/2}} \exp(-1/2 (\mathbf{X} - \boldsymbol{\mu}_k)^T \boldsymbol{\Sigma}_k^{-1} (\mathbf{X} - \boldsymbol{\mu}_k)), \quad (2.15)$$

where $\boldsymbol{\mu}_k$ is the mean value per class:

$$\boldsymbol{\mu}_k = \frac{1}{N_k} \sum_{i=1}^{N_k} \mathbf{X}_i \quad (2.16)$$

and $\boldsymbol{\Sigma}_k$ represents the covariance matrix per class:

$$\boldsymbol{\Sigma}_k = \frac{1}{N_k - 1} \sum_{i=1}^{N_k} (\mathbf{X}_i - \boldsymbol{\mu}_k)(\mathbf{X}_i - \boldsymbol{\mu}_k)^T \quad (2.17)$$

$$= \frac{1}{N_k - 1} \sum_{i=1}^{N_k} \begin{pmatrix} X_{i1} - \mu_1 \\ \vdots \\ X_{ip} - \mu_p \end{pmatrix} \begin{pmatrix} X_{i1} - \mu_1, & \dots, & X_{ip} - \mu_p \end{pmatrix}. \quad (2.18)$$

The dimension of the covariance matrix is $p \times p$.

2.3.2 Process of classification

The idea of discriminant analysis is to assign one of K predefined classes C_1, C_2, \dots, C_K to an observation variables vector $\mathbf{X} \in \mathbb{R}^p$, which has an unknown class membership. The method can be divided into two parts:

- (1) In the learning step (fig. 2.6 a), a learning dataset that consists of N observation variables vectors \mathbf{X}_j labeled with their corresponding classes C_j is used to estimate the mixture proportion π_k (eq. 2.14) as well as the Gaussian model parameters mean value $\boldsymbol{\mu}_k$ (eq. 2.16) and covariance matrix $\boldsymbol{\Sigma}_k$ (eq. 2.17, 2.18) for each of the K classes.
- (2) The prediction step (fig. 2.6 b) is based on the Bayes theorem and a new observation variables vector \mathbf{X}_{new} is associated with that particular class k which has the maximum a-posteriori probability:

$$Pr(k|\mathbf{X}) = \frac{\pi_k f_k(\mathbf{X})}{\sum_{l=1}^K \pi_l f_l(\mathbf{X})}. \quad (2.19)$$

This optimal decision rule is equivalent to minimizing a cost function:

$$\delta^*(\mathbf{X}_{\text{new}}) = \operatorname{argmin}_{k=1, \dots, K} H_k(\mathbf{X}_{\text{new}}), \quad (2.20)$$

where the cost function is represented by the log-likelihood function:

$$H_k(\mathbf{X}_{\text{new}}) = -2 \log(\pi_k f_k(\mathbf{X}, \boldsymbol{\mu}_k, \boldsymbol{\Sigma}_k)). \quad (2.21)$$

Thus in practice, for each of the K classes costs are calculated and the class with lowest costs is predicted for the new observation. Inserting the Gaussian density function (eq. 2.15) into the cost function (eq. 2.21) leads in the general case, where covariance matrices of the

K classes are not assumed to be equal, to discriminant functions that are quadratic in \mathbf{X} :

$$H_k(\mathbf{X}) = (\mathbf{X} - \boldsymbol{\mu}_k)^T \boldsymbol{\Sigma}_k^{-1} (\mathbf{X} - \boldsymbol{\mu}_k) + \log(\det \boldsymbol{\Sigma}_k) - 2 \log(\pi_k) + C, \quad (2.22)$$

with a constant C that is equal for all classes. Therefore this type of classification is referred to quadratic discriminant analysis (QDA) and the quadratic functions can also be seen as decision boundaries in the p -dimensional observation variables space (fig. 2.6 b). In contrast, if it is assumed that all classes share the same covariance matrix $\boldsymbol{\Sigma}_k = \boldsymbol{\Sigma}$, the cost function term becomes linear and this special case is called linear discriminant analysis.

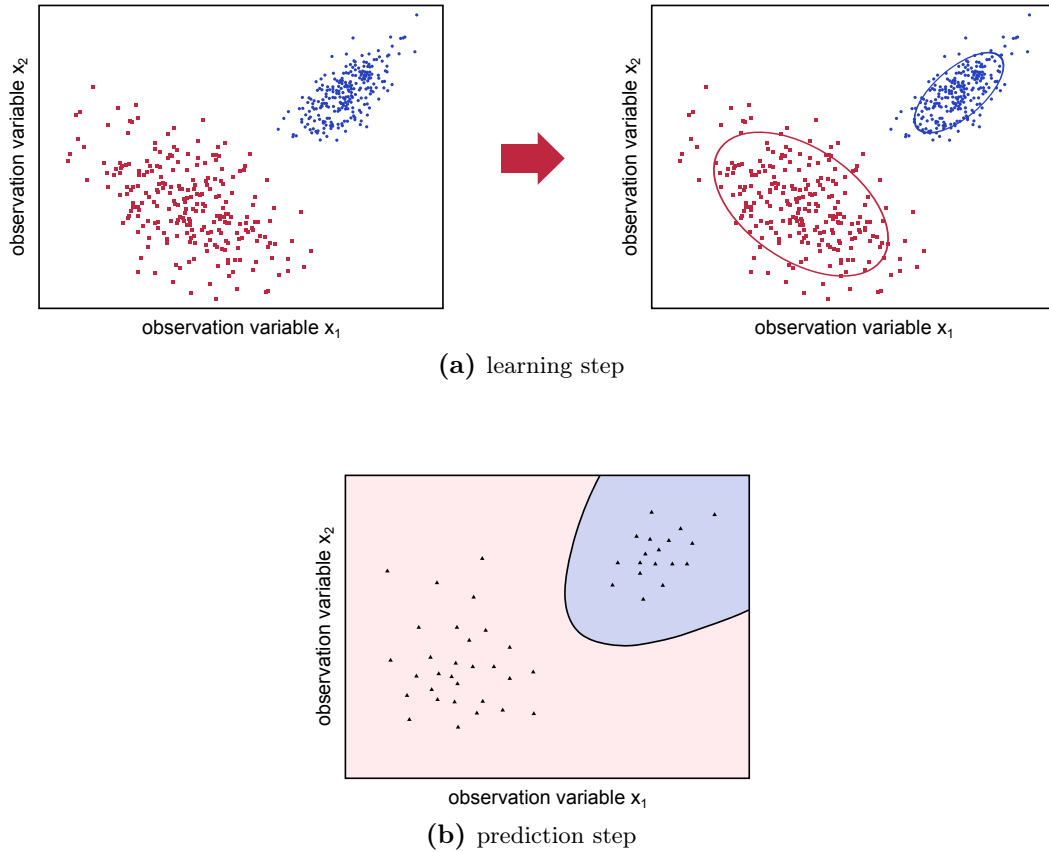


Figure 2.6: Principle of classification using QDA: for a learning dataset that consists of several observation variables vectors labeled with their corresponding classes (a, left), the mixture proportion π_k as well as the Gaussian model parameters mean value $\boldsymbol{\mu}_k$ and covariance matrix $\boldsymbol{\Sigma}_k$ are estimated for each of the K classes (a, right); (b) applying the Bayes theorem, parameter spaces of different classes can be separated by quadratic functions and new observations can be associated with a class by calculating the maximum a posteriori probability of the observation belonging to one of the K classes. Adopted from [Bouveyron \(2012\)](#).

2.4 Ion radiotherapy

Radiotherapy is applied to about half of all patients with malignant localized tumors (Schardt et al., 2010). The key challenge of radiotherapy is to balance the effects of the applied radiation on the target tissues and surrounding healthy tissues. On the one hand, the tumor target must receive a dose high enough to inactivate a sufficient number of cancer cells. On the other hand, the accumulated dose of the surrounding healthy tissue and organs at risk should be as small as possible to decrease the probability of severe side effects. Employing high-energy ion beams as radiation modality for treating tumors was first proposed by Wilson (1946) and offers several advantages compared to conventional photon radiotherapy. A detailed review about ion radiotherapy is provided by Schardt et al. (2010).

2.4.1 Physical and radiobiological aspects of ions

Interactions of charged particles with matter

Interactions of charged particles traversing matter differ from photon interactions. Mega-voltage photons mainly interact through the three processes photoelectric effect, Compton scattering and pair production resulting in an exponentially shaped depth-dose profile with an initial dose buildup (fig. 2.7). For ions at therapeutic energies up to several 100 MeV per nucleon, inelastic collisions with target electrons dominate the interaction cross-section. The mean energy loss per unit path length through these Coulomb interactions, also known as electronic stopping power S_{el} , can be described by the Bethe-Bloch formula (Bethe, 1930; Bloch, 1933b,a; Leo, 1994):

$$S_{\text{el}}(E) = - \left(\frac{dE}{dx} \right)_{\text{el}} \propto N_{\text{a}} \rho \frac{Z}{A} \frac{z^2}{\beta^2} \left[\ln \left(\frac{2 m_{\text{e}} c^2 \beta^2}{I (1 - \beta^2)} \right) - \beta^2 - \text{corr} \right], \quad (2.23)$$

with:

- N_{a} : Avogadro's number = $6.022 \times 10^{23} \text{ mol}^{-1}$,
- ρ : mass density of target material,
- Z : atomic number of target material,
- A : atomic weight of target material,
- z : charge of incident particle in units of e ,
- $\beta = v/c$ of the incident particle,
- m_{e} : electron mass,
- c : velocity of light,
- I : mean excitation potential,
- corr: term for density and shell correction.

The Bethe-Bloch formula (eq. 2.23) implies that the energy deposition of ions penetrating a medium increases with decreasing particle energy resulting in an inverse depth-dose profile compared to photons (Bragg and Kleeman, 1905) (fig. 2.7). Furthermore, the total path length of ions traversing tissue is finite and depends on the electron density $\rho_e = N_a \rho \frac{Z}{A}$ and the mean excitation potential I of the target material as well as on the energy of the incident particle. The consequence is a low dose in the entrance channel increasing towards the end of range. The maximum dose is reached in the so-called Bragg peak near the end of range followed by a sharp dose falloff at the distal end. Ions heavier than protons reveal a dose tail after the distal falloff that is caused by nuclear fragmentation. The ratio of dose peak to plateau is higher for carbon ions than for protons. Changing the particle energy allows a variation of the Bragg peak position in depth. For covering a target volume with a certain thickness in depth, ion beams of different energies are superimposed creating a spread-out Bragg peak (fig. 2.7). Considering the lateral beam spread, the deflection of ion beams is relatively small in comparison to photon beams and decreases with the atomic charge of the incident particle.

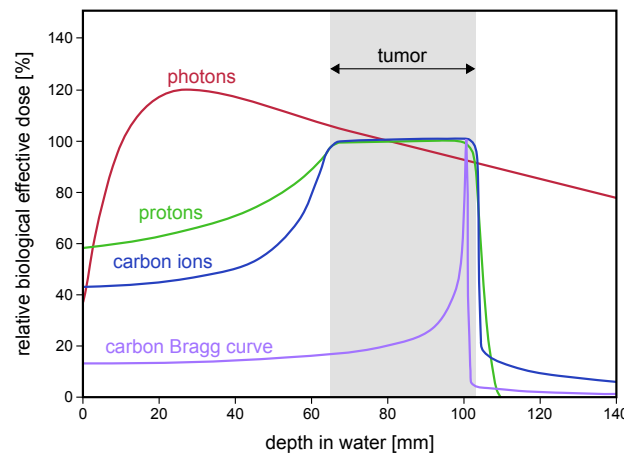


Figure 2.7: Depth-dose distributions of photons and ions. Photons show an exponentially shaped profile with an initial dose buildup (red curve), whereas ions have a low entrance dose and a characteristic dose peak, the so-called Bragg peak, near the end of range that depends on the particle energy (lila curve). For covering an extended tumor, ion beams of different energies are superimposed creating a spread-out Bragg peak (green and blue curves). Adopted from Gwosch (2012).

From the radiotherapy perspective, all these properties of ion beams are advantageous and allow a highly conformal physical dose deposition in the target volume sparing the surrounding healthy tissue. Furthermore, for ions heavier than helium the radiobiological efficiency in damaging cells is pronounced in the Bragg peak area (Scharadt et al., 2010). Thus employing heavy ions such as carbon as radiation modality, biologically effective dose distributions can be reached that even have a higher conformality than the corresponding physical dose distributions.

2.4.2 Treatment planning

The aim of treatment planning is to simulate and optimize the dose distribution within the patient before treatment and adjust treatment plans to clinical needs. The workflow includes a chain of several steps: after diagnosis, three-dimensional images of the patient are acquired and target contours and organs at risk are defined. For this procedure, both MR and CT images are employed.

In the following simulation step, beam parameters are specified and dose distributions are calculated and optimized. Here, the application of CT is the gold standard as it has a high geometrical accuracy and interaction processes of X-rays and ions show certain similarities. Both processes mainly depend on the electron density ρ_e of the target, but ion ranges are additionally influenced by the mean excitation potential I (eq. 2.1, 2.23 and 2.25).

After approval, treatment plans are translated into machine parameters of the particle accelerator and the active beam delivery system by defining the particle number and energy for each scanning spot. Finally, dose and setup are verified and treatment of a patient can start.

The concept of water equivalent path length

Treatment planning and simulation for ion radiotherapy is historically based on the assumption that targets are water-like. In order to account for heterogeneous tissue and calculate the required particle energy for shifting the Bragg peak to a designated depth, CT voxels have to be translated into a water-equivalent system in the beam's-eye view (Chen et al., 1979; Krämer et al., 2000). Thus, voxels of higher density than water elongate and low-density voxels shorten the beam path in the water-equivalent system. In this concept, the range of ions traversing a specific material is defined relative to water as the water equivalent path length (WEPL):

$$WEPL_{\text{material}} = \frac{r_{\text{water}} - r_{\text{material}}}{d}, \quad (2.24)$$

where r_{material} and r_{water} represent the positions in depth at 80 % or 90 % of the depth-dose curve maximum values at the distal fall offs for cases with and without an additional material slab of thickness d in the beam path (fig. 2.8).

Furthermore, the WEPL of a material can be well approximated by the ratio of stopping powers of that particular material and water (compare eq. 2.23):

$$WEPL_{\text{material}} \propto \frac{\rho_{e, \text{material}}}{\rho_{e, \text{water}}} \times \frac{\left[\ln \left(\frac{2 m_e c^2 \beta^2}{I_{\text{material}} (1 - \beta^2)} \right) - \beta^2 \right]}{\left[\ln \left(\frac{2 m_e c^2 \beta^2}{I_{\text{water}} (1 - \beta^2)} \right) - \beta^2 \right]}. \quad (2.25)$$

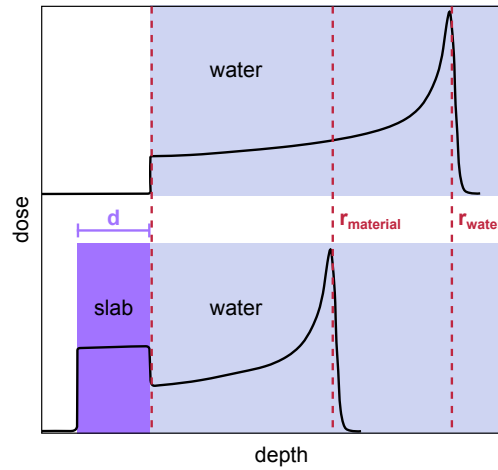


Figure 2.8: Principle of WEPL concept: the positions in depth at 80 % or 90 % of the depth-dose curve maximum values at the distal fall offs for cases with and without an additional material slab in the beam path are measured. The difference of the two range values divided by the thickness of the slab is called WEPL.

Hounsfield look-up table

For the simulation of treatment plans, CT numbers of voxels have to be translated into WEPL values. Therefore, a so-called Hounsfield look-up table (HLUT) is employed correlating CT numbers and WEPL values by approximating a functional relationship between the two quantities. For setting up an empirical HLUT both quantities are measured for tissue equivalent materials covering the whole CT scale and regions between measurement points are linearly interpolated (Jäkel et al., 2001a).

A second approach is a stoichiometric calibration (Schneider et al., 1996). This approach is commonly used as clinical standard because it provides smaller uncertainties in comparison to the empirical approach. In a first step, a mathematical model is used to parametrize the photon attenuation cross-section into scanner-specific and material-specific parameters by measuring materials of known chemical composition. Applying the model with calibrated scanner-specific parameters to any material with known composition, its CT number, when measured in the particular scanner, can be predicted. In a second step, scanner-specific CT numbers and corresponding WEPL values are theoretically derived from known tabulated tissue compositions from literature and a HLUT can be established similarly to the empirical approach.

Interfractional and intrafractional changes of anatomy

CT examinations used for treatment plan simulation in ion radiotherapy are usually acquired before the first fraction of treatment. Major uncertainties in the treatment process are interfractional and intrafractional changes of patient anatomy (Bert and Durante, 2011). Interfractional changes may occur between the day of the CT examination for treatment

plan simulation and the days of treatment. Examples are an organ and tumor movement, tumor growth or shrinkage, a filling of an air cavity with mucus or a gain or loss of weight of the patient. In contrast, intrafractional changes may appear during treatment, e.g. due to breathing. Any of these changes will impair the dose coverage of the tumor target if they affect the position of the tumor or regions along the beam path altering the ion ranges. For compensation, a replanning of treatment would be required adapting treatment plans to these changes. Further CT examinations for new treatment plan simulations would be necessary, e.g. before each fraction or even during treatment. However, supplementary CT examinations are rarely carried out due to the additional dose to the patient.

Therefore in practice, margins are defined around the clinical target volume. They are adjusted to the expected anatomical changes between and during fractions as well as to uncertainties of patient setup and intrinsic uncertainties, which result from the conversion of CT to WEPL (Paganetti, 2012). However, margins increase dose to healthy tissue leading to a reduction of the therapeutic window. For that reason, the definition of margins is usually a trade-off between a better dose coverage of the tumor volume and the probability of side effects.

Considering the high conformality of ions and their finite range in tissue, errors introduced in the treatment planning process are more critical compared to photon treatment planning. Furthermore, errors are systematical affecting all fractions of a treatment in contrast to statistical deviations, such as errors in patient fixation, that fluctuate around zero between fractions.

Application of MRI for treatment plan simulation

The application of MRI for treatment plan simulation is difficult as information about tissue composition gained from MRI differs from CT and no physical relationship between MR signal intensities and WEPL values exists. Therefore establishing a HLUT for translation of MR signals to WEPL is not possible and more sophisticated methods are necessary.

In the literature, two different approaches for a similar problem, the derivation of pCT numbers from MR images, can be found. They are suggested for treatment plan simulation in conventional photon radiotherapy and attenuation correction for hybrid MRI/PET devices.

A first approach deals with *atlas-based methods* (Hofmann et al., 2008; Wang et al., 2008; Greer et al., 2011; Dowling et al., 2012). An atlas is generated by a rigid coregistration of a template MR image with a corresponding template CT image of a patient. Then, for any new patient or the same patient at a later day of treatment, a new MRI examination is carried out. A deformable, non-rigid registration between the template MR image and the new MR image is employed to warp the template CT image to the anatomy of the examined patient creating a pCT. The performance of this approach mainly depends on the accuracy and robustness of the applied non-rigid registration algorithm.

A second approach consists of *classification-based methods*, which group single tissue voxels or whole tissue volumes into several classes that are correlated with certain bulk CT numbers (Boettger et al., 2008; Stanescu et al., 2008; Catana et al., 2010; Keereman et al., 2010; Johansson et al., 2011; Berker et al., 2012; Edmund et al., 2012; Johansson et al., 2012). This classification can be accomplished by point-based methods, which use the absolute signal intensities of single voxels or edge detection. More sophisticated techniques are region-based methods, which further analyze information from neighbors of voxels, e.g. mean values or textures, as well as model-based methods, which employ prior knowledge about segmented objects, e.g. the shape of objects. A more detailed description of image classification and segmentation can be found in Jähne (2005).

3 | Materials and methods

In this chapter, important materials and methods used for the experiments are introduced. Sections 3.1 and 3.2 describe tissue samples and patients for which measurements were carried out. In sections 3.3 and 3.4, CT and MRI scanners as well as imaging protocols and sequences are specified. Section 3.5 presents a tool used for image registration. An overview of the *MMclassification* package, a framework implemented for deriving pCT numbers from MR images is given in section 3.6. Section 3.7 describes software employed for the experiments treatment plan simulation and treatment plan adaptation.

3.1 Tissue samples

Until now, there exist no artificial crafted phantoms that can simulate photon and ion interaction properties as well as MR relaxation characteristics of living tissue. Therefore, three mangos and three pieces of pork meat were used as multimodal phantoms (fig. 3.1). The mangos had a high content of water, which is important for MRI measurements, and were durable for several days. They consisted of a pit in the center that was surrounded by air and fruit flesh. Thus, they could represent air and two soft tissue classes. Meat samples were composed of fatty tissue, muscle and bones and covered a wider range of MR relaxation parameters and attenuation properties for photons and ions in living tissue (table 3.1). For measurements, meat samples were placed in a bowl made out of paper and for a reproducible alignment using the laser cross-hairs of CT and MRI scanners, pen markers were added on the surfaces of all samples.

3.2 Patients

In addition, datasets of three patients with tumors in the head region scheduled for ion radiotherapy at the Heidelberg Ion-Beam Therapy Center (HIT) were employed for the study. For each of the selected patients, CT data of the head region of a standard radiotherapy treatment planning protocol was available and for each of them an examination at the Siemens Magnetom Trio Tim MRI scanner at the German Cancer Research Center (Deutsches Krebsforschungszentrum) (DKFZ), was arranged.



Figure 3.1: Mangos and meat samples used for measurements: meat samples were placed in a bowl made out of paper and wrapped in a foil. For a reproducible alignment using the laser cross-hairs of CT and MRI scanners, pen markers were added on the surfaces of all samples. Meat sample 3 is not shown.

3.3 CT equipment and protocols

CT measurements were performed at several CT scanners from the company Siemens AG, Healthcare Sector, Erlangen (Germany). The Somatom Definition Flash scanner at DKFZ is a dual source CT scanner providing two X-ray tubes. In a dual energy mode, the tubes can be operated at two combinations of different X-ray spectra peak voltages (80/140 kVp and 100/140 kVp). For a better separation of low and high voltage X-ray spectra, a tin filtration can be applied to the higher voltage tube, which absorbs low energy photons. The Somatom Sensation 4 and Somatom Sensation Open scanners were located at the “Kopflinik” of the Heidelberg University Hospital. Both scanner types employ single energy X-ray spectra with peak voltages of 120 kVp.

3.4 MR equipment and sequences

MR images were acquired at DKFZ on a Magnetom Trio Tim MRI scanner with a main magnetic field strength of 3 T manufactured by Siemens AG, Healthcare Sector, Erlangen (Germany). For image acquisition, the following pulse sequences were employed:

TSE sequence

The turbo spin echo (TSE) sequence is a two-dimensional spin echo technique that uses multiple phase-encoded echoes for faster k -space sampling and thus allows for a shorter image acquisition time in comparison to conventional spin echo sequences.

tissue	relative electron density ρ_e	T_1 [ms]	T_2 [ms]
subcutaneous fat	0.951 ^a	371 ^d	133 ^d
skeleton - yellow marrow	0.982 ^a	365 ^d	133 ^d
brain - white matter	1.035 ^a	1084 ^c	69 ^c
brain - gray matter	1.035 ^a	1820 ^c	99 ^c
muscle	1.040 ^a	1412 ^c - 1420 ^d	32 ^d - 50 ^c
kidney	1.041 ^a	1194 ^c	56 ^c
blood	1.050 ^a	1932 ^c	275 ^c
liver	1.050 ^a	812 ^c	42 ^c
skeleton - cartilage	1.083 ^a	1156 ^c - 1240 ^d	27 ^c - 43 ^c
skeleton - cortical bone	1.781 ^a	140 ^b - 260 ^b	0.42 ^b - 0.50 ^b

Table 3.1: MR- and CT-related parameters for tissue from literature: ^a(Bazalova et al., 2008), ^b(Reichert et al., 2005), ^c(Stanisz et al., 2005), ^d(Gold et al., 2004). All measurements were performed in vivo at 3 T. Values for cortical bone were measured at 1.5 T and represent the relaxation time T_2^* .

MPRAGE sequence

The magnetization prepared rapid acquired gradient echo (MPRAGE) sequence is a three-dimensional gradient echo method with low-flip angle excitation that applies a magnetic preparation pulse for T_1 -weighting before signal acquisition.

UTE sequence

The applied ultrashort echo time (UTE) sequence is based on a three-dimensional gradient echo technique with low-flip angle excitation. It features dual echo image acquisition and very short echo times ($TE \leq 0.5$ ms), which are achieved by a radial sampling of k -space, in contrast to probing the signal along lines of a cartesian grid (fig. 2.4). This sampling scheme has the advantage that signal acquisition can start after the RF excitation pulse with very short delay. In three dimensions, signal acquisition is represented by sampling along lines from the center of k -space towards the surface of a sphere around the k -space center (fig. 3.2 a). With this technique it becomes possible to measure non-zero signal intensities of compact bone tissue and thus distinguish bones from air. In contrast, with standard MR sequences a discrimination is not achievable due to very low signal intensities of bones caused by their very short T_2 and T_2^* relaxation times (fig. 3.2 b - d).

3.5 Image registration

A registration toolbox that was developed at DKFZ¹ was used for image registration (Floca, 2009). For coregistering a moving image to a target image, the rigid multi-resolution algorithm *dtmbHS4_multiRes.dll* was employed. This algorithm is based on maximization

¹written by Andreas Jäger (DKFZ)

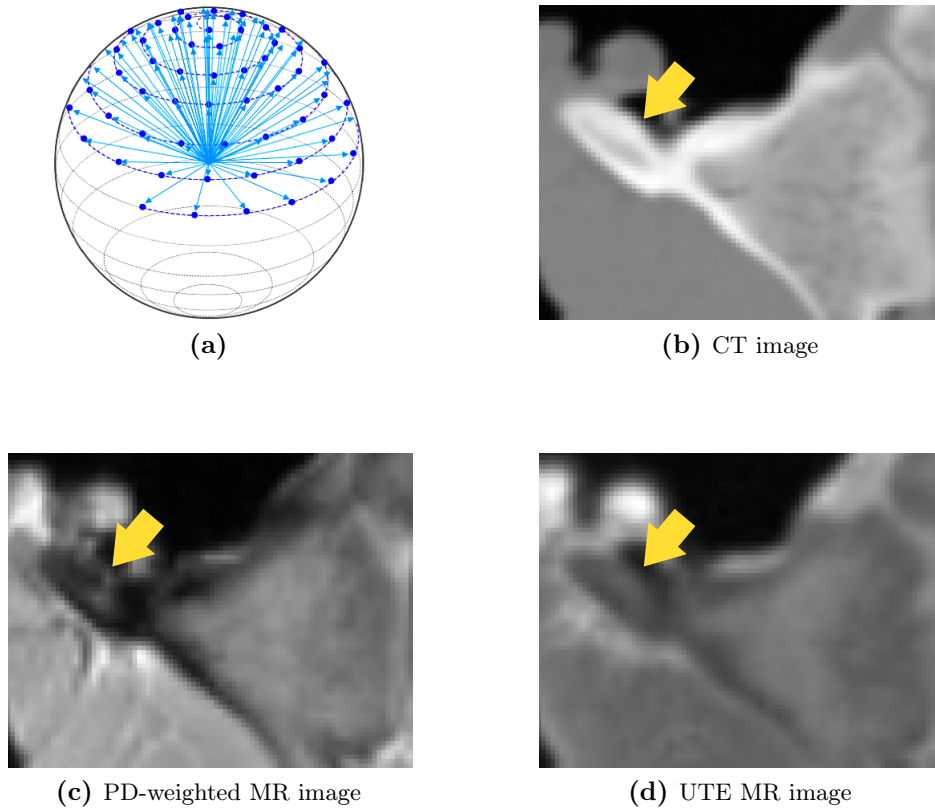


Figure 3.2: (a) 3D radial k -space sampling of applied UTE sequence, adopted from [Jellus \(2010\)](#); (b - d) examples of MR and CT images of bones.

of mutual information and in the registration process, only translation and rotation are allowed as degrees of freedom (fig. 3.3). Moving images are resampled to target image resolution in all dimensions by linear interpolation.

3.6 MMclassification package

3.6.1 Statistical computing language R

R is an open source implementation of S , a programming language for statistical computing and graphics (The R Foundation for Statistical Computing, ([R Development Core Team, 2012](#))). It provides a multi-platform software environment and features the extension of its implemented statistical techniques by installing so-called packages. These additional packages are developed by a large user community and cover a wide range of applications.

3.6.2 Package overview

In the course of this work, the package multimodal classification (*MMclassification*) was developed in the language R . It provides a framework of functions for reading and processing

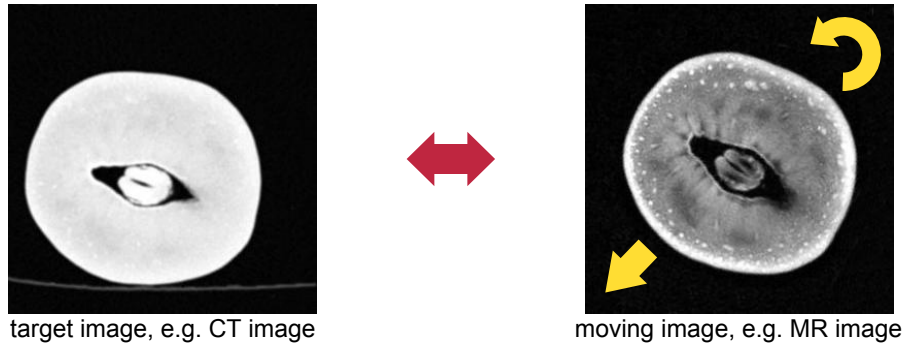


Figure 3.3: Principle of image registration. In the rigid registration process, only translation and rotation are allowed as degrees of freedom.

MR and CT images in order to derive pCT numbers from MR images. Several image processing features are included in the package. The majority of functions are optimized for parallel computing and low memory usage as for a voxelwise classification of medical images processing of huge datasets is necessary. For classification of voxels into CT classes, the high dimensional discriminant analysis (HDDA) algorithm from the package *HDclassif* (version 1.2.1 ([Bouveyron et al., 2007](#); [Berge et al., 2012](#))) is employed. Reading of medical images stored in the Digital Imaging and COmmunication in Medicine (DICOM) file format is realized with the package *oro.dicom* (version 0.3.3). Diagrams and plots of results are created with the *lattice* package (version 0.20.6). A diagram with a complete overview of functions of the *MMclassification* package, a table with a list of used packages and examples of program code for operating the package can be found in the appendix [A](#).

3.6.3 Workflow for derivation of pseudo CT

The process of deriving pCT numbers from MR images starts with a manual definition of input parameters, e.g. image resolution, file paths and which of the additional features and image processing steps are activated (fig. 3.4). Then, further parameters are derived automatically from MR images, e.g. air margins at borders of the images and binary masks. In the next step, MR and CT images selected for learning are loaded, additional features are extracted and the learning database is created. Afterwards, the reading process is repeated for MR and CT images chosen for the prediction of pCT numbers. A pCT is then predicted employing the learning database and the loaded MRI data for prediction. Finally, the resulting pCT is compared to its corresponding rCT by calculating a difference map, further evaluation of data is computed and results are exported to files that are saved to hard disc. Besides the first manual definition of input parameters, the entire process is fully automated.

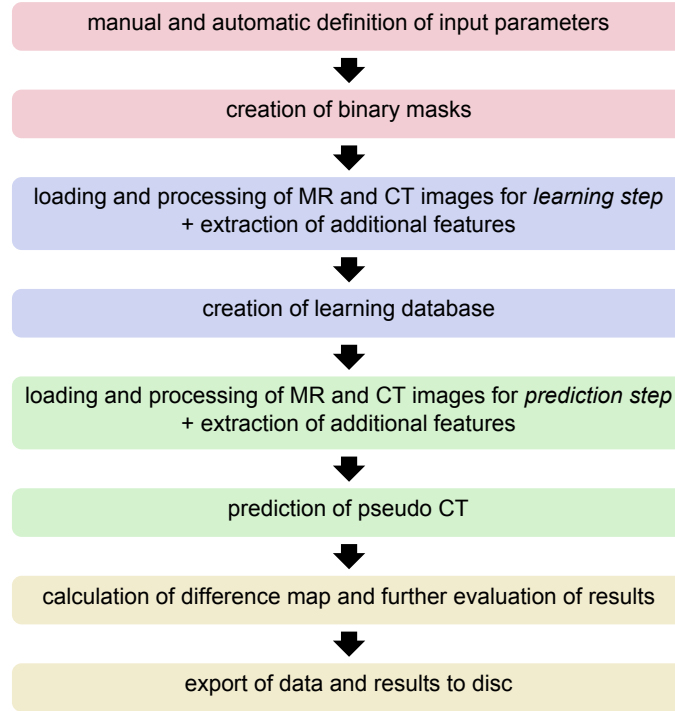


Figure 3.4: Workflow of *MMclassification* package for reading and processing MRI and CT data in order to derive pCT numbers from MR images.

3.6.4 Image processing

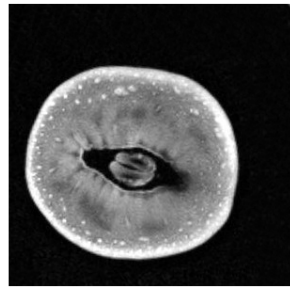
Masking

For each sample a binary mask is created separating the object from surrounding air (fig. 3.5 b). This step circumvents a misclassification of the surrounding air voxels and thus reduces overall errors. In addition, computing time for additional feature extraction and classification is reduced by excluding the surrounding air from computations. Evaluation of data refers only to voxels within the masks.

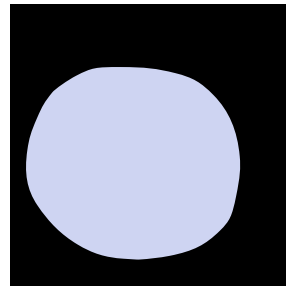
Masking is accomplished by simple region growing. For each row and column of an image slice, growing starts at the two outer ends proceeding towards the center until a threshold value is exceeded.

Additional feature extraction

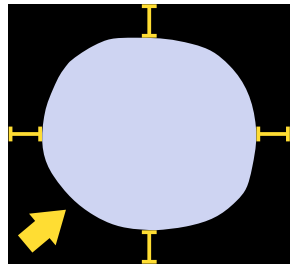
Additional features can be extracted for each voxel in order to augment the information provided by signal intensities of single voxels. For each voxel, additional information can be derived from all of the 26 surrounding voxels of a $3 \times 3 \times 3$ box (fig. 3.5 e) and from its location (fig. 3.5 f).



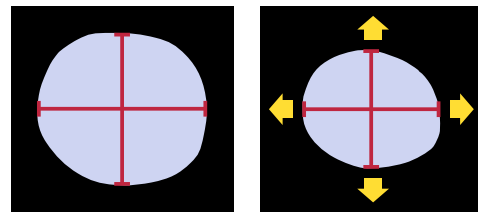
(a) sample image



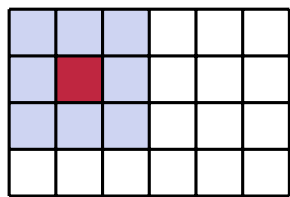
(b) masking



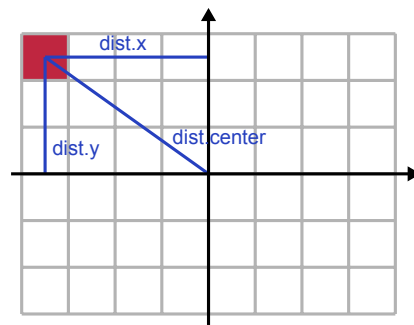
(c) global coordinate system



(d) global scaling



(e) from neighbors of a voxel



(f) from coordinates of a voxel

Figure 3.5: Image processing steps (a - d) and additional feature extraction (e, f) before classification implemented in the *MMclassification* package.

The following features are implemented:

- *box.mean*: the mean intensity of the surrounding box including the central voxel
- *box.sd*: the standard deviation of the surrounding box including the central voxel multiplied by the intensity of the voxel
- *dist.xyz*: the three absolute distances of the voxel to the center of the 3D imaging volume in each spatial dimension
- *dist.center*: the absolute distance of the voxel to the center of the 2D slice

Neighborhood-related features may improve results at transitions, e. g. standard deviations of boxes at transitions are larger than at homogeneous sites. Coordinate-related features assume a certain symmetric spatial distribution of tissue classes, in particular a cylindrical symmetry for *dist.center* and a spherical symmetry for *dist.xyz*. Improved classification results are then obtained in cases, in which a certain tissue class has similar spatial distributions in all samples.

Global coordinate system and global scaling

As the additional features *dist.xyz* and *dist.center* are coordinate-related, image masks of samples can be used for translating coordinates into a common global coordinate system (fig. 3.5 c). Thus, all samples can be centered in the coordinate system of images.

In addition, scaling factors can be calculated virtually equalizing the maximal expansion of masks of all samples in each coordinate direction (fig. 3.5 d). This procedure may improve results of coordinate-related additional features as geometries of patients become more similar.

3.6.5 HDDA algorithm

The HDDA algorithm employs supervised learning for classification of data. It assumes, according to the classical Gaussian mixture model framework, that class conditional densities are Gaussian and it is closely related to the well-known QDA. For classification of data, calculations similar to the description in section 2.3.2 have to be carried out. To increase efficiency in computing time compared to QDA and to circumvent the curse of dimensionality (Berge et al., 2012), it is assumed that high-dimensional data is located around subspaces with a lower dimension than p . This leads to a reduction of the number of dimensions during the learning step and for each of the K classes only the dimensions containing most information for discrimination from other classes are maintained. The algorithm offers a threshold parameter for dimension selection that has a default value of 0.20 and several models with different assumptions concerning the datasets can be selected.

3.7 Software for treatment plan simulation and adaptation

3.7.1 VIRTUOS

The VIRTUal RadiOtherapy Simulator (VIRTUOS), developed at DKFZ, represents the graphical front-end to the radiotherapy treatment planning system VOXELPLAN ([Schlegel et al., 1992](#); [Bendl et al., 1993](#)). It offers tools covering the complete treatment planning process. In this work, the following functions were of importance:

- import of CT cubes created in R
- definition of target volumes in a three-dimensional patient model
- optimization of photon fields to designated target volumes
- three-dimensional dose calculation of photon treatment plans
- import of treatment plans and dose cubes from TRiP98
- visualization and evaluation of imported treatment plans and dose distributions

3.7.2 TRiP98

The software TReatment plannIng for Particles 98 (TRiP98) from GSI Helmholtzzentrum für Schwerionenforschung (GSI), Darmstadt (Germany) is a treatment planning system especially designed for applications in ion radiotherapy ([Krämer et al., 2000](#); [Jäkel et al., 2001b](#)). It allows a physical and biological calculation and optimization of three-dimensional dose distributions. The optimization is an inverse planning process and furthermore assumes a raster-scanning ion beam. Data exchange is compatible with VOXELPLAN file formats that an import of delineated target volumes from VIRTUOS and an export of optimized dose cubes is possible.

4 | Experiments and results

In this chapter, experiments concerning MRI-based treatment plan simulation and results achieved in these experiments are presented. The chapter is divided into four main parts: (1) In sections 4.1 and 4.2, CT and MR image acquisition are described (fig. 4.1 a). (2) Section 4.3 illustrates the evaluation of appropriate MR sequences and parameters for deriving pCT numbers from MR images (fig. 4.1 b). Cross-validation studies of three mangos, three meat samples and data of three patients are carried out in order to minimize errors of pCTs compared to a rCT. (3) Results obtained in simulations of carbon ion, proton and conventional photon treatment plans employing pCTs of meat samples and of patients can be found in sections 4.4 and 4.5 (fig. 4.1 c). (4) A test of the application of MRI for treatment plan adaptation to interfractional changes of anatomy is carried out in section 4.6 (fig. 4.1 d). Results of meat samples presented in this chapter have been published in “Radiation Oncology” (Rank et al., 2013).

4.1 CT image acquisition

4.1.1 Tissue samples

CT images of tissue samples were acquired on the Somatom Definition Flash CT scanner in dual energy mode. The scanner protocol *DE_Abdomen_LiverVNC* with X-ray spectra peak voltages of 80 kVp and 140 kVp with additional tin filtration were used. Effective tube current-time products were 210 mAs and 81 mAs respectively. Image reconstruction from raw data was accomplished with a D30s kernel. A slice thickness of 1.0 mm and a field of view (FOV) of 256 mm were chosen resulting in an in-plane resolution of 0.50 mm.

4.1.2 Patients

CT images of patients from external treatment planning examinations at the Heidelberg “Kopfclinik” were used as CT data. The patients were examined at Somatom Sensation 4 and Somatom Open scanners. Parameters were equivalent to the clinical ion radiotherapy treatment planning head protocol at HIT *01_HIT_BPL_Schaedel_S4* and *01_HIT_BPL_Schaedel_SO*. Patients were fixated with a mask in a similar head position as used for irradiation at HIT. The X-ray spectra peak voltage was 120 kVp and an effective

tube current-time product of 264 mAs was specified. Images were reconstructed from raw data using a H40s kernel. The slice thickness was 3.0 mm and the FOV was 310 mm resulting in an in-plane resolution of 0.61 mm.

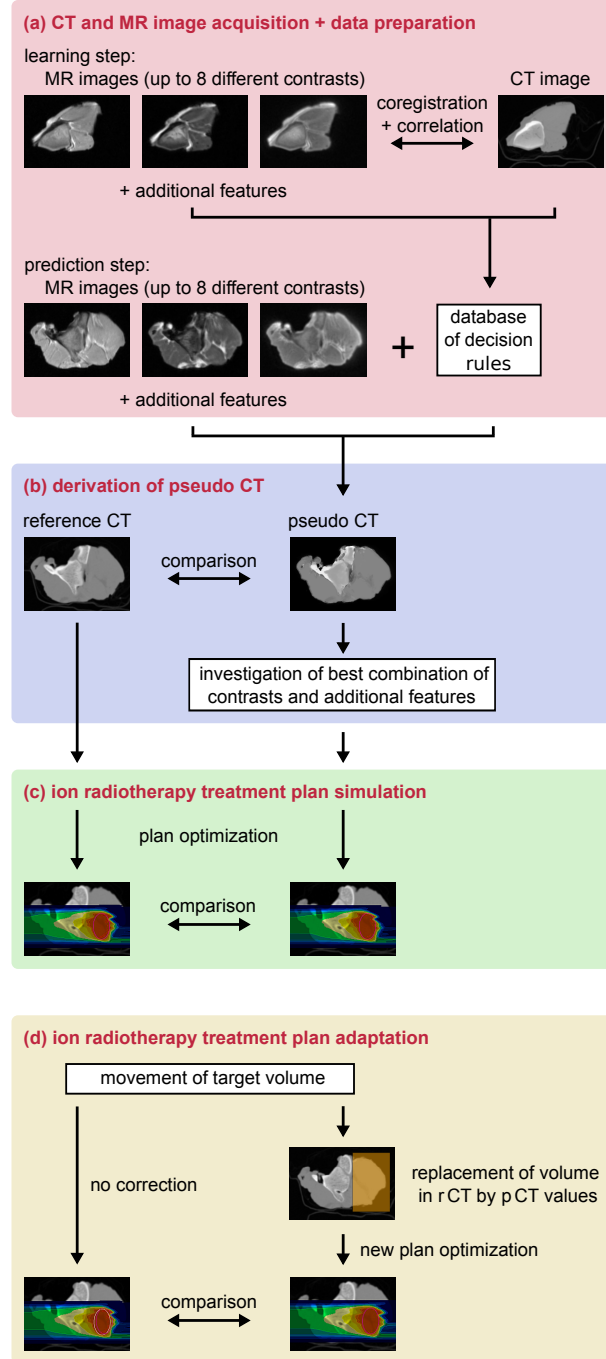


Figure 4.1: Overview of experiments and workflow: (a) CT and MR image acquisition as well as data preparation for classification; (b) derivation of p CT numbers from MR images with cross-validation studies for investigating the best combination of contrasts and additional features; (c) simulation of ion and photon treatment plans on p CTs and r CTs; (d) evaluation of the application of MRI for treatment plan adaptation.

4.2 MR image acquisition

4.2.1 Tissue samples

MR image acquisition of tissue samples was performed on the Magnetom Trio Tim 3 T MRI scanner at DKFZ. Samples were placed in the 12-channel head coil. For mangos sets of seven and for meat samples sets of eight image series with various contrasts were acquired. The TSE sequence with PD- (TSE1, TSE2) and T_2 -weighting (TSE3), the MPRAGE with T_1 -weighting and the dual echo UTE (UTE1, UTE2) sequence were used (table 4.1). For the UTE sequence, the first echo time was chosen as short as possible (Kjer et al., 2012) and the second echo time was adjusted so that water and fat spins were in phase (Rahmer et al., 2007). For all sequences an equivalent FOV of 256 mm was defined. The TSE and MPRAGE sequences had a nominal resolution of $1.0 \times 1.0 \times 2.0 \text{ mm}^3$, whereas the nominal resolution of the UTE sequence was isotropic with $1.0 \times 1.0 \times 1.0 \text{ mm}^3$. The bandwidth of TSE and UTE sequences was $501 \frac{\text{Hz}}{\text{Px}}$ and for the MPRAGE sequence it was $400 \frac{\text{Hz}}{\text{Px}}$. An automatic distortion correction filter and a correction of inhomogeneous coil illumination were activated in each sequence protocol.

CT and MRI measurements of tissue samples were performed at the same day. The MRI coil configuration, MR sequence protocols and sample locations in the head coil were equal for all samples. Variations of absolute signal intensities between samples were low and a further normalization of intensities was not applied to tissue samples.

sequence	echo time [ms]	repetition time [ms]	flip angle [°]	scan time [min]	additional parameters
TSE1	8.3	7500	90	4.8	turbo factor = 7
TSE2	8.3	7500	90	4.8	with fat sat, turbo factor = 7
TSE3	75.0	7500	90	3.8	turbo factor = 9
MPRAGE	2.38	2000	12	6.4	inversion time = 700 ms
UTE1	0.05 4.91	7.25	12	6.1	radial views = 50001
UTE2	0.05 4.91	7.25	60	6.1	radial views = 50001
UTE3	0.05 4.91	7.25	12	7.8	radial views = 39999, with fat sat

Table 4.1: Parameter settings of applied MR sequences. TSE1, TSE3, MPRAGE, UTE1 and UTE2 were employed for measurements of mangos. All sequences besides UTE3 were used for meat samples. Patient data was acquired applying TSE1 and UTE3.

4.2.2 Patients

Patient data was acquired at clinical MRI examinations of patients with tumors in the head region scheduled for ion radiotherapy and carried out on the Magnetom Trio Tim 3 T MRI

scanner employing the 12-channel head coil. Parameters of clinical sequence protocols were not equal for all patients and image data from these sequences could not be used for the derivation of pCT numbers for that reason. Therefore additional MR sequence protocols, especially chosen for this study, were applied. Due to a limited examination time, only a set of three contrasts could be acquired in addition to the standard clinical protocol. The TSE sequence with PD-weighting (TSE1) and the dual echo UTE sequence were selected (UTE3) (table 4.1). In the UTE sequence protocol fat saturation was activated in order to reduce illumination artifacts at the transitions between the surface of head and air (fig. 4.2). The FOVs, nominal resolutions and additional sequence settings for automatic distortion correction and correction of inhomogeneous coil illumination were similar to the parameters used for tissue samples.

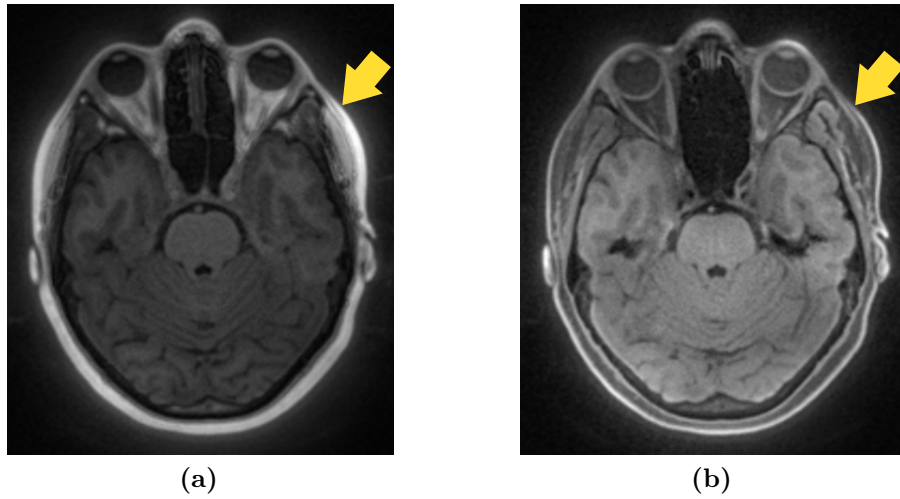


Figure 4.2: Examples of UTE images of the human brain with different settings: (a) without fat saturation; (b) with fat saturation.

For each patient, the CT and MRI examinations were carried out on two consecutive days. Considering coil configurations, both head and neck coils were connected for patient 1 and 3, but only the head coil was activated in the sequence protocol. In the examination of patient 2 solely the head coil was connected and activated. Due to these different coil configurations, absolute signal intensities of additionally acquired MR sequences showed large variations between patients. Differences in similar regions of the brain were up to 68 %. Therefore signal intensities of voxels were corrected with normalization factors calculated individually for each patient. The mean intensities of several regions of interest, e. g. the brainstem or brain grey matter, were measured with the free image analysis software *ImageJ* in PD-weighted and UTE images for each patient (table 4.2). Then, the mean value of signal ratios of regions of interest between patients was used as normalization factor.

sequence	location	patient 1 mean [a.u.]	patient 2 mean [a.u.]	patient 3 mean [a.u.]
TSE1	brainstem	934.8	678.2	900.4
TSE1	eye (right)	1531.9	1082.0	1764.3
TSE1	brain: lateral ventricle (right)	1983.7	1366.4	2000.5
TSE1	brain: grey matter (right)	962.1	689.3	1028.8
TSE1	brain: grey matter (left)	987.3	686.1	1047.0
TSE1	brain: white matter	1366.5	1003.4	1485.3
UTE3 echo1	brainstem	449.9	304.0	428.6
UTE3 echo1	brain: grey matter (right)	425.9	271.7	442.3
UTE3 echo1	brain: grey matter (left)	430.8	267.6	449.1
UTE3 echo2	brainstem	500.4	418.7	458.5
UTE3 echo2	brain: grey matter (right)	451.7	399.4	402.7
UTE3 echo2	brain: grey matter (left)	470.0	391.8	405.5
normalization factors				
	patient 1	(1.00)	1.39	1.00
	patient 2	0.73	(1.00)	0.74
	patient 3	1.00	1.40	(1.00)

Table 4.2: Measurement and calculation of normalization factors for compensating varying absolute signal intensities in MR images of patients.

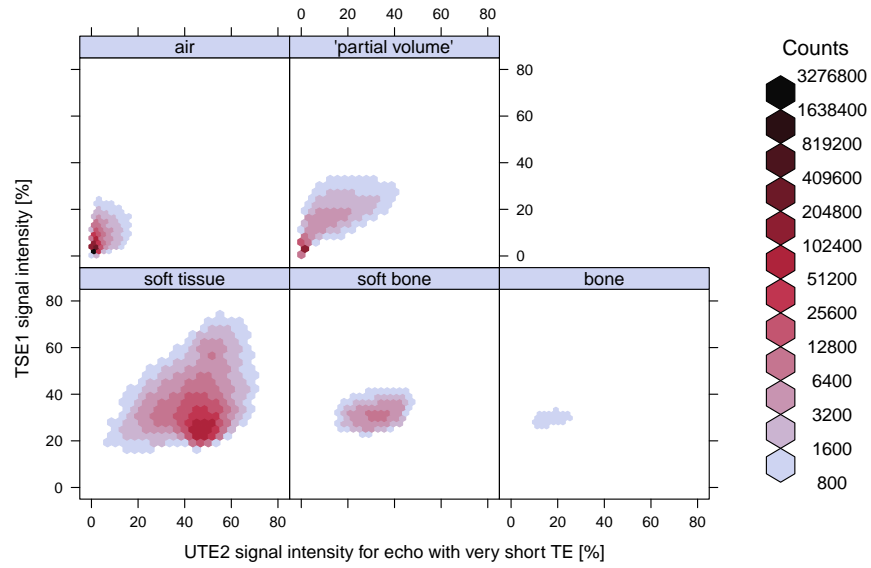
4.2.3 Distribution of absolute MR signal intensities

For evaluation, the distributions of absolute MR signal intensities of five tissue types, namely air, “partial volume”, soft tissue, soft bone and bone, were calculated for meat samples and patients (fig. 4.3). PD-weighted images as well as UTE images acquired at very short echo times were chosen as observation variables resulting in a two-dimensional parameter space. The intensity distributions of tissue types showed different positions of bins with highest number of counts and varying widths. Bins with low count numbers overlapped partially. Comparing meat samples and patients, distributions were similar. However, the number of counts of bone tissue classes was significantly lower for meat samples.

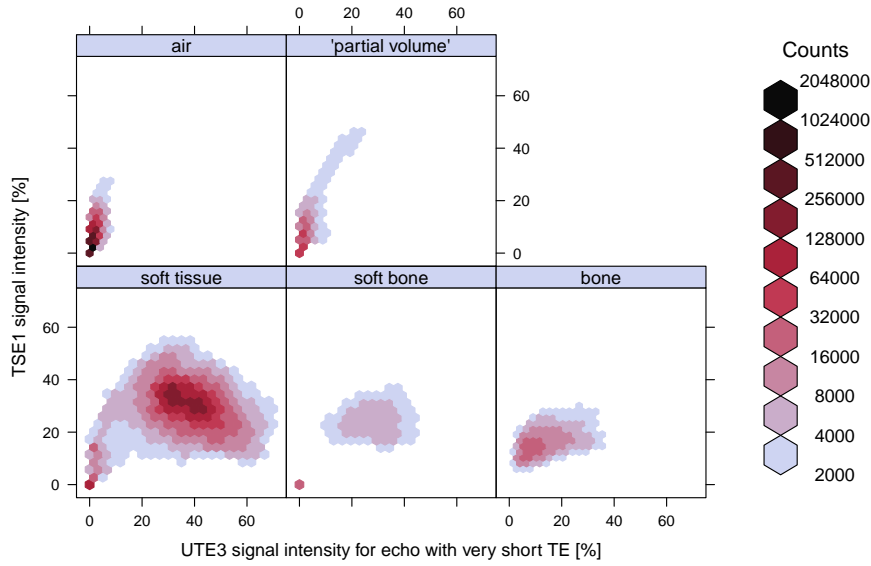
4.3 Derivation of pseudo CT

MR image series of tissue samples and patients with several contrasts were coregistered to their corresponding CT images. After this processing step, MR and CT images could be overlaid and a voxelwise correlation of images was possible. For both mangos and meat samples, only the CT images acquired at a peak voltage of 140 kVp with tin filtration were employed.

Then, the *MMclassification* package was used for deriving pCT numbers from MR images. Binary masks of samples were created utilizing PD-weighted MR images and coordinates of voxels were translated to a global coordinate system that samples were centered in the coordinate system of images. The global scaling parameter was deactivated for tissue



(a) meat samples



(b) patients

Figure 4.3: Distributions of absolute MR signal intensities of five different tissue types for meat samples and patients: the tissue types were discriminated by CT numbers of voxels: air covered the range -1024 HU to -875 HU, “partial volume” -875 HU to -375 HU, soft tissue -375 HU to 250 HU, soft bone 250 HU to 625 HU and bone all values larger than 625 HU. Bins with counts smaller than 800 for meat samples and 2000 for patients are not shown. Signal intensities of the two MRI contrasts were normalized to their maximum values and patient data was further normalized in order to account for the differences in signal intensity between patients. The bins of soft tissue and soft bone in patient plots having a high number of counts and a very low MR signal came from voxels of the patient mask and fixation. The mask and fixation was only used in CT examinations and for that reason, these voxels were measured as air in MRI.

samples. Considering patients, absolute signal intensities were additionally normalized and in the case of activated global scaling, voxel coordinates were scaled so that the expansion of binary masks between patients was equal in all three dimensions.

For classification of voxels applying the HDDA algorithm, each observation variables vector \mathbf{X}_j was composed of intensities of several MRI contrasts and additionally extracted features of one particular voxel j . Class membership of voxels was obtained from their CT numbers. Therefore the CT scale was divided into 128 sections each having a range of 32 HU and each voxel j was associated with its appropriate CT class C_j . However, CT numbers larger than 2500 HU were set to 2500 HU in order to group single voxels with such high CT numbers into one class, e. g. voxels of metal clips.

The pCT number of a voxel was then obtained by calculating the dot product of the posterior probabilities of that voxel for each of the 128 CT classes and the mean CT number of each class derived from the learning dataset. In the HDDA parameter settings the most general model $a_{kj}b_kQ_kd_k$ was used with the default threshold for dimension selection of 0.20 for tissue samples and different thresholds between 0.05 and 0.20 for patients. In addition, datasets were scaled so that each observation variable was equally weighted having a mean value of 0 and a standard deviation of 1.

Cross-validation studies were carried out individually for the three sample types mangos, meat samples and patients. In order to use independent datasets for learning and prediction, a pCT was predicted from MR images for each sample of one type using the other two samples of that type for creating the learning database. The aim of the studies was to find the best combination of contrasts and additional features for each sample type for deriving pCT numbers from MRI data.

4.3.1 Tissue samples

Cross-validation study

For mangos 479 different combinations of contrasts and additional features and for meat samples 738 combinations were tested in individual cross-validation studies as input of the observation variables vector \mathbf{X} . In order to reduce computing time only a reduced number of 32 images per sample was used. For all these combinations, mean absolute errors (MAEs) for masked voxels were calculated by a voxelwise comparison of pCT and rCT:

$$\text{MAE} = \frac{1}{n} \sum_{i=1}^n |\text{pCT}_i - \text{rCT}_i|, \quad (4.1)$$

with n as total number of voxels and i as voxel index.

For mangos the best results were achieved with a combination of the PD- and T_2 -weighted TSE sequence (TSE1, TSE2) and the UTE1 sequence each with the additional feature *dist.xyz* resulting in a seven dimensional observation variables vector \mathbf{X} (table 4.3).

contrasts	additional features	mean absolute error [HU]
mangos		
TSE1, TSE3, UTE1	<i>dist.xyz</i>	24.8
TSE1, TSE3, UTE2	<i>dist.xyz</i>	25.6
TSE1, TSE3, UTE1	<i>dist.center, dist.xyz</i>	26.0
TSE1, TSE3, MPRAGE	<i>box.mean, dist.center, dist.xyz</i>	26.3
TSE1, TSE3, UTE1, UTE2	<i>dist.xyz</i>	26.4
TSE1, TSE3, MPRAGE	<i>box.mean, dist.xyz</i>	26.5
TSE1, TSE3, UTE1	<i>dist.center</i>	26.6
TSE1, TSE3	<i>dist.xyz</i>	26.7
TSE1, TSE3, MPRAGE	none	33.6
TSE3, UTE1	<i>dist.xyz</i>	27.4
meat samples		
TSE1, UTE2	<i>box.sd, dist.center</i>	92.5
TSE1, UTE2	<i>box.sd, dist.xyz</i>	93.5
TSE1, UTE1	<i>box.sd, dist.center</i>	94.1
TSE1, UTE2	<i>box.sd, dist.center, dist.xyz</i>	95.8
TSE1, UTE2	<i>box.mean, box.sd, dist.center</i>	96.5
TSE1, UTE2	<i>box.mean, box.sd, dist.xyz</i>	96.5
TSE1, MPRAGE, UTE2	<i>box.sd, dist.center</i>	96.7
TSE1, TSE2, UTE2	<i>box.sd, dist.center</i>	97.0
TSE1, UTE1, UTE2	none	111.7
UTE1	<i>box.mean, box.sd, dist.xyz</i>	100.7
TSE1, MPRAGE	<i>box.mean, box.sd, dist.center</i>	115.7

Table 4.3: Results of cross-validation studies for mangos (upper part of table) and meat samples (lower part of table): averaged mean absolute errors of masked voxels for the eight best combinations of contrasts and additional features out of 479 combinations for mangos and 738 combinations for meat samples. In comparison, the best result without any additional feature as well as without TSE1 and UTE sequences. Results were obtained for reduced datasets of 32 images per sample.

The mean absolute errors (eq. 4.1) for such a combination for full datasets were $\text{MAE}_{\text{mango 1}} = 21.1 \text{ HU}$, $\text{MAE}_{\text{mango 2}} = 29.0 \text{ HU}$ and $\text{MAE}_{\text{mango 3}} = 30.7 \text{ HU}$. Variations of absolute errors between voxels showed standard deviations of absolute errors between 52 HU and 69 HU. The application of additional features reduced the MAE by up to 26 % on average in comparison to the best result without any additional feature.

Meat samples revealed best results with a combination of the PD-weighted TSE sequence (TSE1) and the UTE2 sequence each with additional features *box.sd* as well as *dist.center* (table 4.3). Again the observation variables vector \mathbf{X} consisted of seven dimensions. The mean absolute errors (eq. 4.1) for that combination for full datasets were $\text{MAE}_{\text{meat sample 1}} = 81.0 \text{ HU}$, $\text{MAE}_{\text{meat sample 2}} = 95.2 \text{ HU}$ and $\text{MAE}_{\text{meat sample 3}} = 90.1 \text{ HU}$. Standard deviations of absolute errors were between 130 HU and 152 HU. Employing additional features resulted in a reduction of the MAE up to 17 % on average, whereas the usage of an UTE sequence improved the results by up to 20 % on average.

A typical dataset of around 200 images for learning and 100 images for prediction needed around 5 - 6 min of computing time for both, the learning step and the prediction step (running on an Intel Core i5 processor with 4 cores and assuming cropped images that were represented by matrices of around 45000 voxels).

For each sample the r CT (fig. 4.4 c, d) was subtracted from the p CT of the best combination of contrasts and additional features (fig. 4.4 a, b) yielding a difference map (fig. 4.4 e, f).

For mangos p CT values of soft tissue and the pit were in good agreement with r CT numbers. Largest errors appeared at borders between soft tissue and air, at air cavities around the pit and at the paper bowls that were used for mounting the mangos at CT image acquisitions. Considering all three mangos, largest errors of single voxels were in the range of 859 HU and 1054 HU.

Results of tissue samples were similar to mangos. Again soft tissue values showed low errors and voxels at transitions between different tissue classes revealed the largest errors. In addition, bone classes also exhibited high deviations. Having large variations of errors, some parts of bones were overestimated, whereas most parts were underestimated. Maximum errors of single voxels were between 1430 HU and 1901 HU.

Mean errors per class

Additionally, the mean errors of p CT per class ME_{cl} were calculated (fig. 4.5 a, c):

$$ME_{cl} = \frac{1}{n_{cl}} \sum_{i=1}^{n_{cl}} p\ CT_{i,cl} - r\ CT_{i,cl}, \quad (4.2)$$

with n_{cl} as number of voxels per class, cl as class index and i as voxel index. In contrast to the MAE, the mean error (ME) represents an average error of a large number of voxels and positive and negative deviations may cancel out.

Mean errors of p CT classes of mangos were in the range from -159 HU to 132 HU. The air class was systematically overestimated, whereas soft tissue showed a slightly underestimation but was in general in good agreement. The “partial volume” class revealed large variations of mean errors between mangos.

For meat samples mean errors of p CT classes covered a much larger range from -791 HU to 98 HU. Air, “partial volume” and soft tissue classes showed a similar progression than for mangos. But in contrast to mangos, for which the maximum CT number was at 237 HU, the range of CT scale for meat samples was up to 1145 HU. These high CT numbers representing bones were strongly underestimated in p CT images.

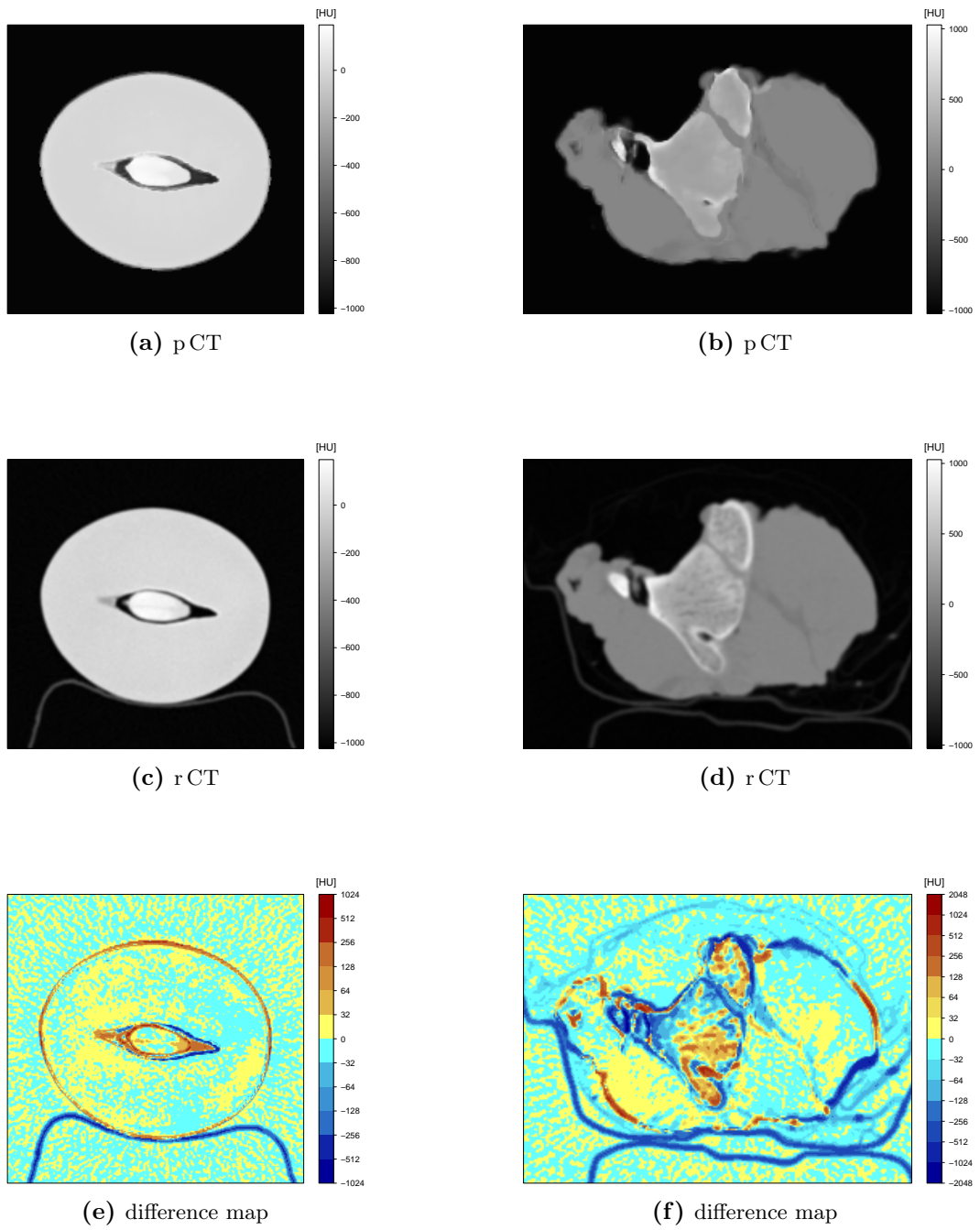


Figure 4.4: Examples of a transversal slice of mango 1 (left column) and meat sample 2 (right column): (a, b) p CT of the best combination of contrasts and additional features. The samples were placed in a bowl made out of paper that gave no signal in MRI resulting in a wrong classification of these voxels as air; (c, d) r CT; (e, f) difference map from data of (a, c) or (b, d). In the logarithmic color scale, red pixels represent an overestimation and blue pixels an underestimation of the r CT number.

Contributions to the sum of absolute mean errors

Furthermore, for each class the contribution to the sum of absolute mean errors CSAME_{cl} was computed (fig. 4.5 b, d):

$$\text{CSAME}_{cl} = \frac{|\text{ME}_{cl}| n_{cl}}{\sum_{cl=1}^K |\text{ME}_{cl}| n_{cl}} \times 100, \quad (4.3)$$

with ME_{cl} as mean error per class, n_{cl} as number of voxels per class, K as total number of classes and cl as class index.

For mangos, variations in the progression of contribution curves between samples were small. Soft tissue classes around 0 HU contributed most to the sum of absolute mean errors having a magnitude of 22 - 38 % and a second small peak appeared at the air class with fractions of around 3 - 7 %. The contributions of all other classes were below 3 %. In contrast, meat samples showed a more even distribution. Highest proportions could again be found at soft tissue classes around 0 HU and the air class both having small peaks between 4 - 6 %. Contributions of all other classes were below 3 %.

4.3.2 Patients

Cross-validation study

A cross-validation study similar to tissue samples was carried out for patient data. In addition to combinations of MR image series with three different contrasts and additional features, the HDDA threshold parameter was varied between 0.05, 0.10 and 0.20 and the global scaling was tested both activated and deactivated.

Altogether 582 combinations were analyzed using full datasets of the three patients. A combination of the PD-weighted (TSE1) and the UTE3 sequence with all additional features *box.mean*, *box.sd*, *dist.center*, *dist.xyz* and a HDDA threshold of 0.10, but without global scaling, showed the best results (table 4.4 and fig. 4.6, 4.7). Mean absolute errors (eq. 4.1) were $\text{MAE}_{\text{patient 1}} = 140.7 \text{ HU}$, $\text{MAE}_{\text{patient 2}} = 141.4 \text{ HU}$ and $\text{MAE}_{\text{patient 3}} = 165.2 \text{ HU}$ for patients 1-3, respectively. Standard deviations of absolute errors were between 284 HU and 321 HU. Extraction of additional features decreased the MAE by up to 27 % on average and the UTE sequence led to a reduction of the MAE up to 21 % on average.

The difference map revealed good accordance of soft tissue pCT numbers with rCT (fig. 4.6 e, f and fig. 4.7 c). Again large errors appeared at tissue transitions of air to soft tissue, soft tissue to bones and air to bones. Largest errors of single voxels up to 3261 - 4047 HU were found at air cavities and bones as well as at metal clips at the skull of one patient.

Mean errors per class

Mean errors of pCT per class ME_{cl} (eq. 4.2) showed a comparable systematical progression for all three patients and covered a huge range from -3655 HU to 1094 HU (fig. 4.5 e).

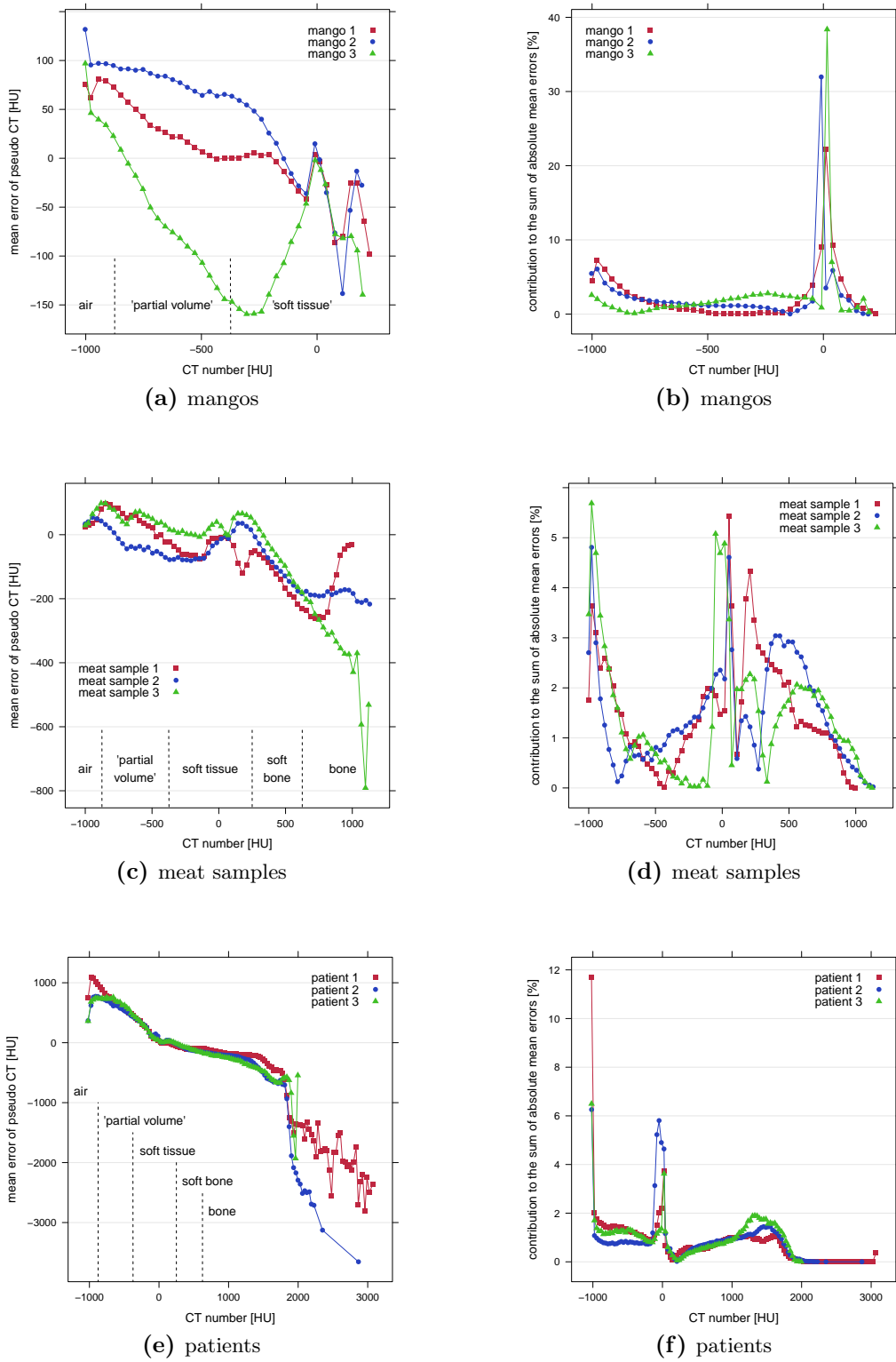


Figure 4.5: Mean errors of pCT per class ME_{cl} (a, c, e) and contributions of CT classes to the sum of absolute mean errors $CSAME_{cl}$ (b, d, f) for mangos (top row), meat samples (center row) and patients (bottom row).

The air and “partial volume” class revealed a strong overestimation, soft tissue was in good agreement with rCT values and soft bones and bones were strongly underestimated.

Contributions to the sum of absolute mean errors

Moreover the contribution of each class to the sum of absolute mean errors $CSAME_d$ (eq. 4.3) was calculated (fig. 4.5 f). Progression of curves was quite similar for the three patients. The air class contributed most with a magnitude of 6 - 12 % followed by soft tissue around 0 HU with a fraction of 4 - 6 %. All other classes showed proportions below 2 % and classes with CT numbers higher than 2000 HU had almost no contributions.

contrasts	additional features	global scaling	HDDA threshold	mean absolute error [HU]
TSE1, UTE3	<i>box.mean, box.sd, dist.center, dist.xyz</i>	off	0.10	149.0
TSE1, UTE3	<i>box.mean, box.sd, dist.center, dist.xyz</i>	on	0.10	152.0
TSE1, UTE3	<i>box.mean, box.sd, dist.xyz</i>	off	0.10	153.6
TSE1, UTE3	<i>box.mean, box.sd, dist.xyz</i>	on	0.10	155.6
TSE1, UTE3	<i>box.mean, box.sd, dist.xyz</i>	off	0.05	155.9
TSE1, UTE3	<i>box.mean, box.sd, dist.center, dist.xyz</i>	on	0.05	156.2
TSE1, UTE3	<i>box.mean, box.sd, dist.center, dist.xyz</i>	off	0.20	156.4
TSE1, UTE3	<i>box.mean, box.sd, dist.center, dist.xyz</i>	on	0.20	157.2
TSE1, UTE3	none	on	0.05	205.5
UTE3	<i>box.mean, box.sd, dist.center, dist.xyz</i>	off	0.20	193.8
TSE1	<i>box.mean, box.sd, dist.xyz</i>	off	0.05	189.9

Table 4.4: Results of cross-validation study for patients: averaged mean absolute errors of masked voxels for the eight best combinations of contrasts, additional features and classification parameters out of 582 combinations. In comparison, the best result without any additional feature as well as without TSE1 and UTE3 sequences.

4.4 Ion radiotherapy treatment plan simulation

4.4.1 Translation of CT to WEPL

Pseudo CT as well as rCT numbers were translated to WEPL values using a HLUT. As X-ray spectra have an influence on CT numbers, different HLUTs were applied for the translation of images of tissue samples and patients. A clinical HLUT for tissue samples did not exist as images were acquired at an X-ray spectra voltage of 140 kVp with tin filtration. Therefore, an empirical HLUT derived from measurements of Gammex tissue equivalent materials, performed in Tremmel (2012), was used (fig. 4.8 a). As patient data examinations were carried out using a standard ion radiotherapy protocol, the clinical stoichiometric HLUT used at HIT could be employed for translation (fig. 4.8 b).

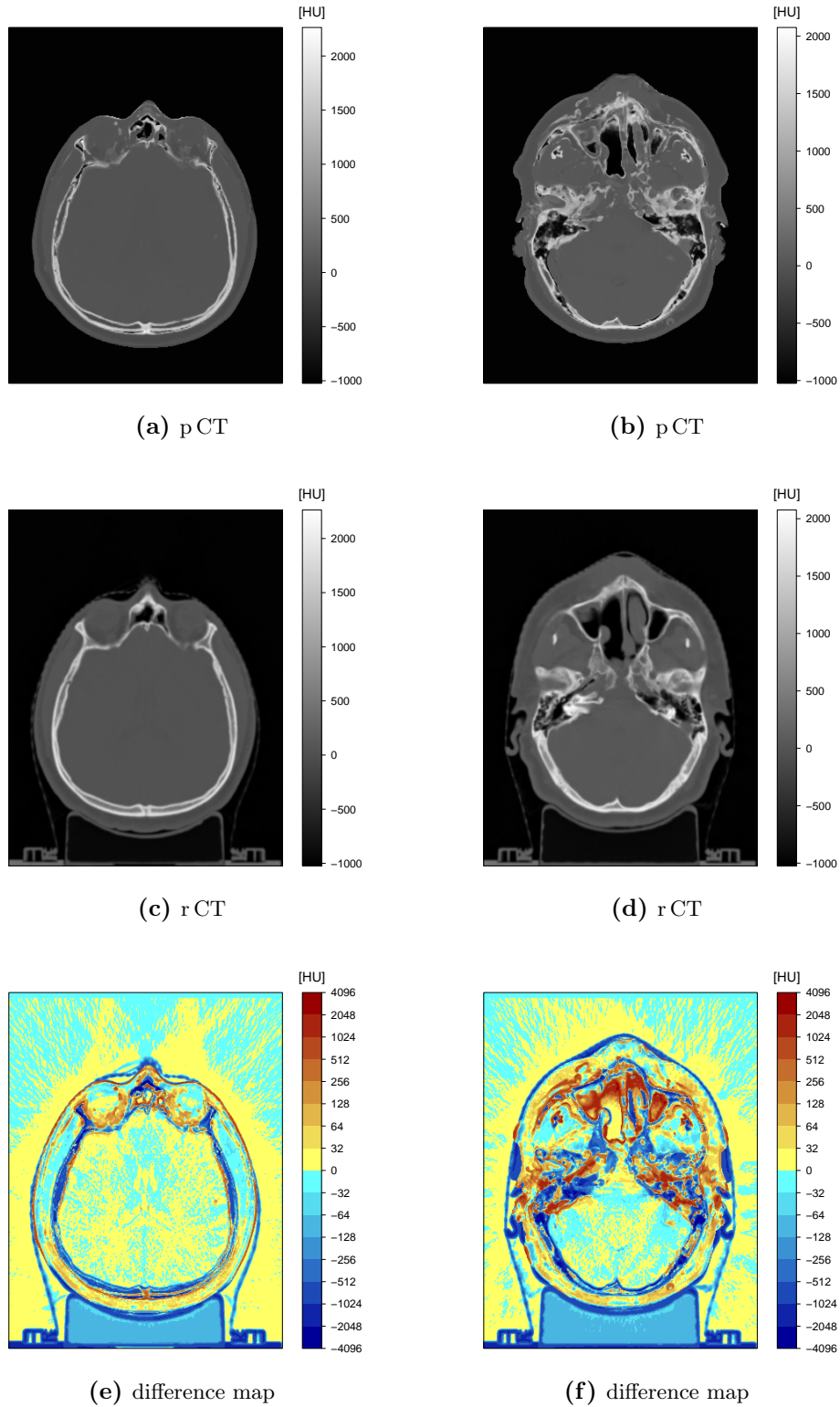
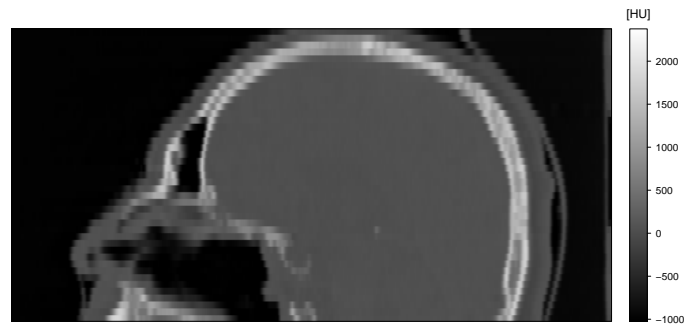


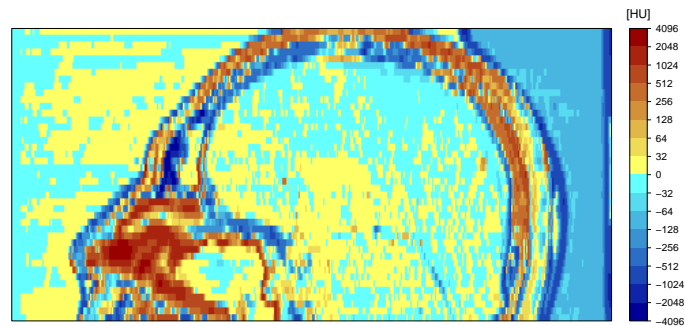
Figure 4.6: Examples of transversal slices of the head region of patient 2: (a, b) p CT using the best combination of contrasts and additional features; (c, d) r CT; (e, f) difference map from data of (a, c) or (b, d). In the logarithmic color scale, red pixels represent an overestimation and blue pixels an underestimation of the r CT number.



(a) p CT



(b) r CT



(c) difference map

Figure 4.7: Example of a sagittal slice of the head region of patient 2: (a, b) p CT using the best combination of contrasts and additional features; (c, d) r CT; (e, f) difference map from data of (a, c) or (b, d). In the logarithmic color scale, red pixels represent an overestimation and blue pixels an underestimation of the r CT number.

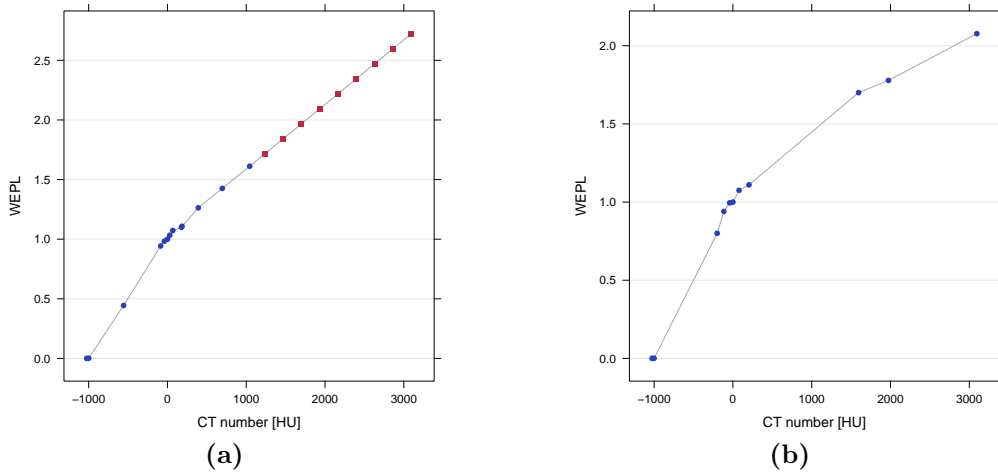


Figure 4.8: HLUTs used for translation of CT to WEPL: (a) empirical HLUT for 140 kVp CT used for tissue samples. Blue dots represent measured values of Gammex tissue equivalent materials and red squares were extrapolated; (b) clinical stoichiometric HLUT from HIT for 120 kVp CT patient data.

4.4.2 Estimation of mean deviation of WET

Employing the translated pseudo WEPL values and their errors derived from mean errors of pCT, an estimate of the mean deviation of water equivalent thickness (WET) for the five tissue types air, “partial volume”, soft tissue, soft bone and bone was calculated:

$$\Delta \text{WET}_{\text{tissue}, d} = \Delta \text{WEPL}_{\text{tissue}} \times d, \quad (4.4)$$

with d as tissue thickness. Variations of ΔWET were evaluated by computing the standard error per tissue type for a beam passing two different thicknesses assuming an irradiation in a lateral direction where the image resolution was 0.5 mm for meat samples and 0.6 mm for patients.

Similar to the calculation of mean errors of pCT per class, for both meat samples and patients the two bone classes exhibited a strong underestimation and air as well as “partial volume” voxels were overestimated. The soft tissue class was in good agreement with reference values (table 4.5). Estimated mean deviations of WET for patients were larger than for meat samples.

4.4.3 Results of ion treatment plan simulation

In VIRTUOS, ion radiotherapy treatment plans were created. A planning target volume (PTV) was placed in both pCT and rCT volumes of all meat samples and patients. A position considered to be the most challenging was chosen for meat samples where the ion beam had to pass bony structures (fig. 4.9 a). For patients hypothetical PTVs were defined at a site inside the brain (fig. 4.9 b).

tissue	mean error of p CT [HU]	$\Delta\text{WET}_{1\text{ cm}}$ [mm]	$\Delta\text{WET}_{10\text{ cm}}$ [mm]
meat samples			
air	43.3	0.4 ± 0.3	3.6 ± 0.9
“partial volume”	28.6	0.3 ± 0.7	2.9 ± 2.1
soft tissue	-1.4	-0.02 ± 0.3	-0.2 ± 0.9
soft bone	-63.2	-0.4 ± 0.3	-3.7 ± 0.9
bone	-223.1	-1.2 ± 0.4	-11.9 ± 1.1
patients			
air	581.9	2.33 ± 1.2	23.3 ± 3.7
“partial volume”	645.3	6.57 ± 1.3	65.8 ± 4.1
soft tissue	28.5	0.26 ± 0.3	2.6 ± 1.0
soft bone	-94.6	-0.56 ± 0.5	-5.6 ± 1.6
bone	-278.6	-1.50 ± 0.6	-15.0 ± 2.0

Table 4.5: Mean errors of p CT and estimated mean deviations of WET with corresponding standard errors of meat samples and patients for different tissue types considering an irradiation at 1 cm and 10 cm depth.

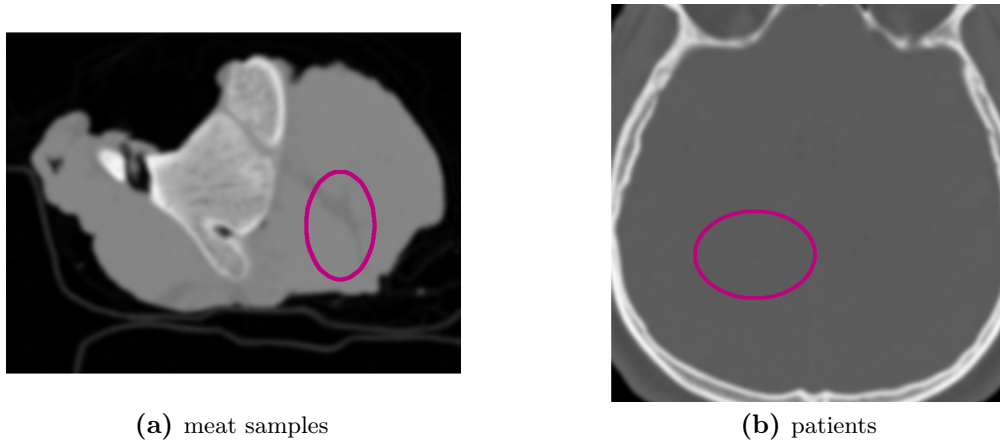


Figure 4.9: Examples of PTV definitions.

Inverse optimization of irradiation fields and the calculation of dose distributions was carried out with TRiP98. A raster-scanning pencil beam model with a full width at half maximum of 5 mm passing a 3 mm ripple filter was assumed for protons and carbon ions. Prescribed physical doses were 3 Gy for protons and 1 Gy for carbon ions.

Proton and carbon field optimizations were run using both MRI-based p CT images and r CT images for meat samples and for patients. Fields optimized on the basis of p CTs were recalculated on r CTs that were considered to be the gold standard (fig. 4.10 a, b and fig. 4.11 a, b). Resulting dose distributions were compared with plans optimized and calculated on r CT images (fig. 4.10 c - f and fig. 4.11 c - f). In addition, dose-volume histograms (DVHs) were calculated for both optimizations (fig. 4.12). In general, dose coverage of PTVs was better for r CT optimizations than for MRI-based p CT optimizations (table 4.6 and

fig. 4.12, 4.13). For meat samples especially distal regions of PTVs showed an underdosage in p CT optimizations. Mean doses of PTVs D_{mean} of r CT optimizations were 0.8 - 3.1 % higher than for p CT optimizations and volumes of PTVs with a dose less than 90 % of prescribed dose $V_{D<90\%}$ were 0 - 8.3 % smaller (table 4.6, upper part). Comparing results of patients, dose differences between p CT and r CT optimizations were less pronounced than for meat samples. Here, mean doses of PTVs D_{mean} of r CT optimizations were only 0.4 - 2.0 % higher compared to p CT and volumes of PTVs with a dose less than 90 % of prescribed dose $V_{D<90\%}$ were 0 - 3.1 % smaller (table 4.6, lower part).

sample type	beam modality	p CT plans		r CT plans	
		D_{mean} [%]	$V_{D<90\%}$ [%]	D_{mean} [%]	$V_{D<90\%}$ [%]
meat sample 1	carbon left	96.5	8.4	99.0	0.7
	proton left	96.2	8.3	99.3	0.0
meat sample 2	carbon left	96.7	4.6	99.0	0.1
	proton left	96.2	6.0	98.9	0.4
meat sample 3	carbon left	97.4	3.4	98.8	0.3
	proton left	97.3	2.4	98.8	0.2
	carbon right	98.2	0.3	99.0	0.1
	proton right	98.0	0.3	98.9	0.3
patient 1	carbon left	98.4	0.1	98.9	0.3
	proton left	97.9	0.2	99.0	0.2
	carbon right	98.2	0.1	98.8	0.1
	proton right	98.1	0.0	99.2	0.1
	carbon left+right	98.4	0.0	98.8	0.0
	proton left+right	98.1	0.0	99.1	0.2
	photon star7	97.0	1.5	96.9	1.7
patient 2	carbon left	97.8	1.9	98.9	0.2
	proton left	97.6	1.7	99.1	0.0
	carbon right	97.2	2.8	99.0	0.2
	proton right	97.1	2.6	99.1	0.0
	carbon left+right	97.5	3.4	98.8	0.3
	proton left+right	97.3	3.0	99.1	0.0
	photon star7	97.1	1.1	97.0	1.0
patient 3	carbon left	97.8	2.5	98.5	0.6
	proton left	97.6	2.0	98.9	0.1
	carbon right	97.9	0.8	98.8	0.1
	proton right	97.7	0.9	99.1	0.0
	carbon left+right	98.0	1.1	98.8	0.1
	proton left+right	97.7	0.9	99.1	0.0
	photon star7	96.9	1.6	97.1	1.5

Table 4.6: Dose statistics parameters of treatment plan simulations of meat samples and patients for carbon ions, protons and photons using both p CT and r CT. An interpretation and direct comparison of results of photon plans with ion plans is difficult as photon fields were not inversely optimized, but geometrically shaped in a forward-optimization process and then calculated on both p CT and r CT.

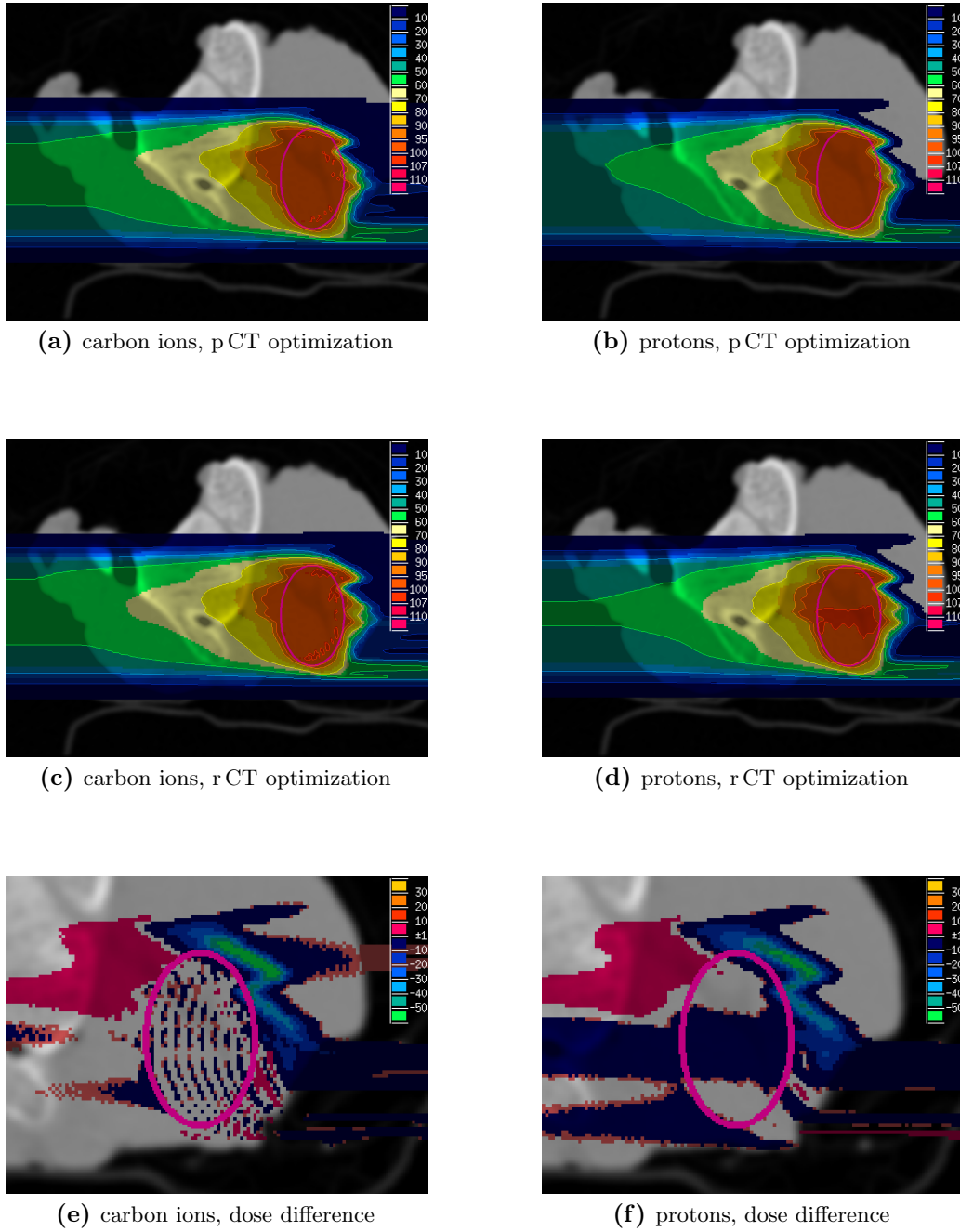
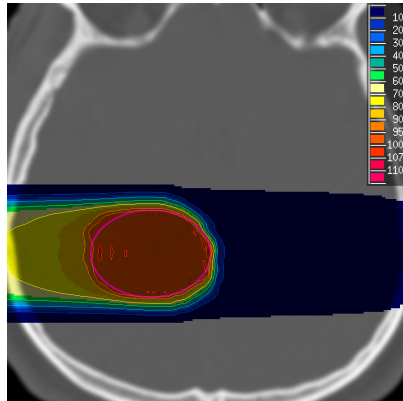
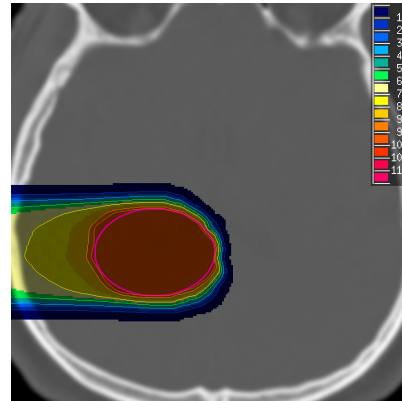


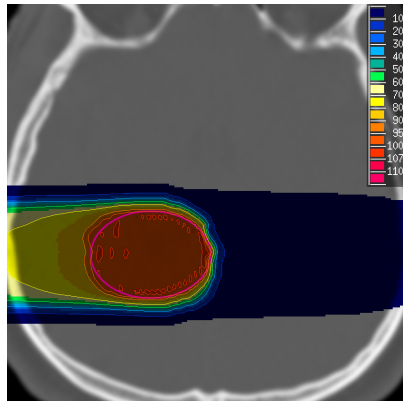
Figure 4.10: Examples of treatment plan simulations of meat sample 2 with a PTV size of $17 \times 26 \times 16 \text{ mm}^3$ for carbon ions (left column) and protons (right column): (a, b) optimized on p CT and recalculated on r CT; (c, d) optimized and calculated on r CT; (e, f) dose difference of (a, c) or (b, d). The unit of color scale is percent of the prescribed physical dose.



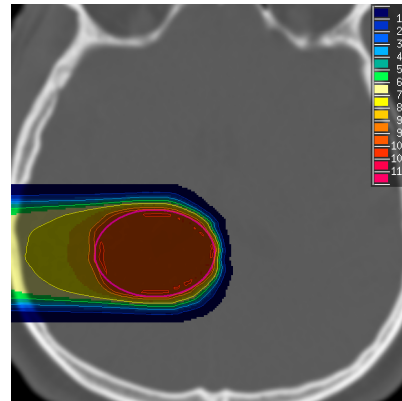
(a) carbon ions, p CT optimization



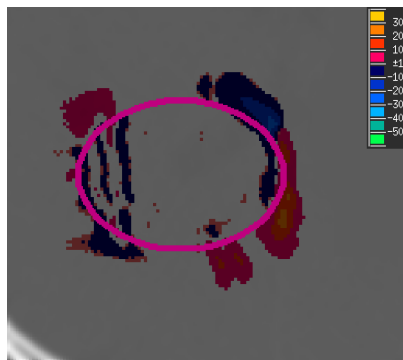
(b) protons, p CT optimization



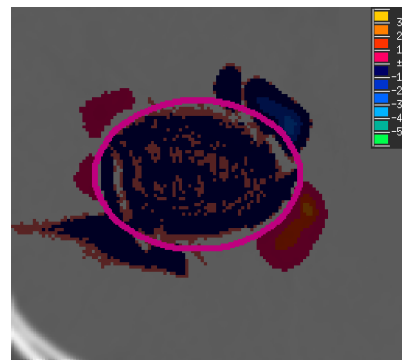
(c) carbon ions, r CT optimization



(d) protons, r CT optimization

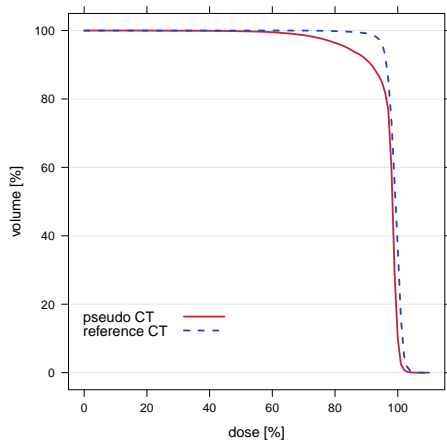


(e) carbon ions, dose difference

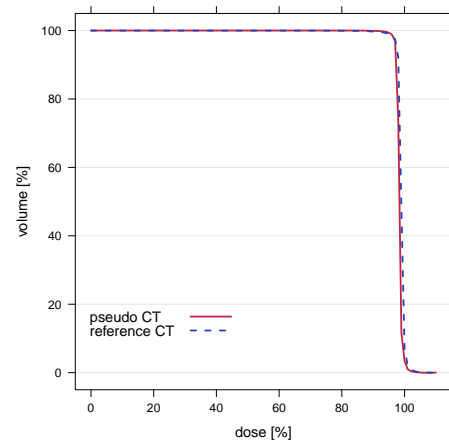


(f) protons, dose difference

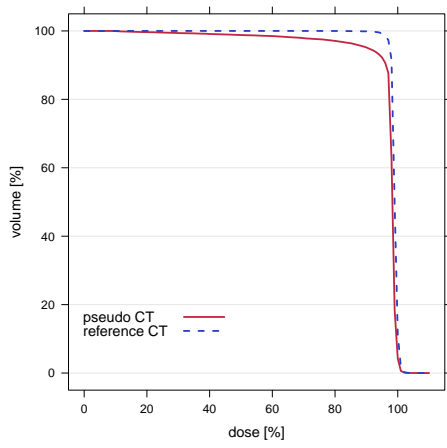
Figure 4.11: Examples of treatment plan simulations of patient 2 with a PTV size of $40 \times 29 \times 30 \text{ mm}^3$ for carbon ions (left column) and protons (right column): (a, b) optimized on p CT and recalculated on r CT; (c, d) optimized and calculated on r CT; (e, f) dose difference of (a, c) or (b, d). The unit of color scale is percent of the prescribed physical dose.



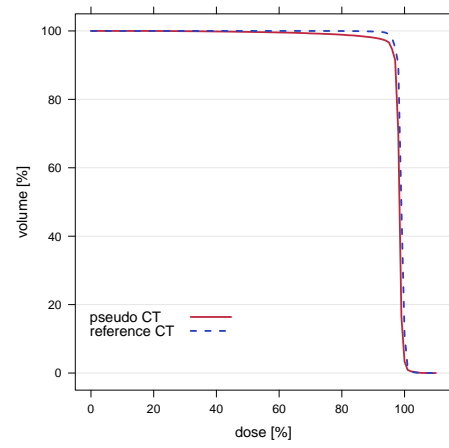
(a) meat sample 1: carbon left



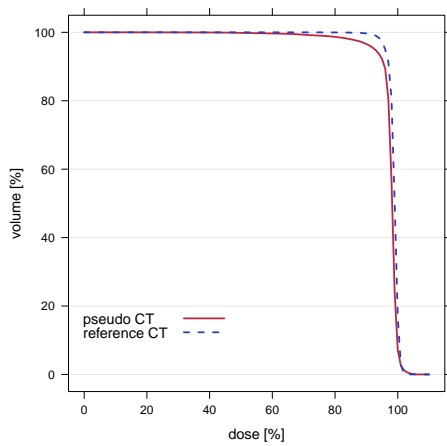
(b) patient 1: carbon left



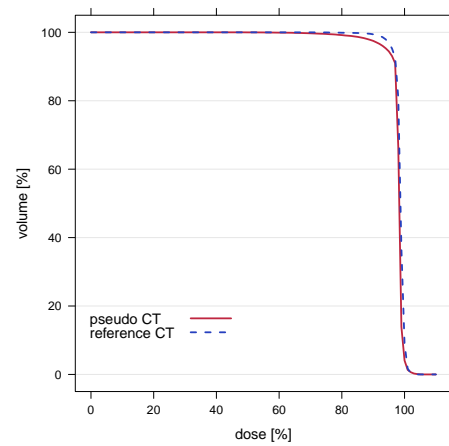
(c) meat sample 2: carbon left



(d) patient 2: carbon left

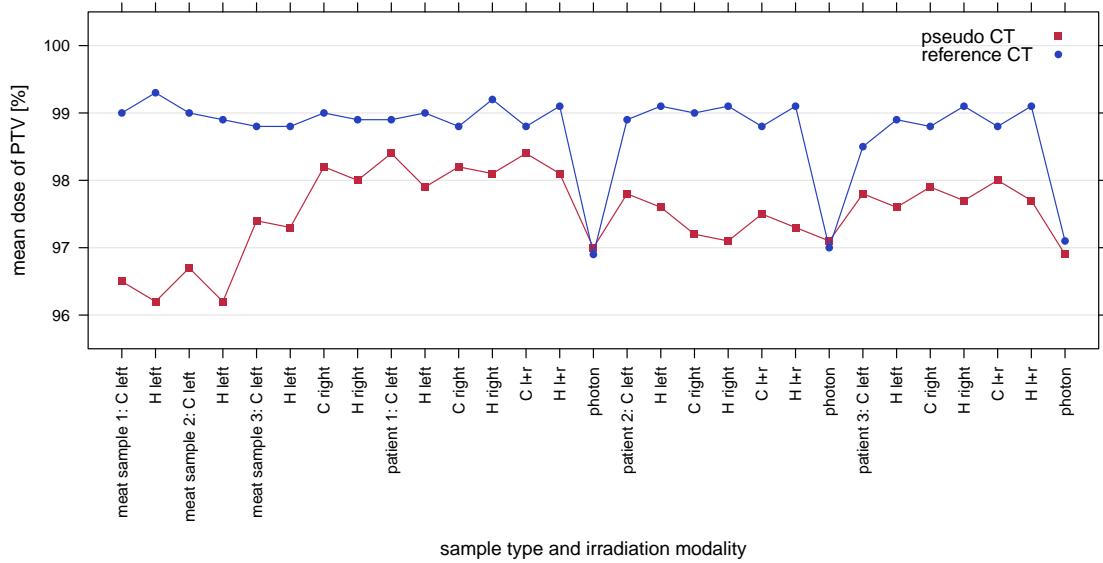


(e) meat sample 3: carbon left

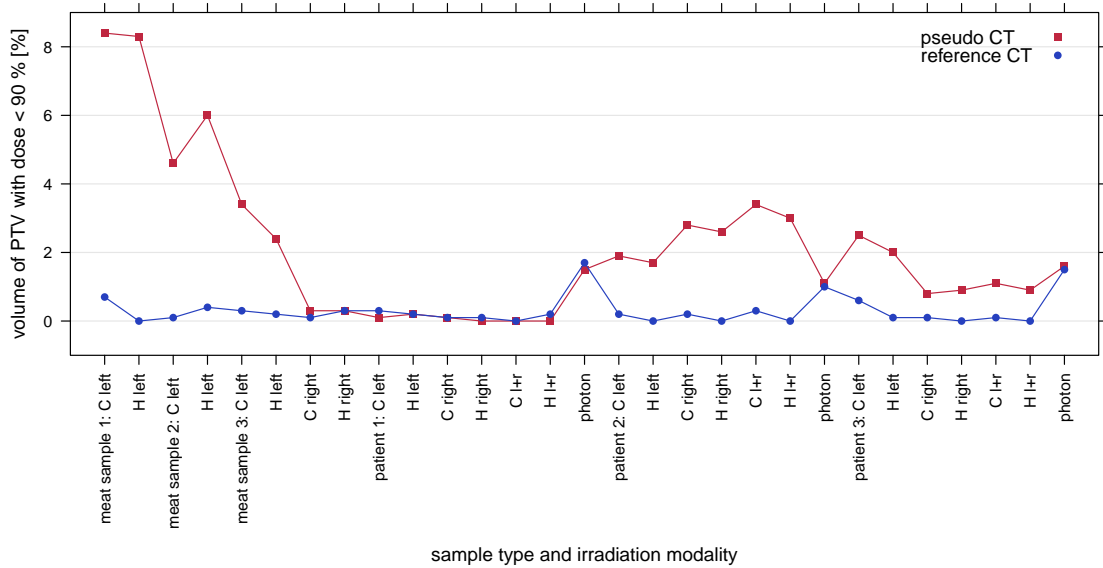


(f) patient 3: carbon left

Figure 4.12: DVHs of treatment plan simulations of meat samples (left column) and patients (right column) for carbon ions. Red curves represent plans optimized on p CT and recalculated on r CT, whereas blue curves illustrate plans optimized and calculated on r CT.



(a) mean dose of PTV



(b) volume of PTV with dose less than 90 %

Figure 4.13: Dose statistics parameters of treatment plan simulations of meat samples and patients for carbon ions, protons and photons using both p CT and r CT. An interpretation and direct comparison of results of photon plans with ion plans is difficult as photon fields were not inversely optimized, but geometrically shaped in a forward-optimization process and then calculated on both p CT and r CT.

4.5 Photon radiotherapy treatment plan simulation

Photon treatment plans were generated with VIRTUOS for both pCT and rCT images of patients. The same PTVs were used as for ion radiotherapy plans. A *star7* photon field configuration was chosen, i. e. seven fields equally distributed on a circular arc lying in one plane. In contrast to the simulation of ion treatment plans, conventional photon fields were not inversely optimized. However, fields were geometrically shaped in a forward-optimization process allowing irregular field contours and collimator orientations. Dose distributions within pCT and rCT volumes were then calculated with the fast pencil kernel algorithm *PDC++* implemented in VIRTUOS (fig. 4.14 a, b).

Differences in dose distributions were very small and only single voxels of PTVs showed deviations in the range of 1 - 10 % (table 4.6 and fig. 4.13, 4.14 c). Mean doses of PTVs D_{mean} and volumes of PTVs with a dose less than 90 % of prescribed dose $V_{D<90\%}$ differed by maximal 0.2 %. Furthermore differences of DVH curves of both simulations showed that volumes of PTVs receiving 98 % of prescribed dose were equivalent, but small deviations of volume in the range of 4 % appeared at 99 - 100 % of dose (fig. 4.14 d).

4.6 Ion radiotherapy treatment plan adaptation

Simulation of target volume shift

In order to investigate the potential of MRI for treatment plan adaptation, i. e. to align plans with interfractional anatomical changes, the following experiment was carried out: a target volume shift between the rCT examination and subsequent fractions was simulated and a treatment plan optimized on the basis of the original rCT without plan adaptation was compared to a plan that was adapted to the target shift using MRI data.

For the experiment the irradiated PTV of meat sample 2 was shifted 2.25 mm in x - and 1.25 mm in y -direction (fig. 4.15 a). For all three patients a target volume movement was simulated by a PTV shift of 1.60 mm in both x - and y -direction (fig. 4.15 b). For decreasing errors introduced by the derivation of pCT numbers, a so-called corrected CT (cCT) was created for meat sample 2 and all three patients. This hybrid approach was based on information from both MRI-based pCT as well as CT-based rCT. As bone tissue classes had largest deviations in pCT images and anatomical changes in bony structures are uncommon, the cCT consisted of the original rCT, in which a volume surrounding the PTV and containing solely soft tissue was replaced by pCT values (fig. 4.15 c, d).

Results of ion treatment plan adaptation

Optimizations of treatment plans created in VIRTUOS and adapted to the target shift were performed on the basis of cCT images with TRiP98 in a similar way as for pCT and rCT images. Proton and carbon field optimizations were run for plans adapted to the

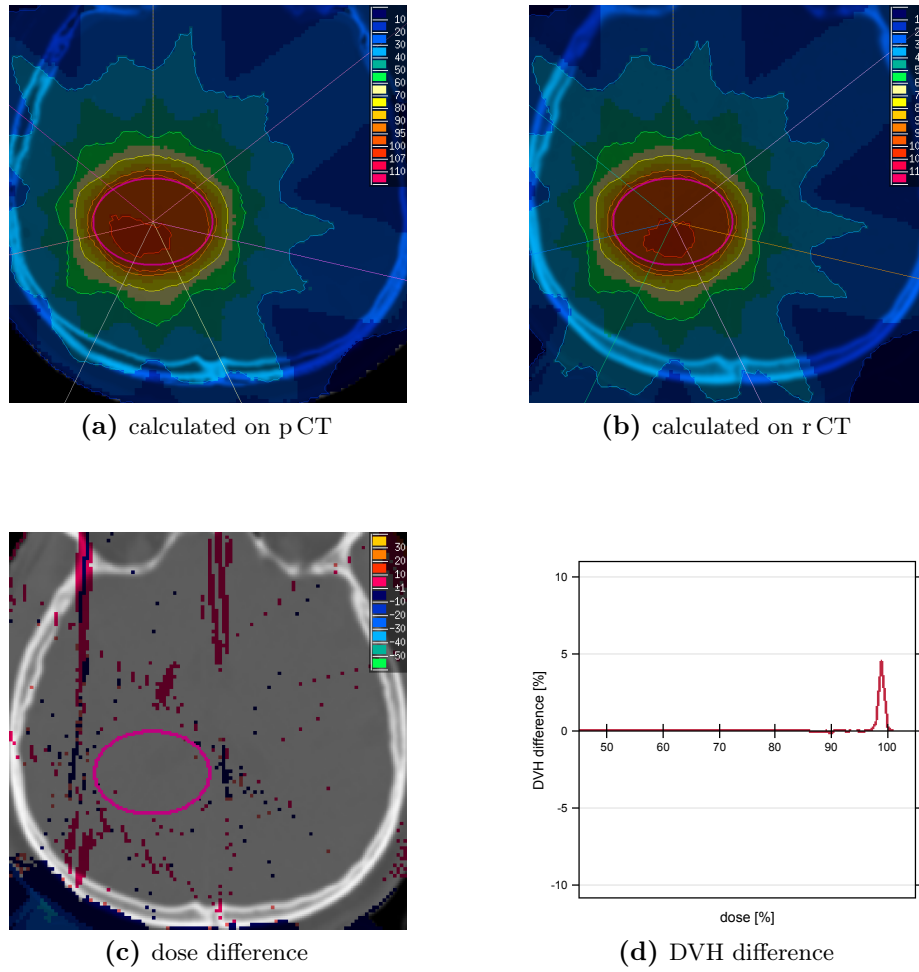


Figure 4.14: Example of photon treatment plan simulation of patient 2 with a PTV size of $40 \times 29 \times 30 \text{ mm}^3$: (a) calculated on p CT; (b) calculated on r CT; (c) dose difference of (a, b); (d) DVH difference of p CT and r CT simulation. The unit of color scale is percent of the prescribed physical dose.

shifted PTVs using c CT images. Dose distributions of the resulting fields were recalculated on r CT images taking the shifted PTVs into account (fig. 4.16 a, b). The results were compared to fields optimized on the basis of r CT before PTV shift and calculated on r CT after PTV shift without plan adaptation (fig. 4.16 c, d).

The c CT optimizations of adapted plans showed for meat sample 2 as well as for the three patients a much better dose coverage of the shifted target volume compared to the r CT optimized plans without plan adaptation. These results were confirmed by DVHs calculated for both types of plans (fig. 4.17). Mean doses of PTVs D_{mean} of adapted c CT plans were 0.1 - 2.3 % higher than for r CT plans without plan adaptation and volumes of PTVs with a dose less than 90 % of prescribed dose $V_{D < 90 \%}$ were 5.0 - 10.0 % smaller (table 4.7).

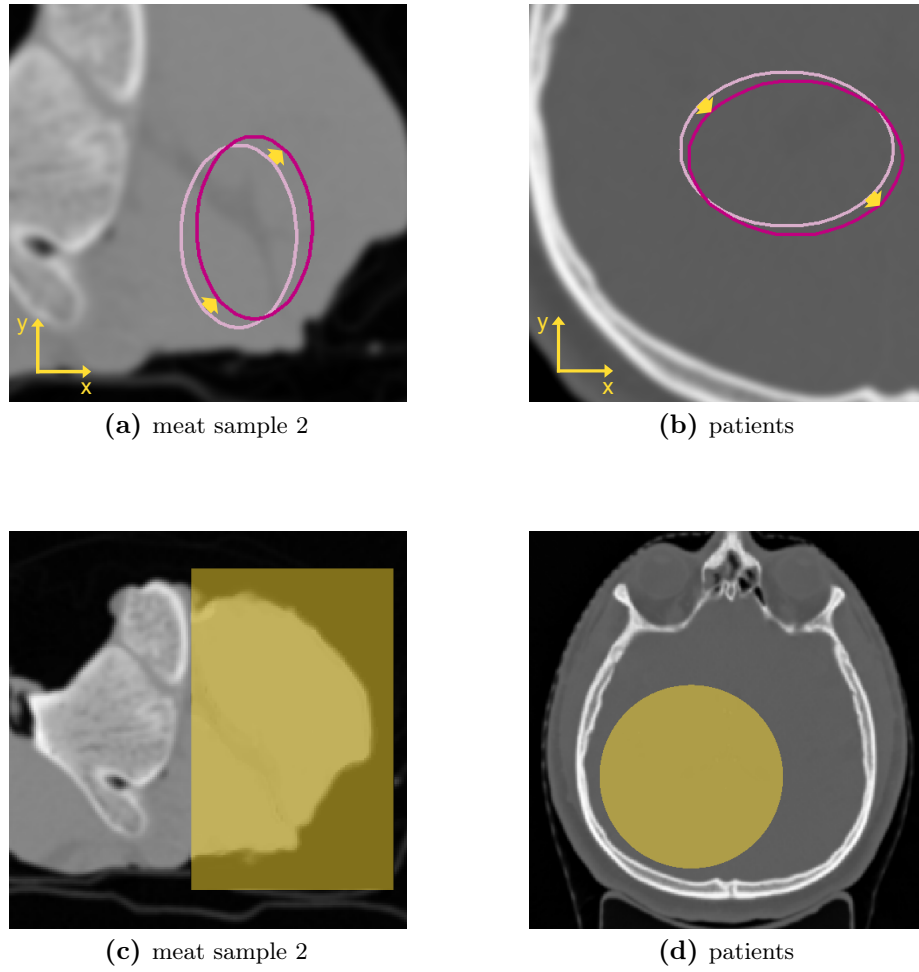
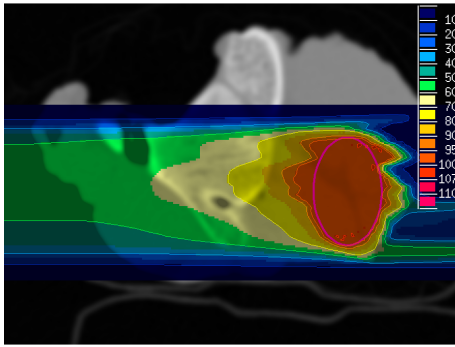


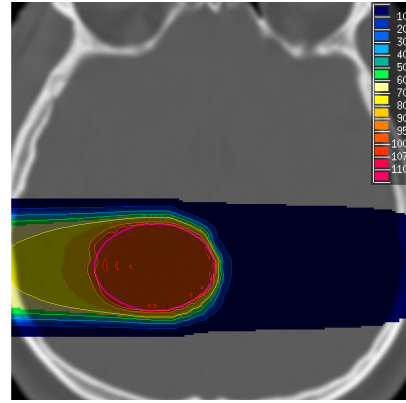
Figure 4.15: Simulated target volume shifts (a, b) and volumes of rCTs replaced by pCT values for creating the cCT (c, d).

sample type	beam modality	adapted c CT plans		non-adapted r CT plans	
		D_{mean} [%]	$V_{D<90\%}$ [%]	D_{mean} [%]	$V_{D<90\%}$ [%]
meat sample 2	carbon left	98.4	0.1	96.5	8.1
	proton left	98.2	0.0	96.0	10.0
patient 1	carbon left	98.4	0.1	96.4	7.8
	proton left	97.9	0.2	96.6	7.9
patient 2	carbon left	98.3	0.1	97.5	5.9
	proton left	98.1	0.0	98.0	5.0
patient 3	carbon left	98.2	0.0	95.9	9.2
	proton left	98.0	0.0	96.8	7.9

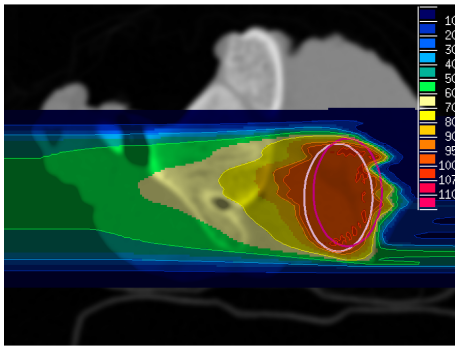
Table 4.7: Dose statistics parameters of treatment plan adaptation of meat sample 2 and all three patients for carbon ions: plans were adapted and optimized on cCT as well as optimized on rCT without plan adaptation. For comparison, all plans were recalculated on rCTs after PTV shift.



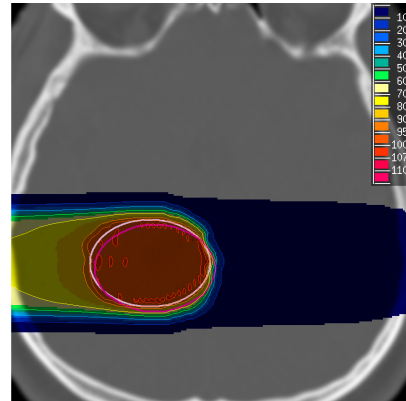
(a) c CT optimization of adapted plan



(b) c CT optimization of adapted plan

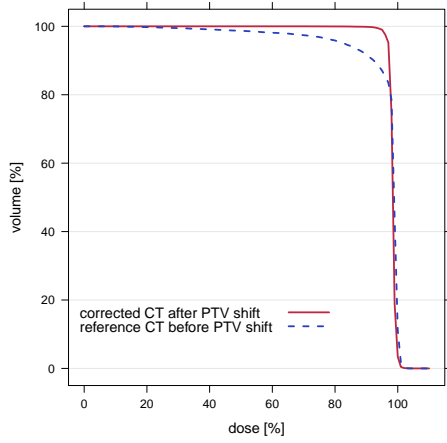


(c) r CT optimization of non-adapted plan

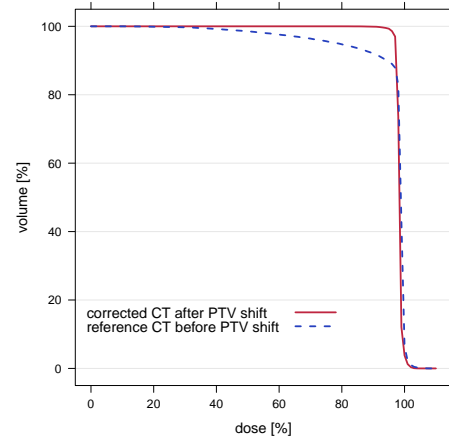


(d) r CT optimization of non-adapted plan

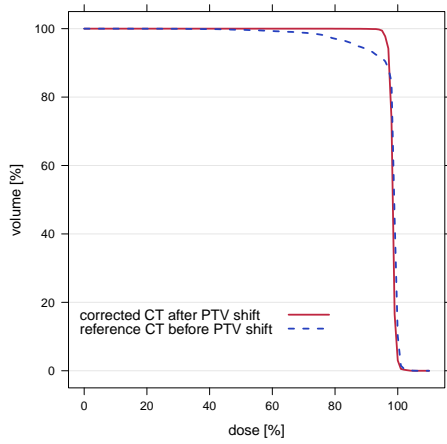
Figure 4.16: Examples of treatment plan adaptation of meat sample 2 (left column) and patient 2 (right column) for carbon ions: (a, b) adapted plans optimized on c CT and recalculated on r CT after PTV shift; (c, d) non-adapted plans optimized on r CT before PTV shift and recalculated on r CT after PTV shift. The unit of color scale is percent of the prescribed physical dose.



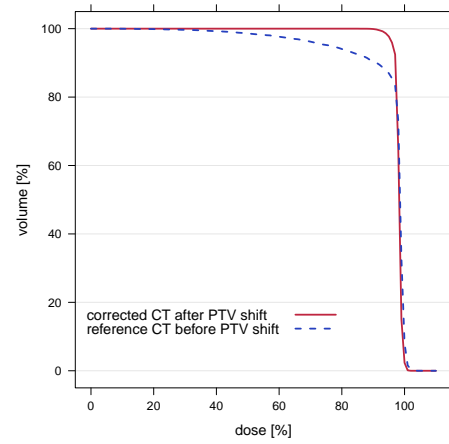
(a) meat sample 2: carbon left



(b) patient 1: carbon left



(c) patient 2: carbon left



(d) patient 3: carbon left

Figure 4.17: DVHs of treatment plan adaptation of meat sample 2 (a) and all three patients (b - d) for carbon ions: plans were optimized on c CTs after PTV shift (red curves) and on r CTs before PTV shift without plan adaptation (blue curves). For comparison, all plans were recalculated on r CTs after PTV shift.

5 | Discussion

5.1 MR image acquisition

Measurement and distribution of absolute MR signal intensities

MRI measurements of tissue samples and patients showed that a quantitative evaluation of signal intensities is more difficult than in CT imaging. Whereas the CT intensity of a voxel mainly depends on the linear attenuation coefficient μ , the MR signal is influenced by several quantities, in particular the density of water and fat protons as well as characteristic relaxation times of tissue T_1 , T_2 and T_2^* . Thus several parameters in MR sequence protocols have an effect on signals of voxels and in contrast to CT, signal intensities of one tissue type can have large variations dependent on the applied sequence and its parameters. Although absolute measurements of physical relaxation times are possible, they are not reasonable for patient examinations due to very long image acquisition times. In clinical practice, weighted MR images are usually acquired as for diagnosis the contrast between two tissue types is sufficient for interpreting images. For that reason, sequence protocols of patient examinations are often customized to patient-specific requirements in order to optimize image acquisition time or reduce the specific absorption rate of the RF pulse. This leads to differences in sequence parameters, e.g. the FOV, slice thickness, repetition time or voxel bandwidth. For that reason, clinical examination protocols were not equal between examined patients and images could not be used for the derivation of pCT numbers as absolute MR signal intensities were of importance.

The application of the UTE sequence showed that even with very short echo times the distinction of the tissue types bone, air and “partial volume” did not work perfectly as distributions of signal intensities of different tissue types overlapped (fig. 4.3). Sequence parameters were chosen similarly to suggestions from literature for imaging of bones, but signal-to-noise ratio (SNR) of bones was not further optimized. However, shining artifacts around the head in UTE images of patients could be reduced using fat saturation during image acquisition. But due to a limited acquisition time the SNR was decreased by 20 % compared to measurements of tissue samples. Intensities of soft bones could be clearly separated from air voxels, but intensities of cortical bone were almost as low as noise of air due to the very short T_2 and T_2^* relaxation times. Furthermore, distributions of soft tissue

and soft bone overlapped leading to an imperfect discrimination of these two tissue types.

Spatial signal inhomogeneities and impact of coil configuration

A further difficulty for interpreting absolute MR signal intensities are machine- and coil-specific systematical variations of signals. The head coil used for examinations has an inhomogeneous illumination and therefore the sensitivity of measurement is dependent on the position of a voxel in the coil. As the inhomogeneities are systematical with higher sensitivity in the center of the coil and a decreasing signal at borders, an inhomogeneity correction is implemented in sequence protocols. During measurements this correction of inhomogeneity was activated, but the results imply that correction was not perfect.

In addition, equal coil configurations used for measurements are important. Due to the fact that coil configurations of patient examinations were different, normalization factors had to be introduced. Whereas the deviation of signal intensities of patient 2 with a different coil setup was up to 68 %, mean intensities of patients 1 and 3 with equal configurations were similar on average for regions of interest in the brain. However, variations of single regions still had large variations between these patients (table 4.2).

5.2 Derivation of pseudo CT

5.2.1 Tissue samples

Pseudo CT images of mangos revealed the lowest MAEs compared to meat samples and patients. This was expected as mangos covered only a small part of the CT scale ranging from air to soft tissue. Bones, at which the other two sample types showed largest deviations, were not included. Therefore, mangos were in this context no suitable phantoms for simulating human tissue, but reasonable as a proof of concept. Meat samples covered a more realistic range of the CT scale, but also showed larger MAEs. In general, the range of MAEs per sample type was small. This result implies that HDDA was a robust method for classification although in each case only two samples were used for creating the learning database.

Cross-validation studies of mangos and meat samples using different combinations of contrasts and additional features revealed the following results: (1) PD-weighted images seemed to provide most information for the derivation of pCT values compared to all other tested contrasts besides UTE sequences (table 4.3). (2) Additional feature extraction could reduce the MAE by up to 17 - 27 % on average. (3) UTE sequences were essential for the distinction of bony tissue and air and could reduce MAE by up to 20 - 21 % on average.

In the extraction of additional features, coordinate-related features contributed most to the improvements of results of mangos because all three mangos had a very similar symmetrical geometry and comparable sizes (table 4.3). For meat samples the *box.sd* feature had largest

contributions to the improvements. Near borders, the standard deviation of a box surrounding a voxel was higher than in homogeneous tissue. Employing this additional information as a further dimension of the observation variables vector improved discrimination of “partial volume” and other tissue classes. In addition, spots at borders with deviations larger than 500 HU could be reduced considerably. The coordinate-related features *dist.xyz* and *dist.center* both also decreased the MAE showing that the spatial distribution of several tissue classes had certain degrees of cylindrical and spherical symmetries. However, effects were smaller than for mangos due to the different geometries of meat samples and positions of bones.

For both mangos and meat samples, largest errors could be found at transitions from air to soft tissue as well as soft tissue to bone and air to bone when considering results of meat samples. These intermediate regions between different tissue classes included single voxels with deviations of more than 500 HU for mangos and 1500 HU for meat samples, but had small contributions to MAEs due to the small number of voxels. Responsible for these large errors were in particular partial volume effects as well as errors of registration and image resampling by linear interpolation leading to a wrong classification on the CT scale.

Pseudo CT numbers of water-like soft tissue around 0 HU of both sample types had the lowest MEs compared to the rCT (fig. 4.5 a, c). However, MEs could not be smaller than ± 16 HU on average as the CT scale was divided into sections of 32 HU. This fact was mainly responsible for deviations of p CTs of mangos. Although MEs of soft tissue classes were small for both sample types, the classes around 0 HU had large contributions to the sum of absolute mean errors (fig. 4.5 b, d). This can be explained by the fact that in the calculation of the $CSAME_{cl}$, contributions of each class were weighted with the number of voxels of each class. The number of voxels of the soft tissue class around 0 HU was around two orders of magnitude higher for mangos and one order higher for meat samples compared to other classes.

For meat samples compact bone classes showed a strong systematical underestimation (fig. 4.5 c). One reason for that was the imperfect signal discrimination of bones and other tissue types in MR imaging. A second cause for the underestimation were clipping errors. As bone tissue classes represented the classes with highest CT numbers, either a correct classification or an underestimation was possible resulting in too low CT numbers on average.

5.2.2 Patients

The derivation of p CTs of patients showed larger MAEs in comparison to tissue samples. Results of cross-validation studies were similar to tissue samples. PD-weighted images and the UTE sequence as well as the extraction of additional features reduced MAEs significantly (table 4.4). In addition, MAEs of the three patients covered only a small range indicating the robustness of the classification method.

All applied additional features contributed to the improvements (table 4.4). The coordinate-related features *dist.xyz* and *dist.center* enhanced the distinction of air and bones decreasing errors of air voxels. Information extracted from the neighborhood of voxels using the *box.mean* and *box.sd* features reduced deviations of p CTs at transitions between different tissue classes.

Similar to tissue samples, large errors in p CT images appeared at transitions between different tissue classes (fig. 4.5 e). Bone tissue classes also showed a systematical underestimation. Reasons for these errors were similar to the explanations for tissue samples.

Again p CT numbers of water-like soft tissue around 0 HU had the lowest MEs compared to the r CT, but $CSAME_{cl}$ were large (fig. 4.5 f). Similarly to tissue samples, the explanation is the high number of voxels in this class. In contrast to tissue samples, the air class contributed most to the sum of absolute mean errors. Many air voxels were classified as bone tissue having absolute errors of more than 2000 HU (fig. 4.6 f and fig. 4.7 c). Discriminating bones and air cavities was not possible in these cases. One reason explaining this result was the reduction of SNR in the UTE sequence protocol due to a limited image acquisition time in clinical practice causing a stronger overlap of distributions of intensities of these tissue types. In addition, this result might show a general limitation of the UTE sequence for distinguishing air from tissues with very small T_2 and T_2^* relaxation times. Expanding the volume for which a p CT is predicted to the mouth region would impair the results considerably due to the very low signal intensities of teeth even in UTE images. A further optimization of UTE sequence parameters might improve results.

In contrast to tissue samples, also settings of the HDDA algorithm were changed in cross-validation studies. Varying the HDDA threshold for dimension selection showed that with the standard setting of 0.20, dimensions containing information were excluded, whereas with a too small value further dimensions were selected that could not contribute to discrimination of classes and impaired the results (table 4.4).

Testing the global scaling feature equalizing the maximal expansion of head sizes showed smaller MAEs when the feature was deactivated. This was not expected as the geometries of patients became more similar to each other applying the feature. Especially for patient 3 the increase of MAE was significant when the feature was activated, whereas for the other two patients differences between both cases were small.

Comparing results of derivation of p CT values to literature is a difficult task as the measures used for evaluation of p CT are usually application-specific and regions for which a p CT is predicted differ between studies. In Johansson et al. (2011) a similar method for deriving so-called s-CT values from MR images based on a Gaussian mixture regression model was applied. The measure used for evaluation was also the MAE and a comparable region of the head of five patients was examined. MAEs varied between 117 HU and 176 HU. This is almost equivalent to the results gained in this work for three patients with MAEs between 141 HU and 165 HU.

5.3 Ion radiotherapy treatment plan simulation

As expected, the estimation of mean deviation of WET showed similar results as the calculation of MEs per class because the errors of pCT were directly translated into deviations of WET. The results showed that in treatment plan simulations, beams passing a large number of soft tissue voxels were uncritical, whereas for air, “partial volume” and bones, large deviations of dose distributions had to be expected (table 4.5).

Treatment planning for ion radiotherapy using TRiP98 was an inverse planning process. At first, dose distributions of PTVs were optimized either using pCT or rCT and resulting plans were both recalculated on rCT images that were assumed to be the gold standard. For that reason, rCT optimized plans were a suitable benchmark for pCT plans.

In the simulation of ion radiotherapy treatment plans, dose distributions in CT cubes, mean doses and volumes of PTVs with a dose less than 90 % of prescribed dose were compared between pCT and rCT optimizations (table 4.6 and fig. 4.10, 4.11, 4.12, 4.13). Results obtained for protons and carbon ions used as irradiation modalities were comparable. The main difference in dose distributions was the characteristic dose tail of carbon ions originating from nuclear fragmentation behind the spread-out Bragg peak.

Comparing pCT and rCT optimizations, results of patients revealed smaller differences than results of meat samples although MAEs of patients were around 68 % higher on average compared to meat samples. Due to the much smaller volumes of meat samples in comparison to patients, the proportion of bones along the beam path was higher. Therefore the averaged WET of beam paths had larger deviations. Furthermore, both soft tissue and bones were underestimated, representing the tissue classes with the largest proportion along the beam path. That is the reason why distal regions of PTVs showed an underdosage. For patients the situation was different. The beam had to pass a small length of bones having a strong underestimation and a longer distance through soft tissue that was slightly overestimated. Thus, an averaging of errors became possible resulting in much smaller deviations of WET along the beam path compared to meat samples. In general, the PTV position in the brain of patients was not the most challenging one as no air cavities and only the thin bone of the skull were along the beam path. In addition, only hypothetical PTVs were considered in this study and plan optimizations did not account for organs at risk. As a further step, clinical plans containing tumor volumes and organs at risk contoured by physicians might be used for comparison of pCT and rCT optimizations.

Besides, differences of dose statistics parameters between pCT and rCT optimizations had higher variations between the three meat samples than between the three patients (table 4.6 and fig. 4.13). This result can be explained with the different geometries of meat samples and ratios of soft tissue and bones along beam paths. In contrast, variations within patients and between different beam directions were small due to corresponding geometries with similar systematical errors.

5.4 Photon radiotherapy treatment plan simulation

Unlike the simulations of ion treatment plans, photon simulation using VIRTUOS was a forward-optimization process. As a result, the optimization was independent of CT cubes of patients and only the geometrical shapes of PTVs were important. After optimizing the fields, dose distributions were calculated on pCT as well as rCT. Therefore, errors in pCTs did not affect the photon field optimizations, but had an effect on the calculation of dose distributions in PTVs and surrounding tissue. Consequently and in contrast to ion treatment plan simulations, it was possible that pCT simulations showed a better dose coverage of PTV than rCT simulations. For that reason, the absolute differences between the parameters mean dose and volume of PTV with a dose less than 90 % of prescribed dose as well as the differences of DVH curves were used for evaluation. The results of pCT and rCT simulations showed that dose distributions were almost equal. It follows that the sensitivity of photons to errors in pCTs was much smaller compared to protons or carbon ions (table 4.6 and fig. 4.13, 4.14). Using fields from seven directions further decreased effects of local errors and improved robustness. As differences of simulations were small, in these cases a MRI-based simulation of photon treatment plans might be an alternative to CT-based simulation for patients with tumors in the brain at positions such as investigated here.

These results were in accordance to literature, where several studies investigated the feasibility of MRI-based simulation of photon treatment plans in the head region of patients (Prabhakar et al., 2007; Kristensen et al., 2008; Stanescu et al., 2008; Jonsson et al., 2010). Two approaches were pursued in these studies. In a first approach, the patient outline was delineated in MR images and a unit electron density was associated with the whole irradiated volume. A second method assigned bulk electron densities to the target volume, organs at risk and additional structures, such as the patient outline and bones, using either a manual or automatic segmentation of MR images. Performances of both MRI-based methods in simulations of photon treatment plans revealed similar results compared to standard clinical techniques based on CT. All four publications reported that a MRI-based simulation of treatment plans might be a feasible option for photon radiotherapy of the brain region, in particular when using the bulk density approach taking bones into account.

5.5 Ion radiotherapy treatment plan adaptation

The application of MRI for treatment plan adaptation was tested by simulating a movement of target volume. For both, meat sample 2 and all three patients, the cCT optimizations of adapted plans showed a significantly better dose coverage of the shifted target volume compared to rCT optimized plans without plan adaptations (table 4.7 and fig. 4.17). This result demonstrated that the error introduced by replacing a volume of the rCT containing

solely soft tissue by MRI-based pCT values was much smaller than the error resulting from a target volume shift of 2.25 mm in x - and 1.25 mm in y -direction for meat sample 2 and 1.6 mm in both directions for the three patients. In these cases, the hybrid approach of combining one CT examination with soft tissue corrections from MRI examinations before each fraction would give the opportunity of treatment plan adaptations to interfractional changes of anatomy and could improve dose coverage of target volumes. A disadvantage of the approach of replacing only parts of the rCT would be the introduction of registration errors. Therefore, a careful evaluation of advantages and disadvantages in comparison to a full substitution is required.

In practice, the effect of a tumor shift on the dose coverage of the tumor volume is smaller than in the experiment. That is because margins are defined around the clinical target volume and the resulting PTV is irradiated. In order to reduce these margins and the dose to healthy tissue, MRI-based treatment plan adaptation before fractions seems to be a quite interesting application and might improve accuracy of treatment planning.

5.6 Practical aspects

Although MRI-based treatment plan simulation was tested with patient data in this work, many practical problems have to be solved thinking towards a clinical implementation:

- Positioning of patients at MRI examinations has to be similar to the positions at radiotherapy treatments.
- Fixations used for patient positioning have to be MRI-compatible, i. e. they may not contain any ferromagnetic components.
- MR sequences with small geometric image distortions have to be selected.
- MR images have to be evaluated carefully with regard to image artifacts, e. g. chemical shift, susceptibility or motion artifacts, which may result in ghosting, image distortion as well as loss or gain of signal intensities of voxels.
- Patients with metal implants may not be examined at MRI scanners or at least severe artifacts and image distortions have to be expected.
- Standard settings, coil configurations, sequence protocols and workflows have to be defined specifically for applications at different regions of the body.
- Image registration of MR and CT images worked well in the head region, but may cause difficulties at other regions of the body, at which anatomical changes between examinations are more common.

5.7 Outlook

Future investigations should either focus on the improvement of the *classification-based method* or investigate alternative methods for deriving a pCT from MR images. The major challenge using the *classification-based method* was the distinction of compact bones and air. In the following, several opportunities are proposed that might improve classification results:

- An extended set of samples should be employed for creating the learning database of decision rules to compensate for anomalies and differences between samples.
- More suitable MRI contrast parameters may have to be found for a further improved discrimination of tissue classes.
- UTE sequence parameters might be optimized for improving the SNR of compact bones and air.
- A better correction of inhomogeneous coil illumination than the implemented filter might decrease the variances of MR signal intensities of the different classes.
- Alternative additional features, e. g. larger box sizes of $7 \times 7 \times 7$ voxels for mean and standard deviation might reduce the effects of partial volume and interpolation leading to smaller errors at tissue transitions.
- Bone and air probability maps as further additional features might improve discrimination of air and bones.
- The CT scale may be divided into non-equidistant sections. This would especially decrease errors of soft tissue as the bin size of CT classes could be reduced for that tissue type.
- More sophisticated discrimination tools like non-parametric discriminant analysis or support vector machines may have to be used instead of HDDA.
- The application of Gaussian process regression models instead of discriminant analysis would allow the prediction of continuous pCT numbers without discrete classes.

As an alternative to an optimization of the *classification-based method*, an *atlas-based method* might be employed for deriving pCT values from MR images. One major advantage would be that a clinical MR sequence could be used for calculating the image transformation. Variations in absolute MR signal intensities would be less critical. During the non-rigid registration process, anatomical structures are translated and deformed, but voxel intensities stay unchanged. Therefore, systematical under- or overestimations of voxels belonging to one tissue class would be unlikely. On the other hand, a MRI-alone derivation of pCT

without any real CT examination would only be possible if the employed atlas was based on former MR and CT examinations of other patients. In that case, the atlas would not be patient-specific and anatomical differences between patients might impair results. In addition, as prediction of this alternative approach is not based on single voxels, performance might be worse for changes that cannot be described by a translation or deformation of voxels, e.g. the filling of an air cavity with mucus.

6 | Conclusions

The aim of this work was to investigate the potential of MRI for applications in ion radiotherapy treatment plan simulation and adaptation using a classification-based approach. MR signal intensities were translated into ion ranges pursuing a two-step approach. A tissue classification method based on discriminant analysis was employed for deriving pCT numbers from MR images, followed by a translation into ion ranges.

The *search for suitable MR sequences* showed that combining several MRI contrasts enhanced the separation and classification of different tissue types analyzing their absolute MR signal intensities. The distinction of bones and air was challenging and could be improved significantly with the application of an UTE sequence with very short echo time. Besides, the PD-weighted MRI contrast seemed to contain most information.

In the *derivation of pseudo CT*, the evaluation of the classification tool demonstrated that a purely statistical classification approach allows for deriving pCT numbers from MR images although no physical relationship exists. Results obtained in cross-validation studies of mangos, meat samples and patients revealed largest deviations at transitions between different tissue types and at compact bones and air cavities, whereas soft tissue was in good agreement with reference values.

Treatment plan simulation of ion radiotherapy plans revealed that the effect of uncertainties in pCT images introduced by a wrong classification of bones was largely dependent on the proportion of these along the beam path. In cases of a small ratio of bone to soft tissue, e.g. for irradiation of the brain, results of rCT optimizations exhibited only slightly higher mean doses of PTVs than pCT optimizations.

In simulations of photon treatment plans, pCT and rCT simulations showed almost equal dose distributions indicating that photons have a much lower sensitivity to errors in pCTs than protons or carbon ions.

Considering applications of MRI for *treatment plan adaptation*, a target volume shift was simulated and a hybrid approach combining one CT examination with soft tissue corrections from MRI examinations before each fraction was proposed. It was shown that the error introduced by substituting a volume of the rCT around the target containing solely soft tissue was significantly smaller than the uncertainty resulting from a target volume shift

between 1.25 mm and 2.25 mm in two directions. This result indicates that applications in adaptive ion radiotherapy are especially interesting.

Results achieved in this work for tissue samples and for the head region of patients represent first steps towards MRI-based treatment plan simulation in ion radiotherapy and provided first evidence for feasibility. Improvements for the tissue classification method as well as investigations of alternative methods have been proposed. Furthermore, an expansion of tests to other regions of the body, e.g. the prostate, would be required in order to assess the performances of different approaches for various applications.

In the future, MRI may complement the treatment planning process for ion radiotherapy and improve the accuracy so as to reap the rewards of highly conformal irradiation of tumors with charged particles. Especially applications in adaptive ion radiotherapy seem to be interesting as MRI examinations before each fraction would give the opportunity of adaptation to interfractional changes of anatomy without additional dose to the patient. As depth-dose distributions of ions are in comparison to photons far more sensitive to errors in CT images, results obtained for ion radiotherapy represent a reliable test if MRI-based treatment plan simulation is generally feasible.

Thinking further, even a device combining an ion beam applicator and a MRI scanner is conceivable (fig. 6.1). Such a device would not only allow for compensating anatomical changes between fractions, but also intrafractional changes, e.g. a movement of chest due to breathing, might be taken into account making a real-time adaptation of ion radiotherapy treatment possible.

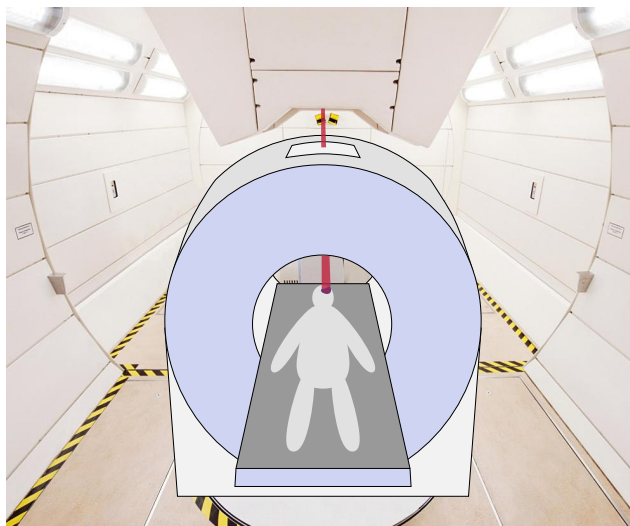


Figure 6.1: Vision for the future: ion beam applicator (beam nozzle in the upper part of the image) combined with a MRI scanner. Such a hybrid device would allow for real-time imaging and treatment plan adaptation to anatomical changes during irradiation of a patient (photomontage, original image adopted from <http://www.klinikum.uni-heidelberg.de/Gantry-Pressbilder-Stand-Oktober-2012.129328.0.html>, March 10, 2013).

A | Appendix

A.1 MMclassification package

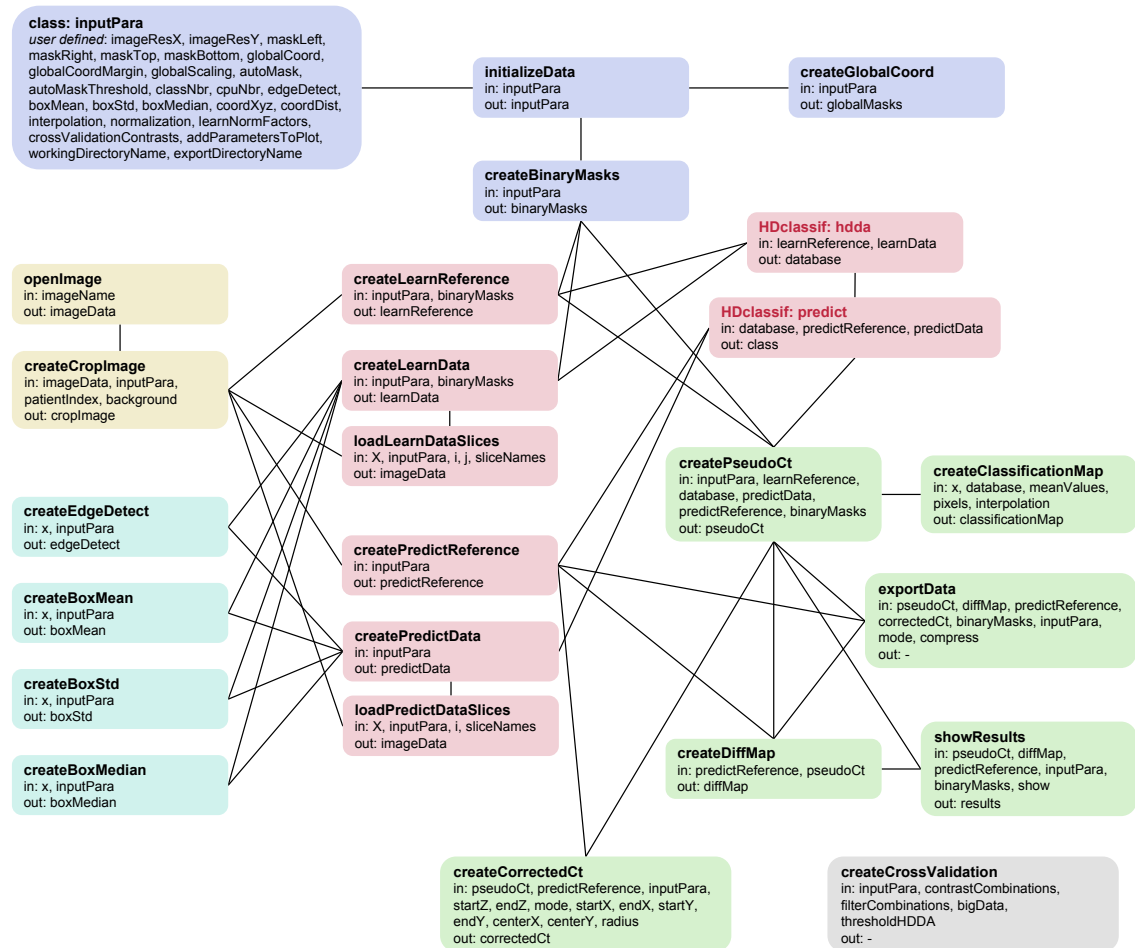


Figure A.1: Framework of functions of the *MMclassification* package (version 0.4.6) for reading and processing MR and CT data in order to derive p CT numbers from MR images.

package name	version
grid	2.14.2
gtools	2.7.0
HDclassif	1.2.1
hexbin	1.26.0
hier.part	1.0-3
lattice	0.20.6
MASS	7.3-17
methods	2.14.2
oro.dicom	0.3.3
snow	0.3-9
snowfall	1.84

Table A.1: List of *R* packages on which the *MMclassification* package (version 0.46) depends. *R* was used in version 2.14.2.

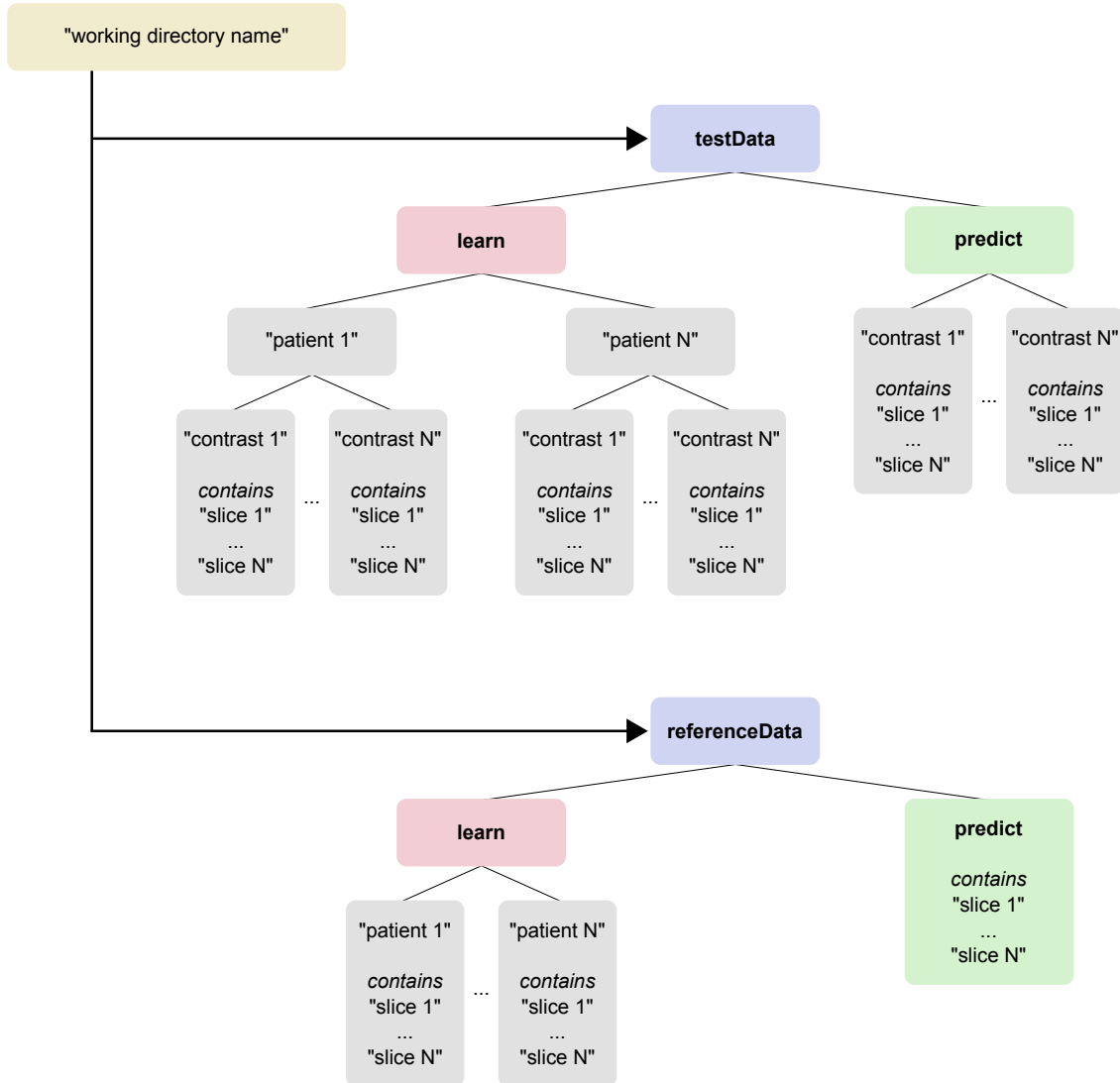


Figure A.2: File structure needed for reading MRI and CT data: folder names in quotation marks can be chosen arbitrarily, whereas bold folder have to be named as illustrated.

Program code

Definition of input parameters

```
# STEP 1: create class with input parameters having DEFAULT values
inputPara <- new("inputPara")

# STEP 2: define image resolution
inputPara@imageResX <- 512      # value has to be a multiple of 2
inputPara@imageResY <- 512      # value has to be a multiple of 2

# STEP 3: define pixels to be removed at each side of the image
inputPara@maskLeft <- 140       # left
inputPara@maskRight <- 10        # right
inputPara@maskTop <- 120         # top
inputPara@maskBottom <- 130      # bottom

# OR automatic masking of the object using:
inputPara@autoMask <- 1          # 1 for "ON" and 0 for "OFF"
inputPara@autoMaskThreshold <- c(100, 100, 100) # threshold to
    distinguish air from tissue for each object
inputPara@globalCoord <- 1       # 1 for "ON" and 0 for "OFF"
inputPara@globalCoordMargin <- 15 # margin around the object
inputPara@globalScaling <- 1     # scale objects to the same size

# STEP 4: define number of classes the images are divided into
inputPara@classNbr <- 64         # value has to be in the form 2^x

# STEP 5: define which additional filters are employed
inputPara@edgeDetect <- 0        # 1 for "ON" and 0 for "OFF"
inputPara@boxMean <- 0           # 1 for "ON" and 0 for "OFF"
inputPara@boxStd <- 0            # 1 for "ON" and 0 for "OFF"
inputPara@boxMedian <- 0         # 1 for "ON" and 0 for "OFF"
inputPara@coordXyz <- 0          # 1 for "ON" and 0 for "OFF"
inputPara@coordDist <- 0         # 1 for "ON" and 0 for "OFF"
inputPara@interpolation <- 0     # 1 for "ON" and 0 for "OFF"
inputPara@normalization <- 0     # 1 for "ON" and 0 for "OFF"

# STEP 6: define parameters for export of pseudo CT
inputPara@export$createdBy <- "user"
inputPara@export$patientName <- "PAT001" # patientName must have
    three letters and three numbers
inputPara@export$pixelSize <- 0.5        # in mm
inputPara@export$sliceDistance <- 1      # in mm
```

```
# STEP 7: define optional parameters
inputPara@cpuNbr <- 2          # number of CPUs used
inputPara@addParametersToPlot <- 1 # 1 for "ON" and 0 for "OFF"
inputPara@crossValidationContrasts <- 0

# STEP 8: define working directory and export directory path names
inputPara@workingDirectoryName <- ".../workingDirectoryName"
inputPara@exportDirectoryName <- ".../exportDirectoryName"
```

Example of a typical workflow

```
# STEP 1: create class with input parameters having DEFAULT values
inputPara <- new("inputPara")

# STEP 2: define input parameters => type "?inputPara" for help
inputPara@workingDirectoryName <- system.file("extdata", package="
  MMclassification") # will load and process example images
inputPara@exportDirectoryName <- ".../exportDirectoryName"

# STEP 3: automatically generate list with file structure
inputPara <- initializeData(inputPara = inputPara)
binaryMasks <- createBinaryMasks(inputPara = inputPara)

# STEP 4: create learn database
learnReference <- createLearnReference(inputPara = inputPara,
  binaryMasks = binaryMasks)
learnData <- createLearnData(inputPara = inputPara, binaryMasks =
  binaryMasks)
database <- hdda(data = learnData, cls = learnReference[,2],
  scaling = TRUE)

# STEP 5: predict data
predictReference <- createPredictReference(inputPara = inputPara)
predictData <- createPredictData(inputPara = inputPara)
pseudoCt <- createPseudoCt(inputPara = inputPara, learnReference =
  learnReference, database = database, predictData = predictData,
  predictReference = predictReference, binaryMasks = binaryMasks)

# STEP 6: evaluation
diffMap <- createDiffMap(predictReference = predictReference,
  pseudoCt = pseudoCt)
results <- showResults(pseudoCt = pseudoCt, diffMap = diffMap,
  predictReference = predictReference, inputPara = inputPara,
  binaryMasks=binaryMasks)
```

```
# STEP 7: export results
# works only if 'inputPara@exportDirectoryName' is defined
exportData(pseudoCt=pseudoCt, predictReference=predictReference,
  correctedCt=NULL, mode="ctx", inputPara=inputPara)
exportData(pseudoCt=pseudoCt, diffMap=diffMap, predictReference=
  predictReference, binaryMasks=binaryMasks, correctedCt=NULL,
  mode="png", inputPara=inputPara)
exportData(pseudoCt=pseudoCt, diffMap=diffMap, predictReference=
  predictReference, binaryMasks=binaryMasks, mode="RData",
  inputPara=inputPara)
```


Scientific contributions related to this thesis

Rank, C. M., Tremmel, C., Hünemohr, N., Nagel, A. M., Jäkel, O., and Greilich, S. (2013). MRI-based treatment plan simulation and adaptation for ion radiotherapy using a classification-based approach. *Radiation Oncology*, 8(51).

Rank, C. M., Hünemohr, N., Nagel, A. M., Röthke, M. C., Jäkel, O., and Greilich, S. (2013). MRI-based treatment plan simulation and adaptation for ion radiotherapy. Accepted for oral presentation at the 2nd ESTRO Forum 2013. April 19 - April 23, 2013 - Geneva, Switzerland.

List of Figures

1.1	Effect of interfractional changes on the dose coverage of a tumor target . . .	1
2.1	Principle of CT imaging	4
2.2	Nuclear magnetic moments and Zeeman splitting of hydrogen in the environment of a constant magnetic field	6
2.3	Temporal evolution of magnitudes of longitudinal and transversal component of magnetization after excitation	7
2.4	Cartesian and radial schemes for probing the k -space	8
2.5	Dependence of the MRI contrast on sequence parameters	8
2.6	Principle of classification using QDA	11
2.7	Depth-dose distributions of photons and ions	13
2.8	Principle of WEPL concept	15
3.1	Mangos and meat samples used for measurements	20
3.2	k -space sampling of applied UTE sequence and examples of MR and CT imaging of bones	22
3.3	Principle of image registration	23
3.4	Workflow of <i>MMclassification</i> package	24
3.5	Image processing steps implemented in the <i>MMclassification</i> package	25
4.1	Overview of experiments and workflow	30
4.2	Examples of UTE images of the human brain with different settings	32
4.3	Distributions of absolute MR signal intensities of five different tissue types for meat samples and patients	34
4.4	Examples of a transversal slice of p CT, r CT and difference map of a mango and a meat sample	38
4.5	Mean errors of p CT per class and contributions of CT classes to the sum of absolute mean errors	40
4.6	Examples of transversal slices of p CT, r CT and difference map of the head region of a patient	42

4.7	Examples of a sagittal slice of p CT, r CT and difference map of the head region of a patient	43
4.8	HLUTs used for translation of CT to WEPL	44
4.9	Examples of PTV definitions for meat samples and patients	45
4.10	Examples of treatment plan simulations of a meat sample for carbon ions and protons	47
4.11	Examples of treatment plan simulations of a patient for carbon ions and protons	48
4.12	DVHs of treatment plan simulations for carbon ions	49
4.13	Dose statistics parameters of treatment plan simulations for carbon ions, protons and photons	50
4.14	Example of photon treatment plan simulations of a patient	52
4.15	Simulated target volume shifts and creation of c CTs	53
4.16	Examples of treatment plan adaptation for carbon ions	54
4.17	DVHs of treatment plan adaptation for carbon ions	55
6.1	Vision for the future: ion beam applicator combined with a MRI scanner . .	68
A.1	Framework of functions of the <i>MMclassification</i> package	i
A.2	File structure needed for reading MRI and CT data	ii

List of Tables

3.1	MR- and CT-related parameters for tissue from literature	21
4.1	Parameter settings of applied MR sequences	31
4.2	Measurement and calculation of normalization factors	33
4.3	Results of cross-validation studies for mangos and meat samples	36
4.4	Results of cross-validation study for patients	41
4.5	Mean errors of p CT and estimated mean deviations of WET for different tissue types	45
4.6	Dose statistics parameters of treatment plan simulations for carbon ions, protons and photons	46
4.7	Dose statistics parameters of treatment plan adaptation for carbon ions and protons	53
A.1	List of <i>R</i> packages on which the <i>MMclassification</i> package depends	ii

Bibliography

- Bazalova, M., Carrier, J.-F., Beaulieu, L., and Verhaegen, F. (2008). Dual-energy CT-based material extraction for tissue segmentation in Monte Carlo dose calculations. *Physics in Medicine and Biology*, 53(9):2439–2456.
- Bendl, R., Pross, J., and Schlegel, W. (1993). VIRTUOS - A program for VIRTUal radiOtherapy Simulation. In Lemke, H., Inamura, K., Jaffe, C., and Felix, R., editors, *Computer Assisted Radiology. Proceedings of the International Symposium CAR 93*, pages 676–682, 822–823. Springer.
- Berge, L., Bouveyron, C., and Girard, S. (2012). HDclassif: An R Package for Model-Based Clustering and Discriminant Analysis of High-Dimensional Data. *Journal Of Statistical Software*, 46(6):1–29.
- Berker, Y., Franke, J., Salomon, A., Palmowski, M., Donker, H. C. W., Temur, Y., Mottaghy, F. M., Kuhl, C., Izquierdo-Garcia, D., Fayad, Z. a., Kiessling, F., and Schulz, V. (2012). MRI-Based Attenuation Correction for Hybrid PET/MRI Systems: A 4-Class Tissue Segmentation Technique Using a Combined Ultrashort-Echo-Time/Dixon MRI Sequence. *Journal of Nuclear Medicine*, 53(5):796–804.
- Bert, C. and Durante, M. (2011). Motion in radiotherapy: particle therapy. *Physics in Medicine and Biology*, 56(16):R113–R144.
- Bethe, H. (1930). Zur Theorie des Durchgangs schneller Korpuskularstrahlen durch Materie. *Annalen der Physik*, 397(3):325–400.
- Bloch, F. (1933a). Bremsvermögen von Atomen mit mehreren Elektronen. *Zeitschrift für Physik*, 81(5-6):363–376.
- Bloch, F. (1933b). Zur Bremsung rasch bewegter Teilchen beim Durchgang durch Materie. *Annalen der Physik*, 408(3):285–320.
- Bloch, F. (1946). Nuclear Induction. *Physical Review*, 70(7-8):460–474.
- Boettger, T., Nyholm, T., Karlsson, M., Nunna, C., and Celi, J. C. (2008). Radiation therapy planning and simulation with magnetic resonance images. *Proceedings of SPIE*, 6918:69181C–1–11.

- Bouveyron, C. (2012). *HDclassif: an R Package for Model-Based Classification of High-Dimensional Data*. Talk, Université Paris 1 Panthéon-Sorbonne, France.
- Bouveyron, C., Girard, S., and Schmid, C. (2007). High Dimensional Discriminant Analysis. *Symposium A Quarterly Journal In Modern Foreign Literatures*, 36(14):1–9.
- Bragg, W. H. and Kleeman, R. (1905). XXXIX. On the α particles of radium, and their loss of range in passing through various atoms and molecules. *Philosophical Magazine Series 6*, 10(57):318–340.
- Bushberg, J. T., Seibert, J. A., Leidholdt, E. M., and Boone, J. M. (2002). *The Essential Physics of Medical Imaging*. Lippincott Williams & Wilkins, 2nd edition.
- Catana, C., van der Kouwe, A., Benner, T., Michel, C. J., Hamm, M., Fenchel, M., Fischl, B., Rosen, B., Schmand, M., and Sorensen, A. G. (2010). Toward implementing an MRI-based PET attenuation-correction method for neurologic studies on the MR-PET brain prototype. *Journal of Nuclear Medicine*, 51(9):1431–1438.
- Chen, G. T. Y., Singh, R. P., Castro, J. R., Lyman, J. T., and Quivey, J. M. (1979). Treatment planning for heavy ion radiotherapy. *International Journal of Radiation Oncology, Biology, Physics*, 5(10):1809–1819.
- Dowling, J. a., Lambert, J., Parker, J., Salvado, O., Fripp, J., Capp, A., Wratten, C., Denham, J. W., and Greer, P. B. (2012). An atlas-based electron density mapping method for magnetic resonance imaging (MRI)-alone treatment planning and adaptive MRI-based prostate radiation therapy. *International Journal of Radiation Oncology, Biology, Physics*, 83(1):e5–e11.
- Edmund, J., Kjer, H., and Hansen, R. (2012). Auto-Segmentation of Bone in MRI-Only Based Radiotherapy Using Ultra Short Echo Time. *Radiotherapy and Oncology*, 103:S75.
- Fallone, B. G., Murray, B., Rathee, S., Stanescu, T., Steciw, S., Vidakovic, S., Blosser, E., and Tymofichuk, D. (2009). First MR images obtained during megavoltage photon irradiation from a prototype integrated linac-MR system. *Medical Physics*, 36(6):2084–2088.
- Fisher, R. A. (1936). The Use of Multiple Measurements in Taxonomic Problems. *Annals of Eugenics*, 7:179–188.
- Floca, R. (2009). MatchPoint: On Bridging the Innovation Gap between Algorithmic Research and Clinical Use in Image Registration. In Dössel, O. and Schlegel, W., editors, *World Congress on Medical Physics and Biomedical Engineering, 2009, Munich, Germany*, volume 25/4 of *IFMBE Proceedings*, pages 1105–1108. Springer.

- Gold, G., Han, E., and Stainsby, J. (2004). Musculoskeletal MRI at 3.0 T: relaxation times and image contrast. *American Journal of Roentgenology*, 183(8):343–351.
- Greer, P. B., Dowling, J. A., Lambert, J. A., Fripp, J., Parker, J., Denham, J. W., Wratten, C., Capp, A., and Salvado, O. (2011). A magnetic resonance imaging-based workflow for planning radiation therapy for prostate cancer. *Medical Journal of Australia*, 194(4):24–27.
- Gwosch, K. C. (2012). *Non-Invasive Monitoring of Carbon Ion Beam Therapy by Tracking of Secondary Ions – An Initial Study*. Master thesis, University of Heidelberg, Germany.
- Hastie, T., Tibshirani, R., and Friedman, J. (2011). *The Elements of Statistical Learning*. Springer, 2nd edition.
- Hofmann, M., Steinke, F., Scheel, V., Charpiat, G., Farquhar, J., Aschoff, P., Brady, M., Schölkopf, B., and Pichler, B. J. (2008). MRI-based attenuation correction for PET/MRI: a novel approach combining pattern recognition and atlas registration. *Journal of Nuclear Medicine*, 49(11):1875–1883.
- Hounsfield, G. N. (1973). Computerized transverse axial scanning (tomography): Part I. Description of system. 1973. *The British Journal of Radiology*, 46(552):1016–1022.
- Jähne, B. (2005). *Digital Image Processing*. Springer, 6th edition.
- Jäkel, O., Jacob, C., and Schardt, D. (2001a). Relation between carbon ion ranges and x-ray CT numbers. *Medical Physics*, 28(4):701–703.
- Jäkel, O., Krämer, M., Karger, C. P., and Debus, J. (2001b). Treatment planning for heavy ion radiotherapy: clinical implementation and application. *Physics in Medicine and Biology*, 46(4):1101–1116.
- Jellus, V. (2010). *Applications Guide: UTE 3D imaging with ultrashort echo times*. Siemens AG, Healthcare Sector.
- Johansson, A., Karlsson, M., and Nyholm, T. (2011). CT substitute derived from MRI sequences with ultrashort echo time. *Medical Physics*, 38(5):2708–2714.
- Johansson, A., Karlsson, M., Yu, J., Asklund, T., and Nyholm, T. (2012). Voxel-wise uncertainty in CT substitute derived from MRI. *Medical Physics*, 39(6):3283–3290.
- Jonsson, J. H., Karlsson, M. G., Karlsson, M., and Nyholm, T. (2010). Treatment planning using MRI data: an analysis of the dose calculation accuracy for different treatment regions. *Radiation Oncology*, 5(62).
- Kalender, W. A. (2011). *Computed Tomography*. Publicis Publishing, 3rd edition.

- Karlsson, M., Karlsson, M. G., Nyholm, T., Amies, C., and Zackrisson, B. (2008). Dedicated magnetic resonance imaging in the radiotherapy clinic. *International Journal of Radiation Oncology, Biology, Physics*, 72(2):644–651.
- Keereman, V., Fierens, Y., Broux, T., De Deene, Y., Lonnew, M., and Vandenberghe, S. (2010). MRI-based attenuation correction for PET/MRI using ultrashort echo time sequences. *Journal of Nuclear Medicine*, 51(5):812–818.
- Kjer, H., Hansen, R., Paulsen, R., and Edmund, J. (2012). Optimized Acquisition Parameters for MRI Only RT Using Ultrashort Echo Times. *International Journal of Radiation Oncology, Biology, Physics*, 84(3):S866.
- Krämer, M., Jäkel, O., Haberer, T., Kraft, G., Schardt, D., and Weber, U. (2000). Treatment planning for heavy-ion radiotherapy: physical beam model and dose optimization. *Physics in Medicine and Biology*, 45(11):3299–3317.
- Kristensen, B. H., Laursen, F. J. r., Lø gager, V., Geertsen, P. F., and Krarup-Hansen, A. (2008). Dosimetric and geometric evaluation of an open low-field magnetic resonance simulator for radiotherapy treatment planning of brain tumours. *Radiotherapy and Oncology*, 87(1):100–109.
- Lagendijk, J. J. W., Raaymakers, B. W., Raaijmakers, A. J. E., Overweg, J., Brown, K. J., Kerkhof, E. M., van der Put, R. W., Hårdemark, B., van Vulpen, M., and van der Heide, U. A. (2008). MRI/linac integration. *Radiotherapy and Oncology*, 86(1):25–29.
- Lambert, J., Greer, P. B., Menk, F., Patterson, J., Parker, J., Dahl, K., Gupta, S., Capp, A., Wratten, C., Tang, C., Kumar, M., Dowling, J., Hauville, S., Hughes, C., Fisher, K., Lau, P., Denham, J. W., and Salvado, O. (2011). MRI-guided prostate radiation therapy planning: Investigation of dosimetric accuracy of MRI-based dose planning. *Radiotherapy and Oncology*, 98(3):330–4.
- Lee, Y. K., Bollet, M., Charles-Edwards, G., Flower, M. A., Leach, M. O., McNair, H., Moore, E., Rowbottom, C., and Webb, S. (2003). Radiotherapy treatment planning of prostate cancer using magnetic resonance imaging alone. *Radiotherapy and Oncology*, 66(2):203–216.
- Leo, W. R. (1994). *Techniques for Nuclear and Particle Physics Experiments*. Springer, 2nd edition.
- Liang, Z.-P. and Lauterbur, P. C. (2000). *Principles of Magnetic Resonance Imaging*. Wiley-IEEE Press Series in Biomedical Engineering, 1st edition.
- Paganetti, H. (2012). Range uncertainties in proton therapy and the role of Monte Carlo simulations. *Physics in Medicine and Biology*, 57(11):R99–117.

- Prabhakar, R., Julka, P. K., Ganesh, T., Munshi, A., Joshi, R. C., and Rath, G. K. (2007). Feasibility of using MRI alone for 3D radiation treatment planning in brain tumors. *Japanese Journal of Clinical Oncology*, 37(6):405–411.
- Purcell, E. M., Torrey, H. C., and Pound, R. V. (1946). Resonance Absorption by Nuclear Magnetic Moments in a Solid. *Physical Review*, 69(1-2):37–38.
- R Development Core Team (2012). *R: A Language and Environment for Statistical Computing*. R Foundation for Statistical Computing.
- Rahmer, J., Blume, U., and Börnert, P. (2007). Selective 3D ultrashort TE imaging: comparison of "dual-echo" acquisition and magnetization preparation for improving short-T2 contrast. *Magnetic Resonance Materials in Physics, Biology and Medicine*, 20(2):83–92.
- Rank, C. M., Tremmel, C., Hünemohr, N., Nagel, A. M., Jäkel, O., and Greilich, S. (2013). MRI-based treatment plan simulation and adaptation for ion radiotherapy using a classification-based approach. *Radiation Oncology*, 8(51).
- Reichert, I. L. H., Robson, M. D., Gatehouse, P. D., He, T., Chappell, K. E., Holmes, J., Girgis, S., and Bydder, G. M. (2005). Magnetic resonance imaging of cortical bone with ultrashort TE pulse sequences. *Magnetic Resonance Imaging*, 23(5):611–618.
- Reiser, M. F., Semmler, W., and Hricak, H. (2008). *Magnetic Resonance Tomography*. Springer, 1st edition.
- Schardt, D., Elsässer, T., and Schulz-Ertner, D. (2010). Heavy-ion tumor therapy: Physical and radiobiological benefits. *Reviews of Modern Physics*, 82(1):383–425.
- Schlegel, W., Pastyr, O., Bortfeld, T., Becker, G., Schad, L., Gademann, G., and Lorenz, W. J. (1992). Computer systems and mechanical tools for stereotactically guided conformation therapy with linear accelerators. *International Journal of Radiation Oncology, Biology, Physics*, 24(4):781–787.
- Schneider, U., Pedroni, E., and Lomax, A. (1996). The calibration of CT Hounsfield units for radiotherapy treatment planning. *Physics in Medicine and Biology*, 41(1):111–124.
- Stanescu, T., Jans, H.-S., Pervez, N., Stavrev, P., and Fallone, B. G. (2008). A study on the magnetic resonance imaging (MRI)-based radiation treatment planning of intracranial lesions. *Physics in Medicine and Biology*, 53(13):3579–3593.
- Stanisz, G. J., Odobina, E. E., Pun, J., Escaravage, M., Graham, S. J., Bronskill, M. J., and Henkelman, R. M. (2005). T1, T2 Relaxation and Magnetization Transfer in Tissue at 3T. *Magnetic Resonance in Medicine*, 54(3):507–512.

- Tremmel, C. (2012). *Improving ion beam therapy treatment planning for metal implants by using dual-energy CT scanning*. Master thesis, University of Heidelberg, Germany.
- Wang, C., Chao, M., Lee, L., and Xing, L. (2008). MRI-based treatment planning with electron density information mapped from CT images: a preliminary study. *Technology in Cancer Research & Treatment*, 7(5):341–348.
- Wilson, R. (1946). Radiological use of fast protons. *Radiology*, 47(5):487–491.

Acknowledgements

An dieser Stelle möchte ich mich bei allen, die zum Gelingen meiner Masterarbeit beigetragen haben, ganz herzlich bedanken, insbesondere bei:

Prof. Dr. Oliver Jäkel für die freundliche Aufnahme in seine Arbeitsgruppe und die Möglichkeit, dieses interessante Thema bearbeiten zu dürfen.

Prof. Dr. Peter Bachert für die Übernahme des Erstgutachtens und die Vertretung meiner Arbeit gegenüber der Fakultät.

Prof. Dr. Wolfgang Schlegel für die Aufnahme in die Abteilung „Medizinische Physik in der Radioonkologie“ und seine fachkundige Beratung bei Fragen jeglicher Art.

Dr. Steffen Greilich für die umfassende und fördernde Betreuung meiner Arbeit sowie die freundliche und stets kompetente Hilfe bei allen auftretenden Fragen und Problemen.

Nora Hünemohr für die kompetente Betreuung, die vielen hilfreichen Diskussionen und den Einsatz als MR-Probandin.

Allen Mitarbeitern der „Heavy Ion Therapy“ Arbeitsgruppe am DKFZ für die Hilfsbereitschaft und stets angenehme und freundschaftliche Arbeitsatmosphäre sowie die unterhaltsamen und lustigen Mittagspausen bei Kaffee und „Latte macchiato“.

Dr. Armin Nagel und Dr. Frederik Laun für die großzügige Hilfe bei allen Fragen rund um die MR-Bildgebung und die Unterstützung bei MR-Messungen.

Andreas Jäger und Dr. Ralf Floca für die Bereitstellung ihres Programms zur multimodalen Bildregistrierung.

Dr. Matthias Röthke für die Ermöglichung, mit Patientendaten arbeiten zu können, sowie Regula Gnirs und Susanne Yubai für den unermüdlichen Einsatz, Patienten für Untersuchungen zu finden und die Anleitung bei deren MR-Untersuchungen.

Hannah Prokesch und Swantje Ecker vom HIT für die interessanten Diskussionen über Ionentherapie und Bestrahlungsplanung.

Meinem Freund Kristian Rink für das Korrekturlesen des Manuskripts.

Ein ganz besonderer Dank gilt meinen Eltern für die Ermöglichung meines Physikstudiums und die herzliche Unterstützung in jeglicher Hinsicht.

Declaration

Ich versichere, dass ich diese Arbeit selbstständig verfasst und keine anderen als die angegebenen Quellen und Hilfsmittel benutzt habe.

Heidelberg, den 12. März 2013

.....